ISAS - INTERNATIONAL SCHOOL
FOR ADVANCED STUDIES

Relativistic Radiative Transfer for Accretion Flows onto Neutron Stars and Black Holes

by

Silvia Zane

Thesis submitted for the degree of
"Doctor Philosophiæ"

Astrophysics Sector

SUPERVISORS

Prof. John Miller
Prof. Aldo Treves
Dott. Roberto Turolla

October 1997

SISSA - SCUOLA INTERNAZIONALE SUPERIORE DI STUDI AVANZATI
TRIESTE
Strada Costiera 11

TRIESTE

SISSA ISAS
SCUOLA INTERNAZIONALE SUPERIORE DI STUDI AVANZATI
INTERNATIONAL SCHOOL FOR ADVANCED STUDIES

Relativistic Radiative Transfer for Accretion Flows onto Neutron Stars and Black Holes

by

Silvia Zane

Thesis submitted for the degree of

"Doctor Philosophiæ"

Astrophysics Sector

SUPERVISORS

Prof. John Miller
Prof. Aldo Treves
Dott. Roberto Turolla

October 1997

To My Brothers.

Preface

This thesis contains part of the outgrowth of the research that I carried out at the International School for Advanced Studies (SISSA–ISAS) in Trieste (Italy), during my Phd program. Actually, in this period, my scientific activity covered different fields of theoretical astrophysics and not all of them have been presented in here. The main topics in which I am involved are:

- study of general relativistic radiative transfer in fast moving media, with particular interest on typical radiative processes of high energy accreting flows ($e-e$, $e^- - e^+$, $e-p$ bremsstrahlung, pair production-annihilation, Compton scattering...);
- observability of accreting old neutron stars (ONSs) with EUVE and ROSAT as single sources and analysis of their diffuse emission; phase–space distribution of galactic ONSs;
- Galactic Center environment;
- General Relativity; equilibrium and stability properties of rotating configurations in 3D.

The main part of my research activity was aimed to study the transfer of radiation in relativistic stationary flows accreting onto compact objects (black holes and neutron stars), in connection with the study of spectral properties for particular classes of X-rays, EUV sources. This is the topic of this thesis, too. I used, in different applications, two different theoretical approaches to the general relativistic treatment of radiative transfer. The first one, originally developed by Thorne (1981), exploits an expansion of the specific intensity of the radiation field into moments (projected symmetric trace-free tensors) so that it has the main advantage of reducing the dimensionality of the problem. Despite it has been probed to be a fast, powerful tool for tackling problems of relativistic radiation hydrodynamics for 1–dimensional flows, at the same time, it presents a number of limitations that are described in detail later on in this thesis. As an example, it does not allow a correct treatment when dealing with high–energy regimes. In fact, it is just the lack of informations about the angular dependence of the radiation field that makes impossible to describe processes like photon–photon pair production and non isotropic scattering, that start to be important in high temperature plasmas ($T \gtrsim 10^8$). This is one of the reasons that initially motivated our interest in investigating other kind of approaches. In this thesis I present a second, alternative formalism, in which the transfer equation is directly solved along its characteristic directions, i.e. along the photon propagation directions in the phase space. Using this approach, an exact (numerical) solution for the photon distribution function is naturally provided, allowing a complete treatment of non–isotropic radiative processes. A numerical code has been developed and is presented here. Solutions for both the radiation

field in a fixed background or for the full radiation–hydrodynamical problem have been obtained in spherical and plane-parallel geometry. Particular care has been devoted to a detailed evaluation of the source term, taking into account for the main radiative processes that take place in astrophysical flows. In its present version, the code can deal with $e^- - e^-$, $e^+ - e^+$, $e^- - e^+$, $e^- - p$, $e^+ - p$ bremsstrahlung, pair production-annihilation, Thomson and Compton scattering. In particular, Compton terms are directly calculated from integrals of the Compton scattering kernel, without resorting to the Kompaneets approximation. Radiative effects due to magnetic fields are neglected.

- This work is in the framework of a collaboration with prof. L. Nobili, dr. R. Turolla (Dep. of Physics, University of Padova) and prof. A. Treves (University of Como); the numerical code, written in Fortran, has been tested and is working now. Routines are available under request.

The second part of this thesis contains the study of different models for accretion flows; spectral results have been obtained using the numerical techniques previously described. In particular, I present the analysis of spherical accretion onto black holes and a study of the spectrum in static atmospheres around neutron stars. Since, in the first case, dynamics play an important role, this process has been studied in detail; I present here also an analytical investigation of bulk motion Comptonization in the relativistic case. It is particularly interesting that in both the BH and the NS case, the equilibrium solutions show a bimodal behaviour, with a high temperature, strongly comptonized state that coexists with a "cold" one, for the same values of the model parameters. We considered this circumstance, in con-

nection with the possibility to drive on–off transitions between the two branches. Moreover, the onset of the "hot" state may represent a possible physical mechanism for producing efficiently high energy radiation from weakly magnetized, accreting neutron stars and may be of interest in connection with hard X–ray transients, at present observed with SIGMA and BATSE. At low values of the accretion rates only the "cold" state exists; we have extensively investigated also these models, in which the emission is typically peaked in X–rays, in connection with the determination of the spectral properties of old neutron stars (ONSs) accreting the interstellar medium. The emergent spectrum shows a significant hardening with respect to the blackbody at the neutron star effective temperature, and this circumstance stimulated a lot of work aimed to reconsider the observational impact of ONSs with ROSAT and EUVE.

- These analyses are carried out in collaboration with prof. A. Treves (University of Como), dr. R. Turolla (University of Padova), dr. M. Colpi (University of Milano), dr. L. Zampieri (University of Illinois at Urbana Champaign); future works are in preparation.

I spent the last year of my Phd at the University of Illinois at Urbana–Champaign (UIUC), collaborating to a research plan in General Relativity, with the group of Relativistic and high–energy Astrophysics (Prof. S.Shapiro). These studies, however, are outside the topic of this thesis and are not reported here. At present, we are considering the problem of the determination of equilibrium sequences and stability properties of rotating, relativistic configurations in 3D. The problem is manyfold, either from the purely formal and the observational point of view. As an example, rapidly spinning NSs, subject to triaxial in-

stabilities could become important sources of gravitational waves emission and represent possible targets for the forthcoming GEO600 (Germany), LIGO (US) and VIRGO (Italy) interferometric detectors. Also, numerical simulations based on SPH calculations suggest that the coalescence and merging in a single, triaxial object is the most inevitable end point of close NS–NS binary evolution. Working in the framework of a PN approximation, we developed a completely analytical treatment of homogeneous, rigidly rotating bodies. We used a 3+1 splitting of the metric, that seems to be particularly well suited to numerical studies of the fully nonlinear equations for strong field sources. In this respect, our solution should provide an important test-bed calculation for future numerical results for tridimensional, relativistic systems. It has been found that, under these assumptions, the ADM equations can be solved analytically, and it is possible to derive approximated expressions for the main structural parameters of the rotating configuration (total mass–energy, rest mass and angular momentum); equilibrium sequences and stability points can then be obtained using a variational principle. As first application, we derived the first PN correction to the secular Jacobi–like instability point with respect to the formation of a barlike structure.

- This study is in the framework of a collaboration with Prof. S.L. Shapiro (University of Illinois at Urbana Champaign). It is supported by SISSA (Trieste, Italy) and by "Fondazione A. Gini" (University of Padova, Italy); the work is still in progress.

Table of Contents

1 Introduction

Radiative transfer in high energy, fast and differentially moving plasmas is today at the basis of a large number of currently interesting astrophysical situations, as for example accretion onto compact objects, expanding envelopes in supernova explosions and in X–ray bursting neutron stars, early phases of the cosmic expansion and jets in galactic and extragalactic sources. In many cases the production of a large amount of energy in a comparatively small volume and a spectrum which extends into the X–ray and gamma–ray domain suggest that the physical conditions under which radiation is produced are rather extreme, and involve the presence of a black hole or a neutron star, making a general relativistic treatment necessary. Both the strong gravitational field and the dynamics can substantially modify the emitted spectrum: the former via gravitational red–shift, the latter by introducing aberration, advection and Doppler shift. Moreover, contrary to a widespread belief, the effects of dynamics on the transfer of radiation are still important in presence of non–relativistic velocities, if photons are produced in optically thick regions (Mihalas, 1980; Mihalas & Mihalas, 1984; Nobili, Turolla & Zampieri, 1993, NTZ93 in the following).

Since the pioneering works by Thomas (1930), Simon (1963) and Lindquist (1966), rel-

ativistic transfer received wide attention (see e.g. Mihalas & Mihalas 1984 for references to earlier papers). Most applications presented until the early 70's focused on the diffusion approximation. However, when the medium is marginally thick, like in photospheric layers or in hot coronae, this approximation breaks down and a more general analysis is necessary. It was also realized long ago (see Castor 1972, Mihalas 1980 and references therein) that, for relativistic flows, the interaction between matter and radiation is most easily described if the material properties and the radiation field are evaluated in the frame in which the medium is at rest. This fact led to the investigation of the comoving frame transfer equation (CTE), considered by Mihalas (1980), Hauschildt & Wehrse (1991) in the framework of special relativity, and by Schmidt–Burgk (1978), Thorne (1981), Schinder & Bludman (1989) in the general–relativistic case. Broadly speaking, two levels of difficulty are encountered in the solution of the radiative transfer problem. The first one is connected to the fact that the transfer equation itself is a Boltzmann equation for the photon distribution function in phase–space (see e.g. Lindquist 1966). The mathematical structure of the differential operator is intrinsically complicated, mainly in situations without any presupposed symmetry. The second one is related to the description of the microphysics, appearing in the expression of the source term. Even in the simple case of isotropic, coherent scattering, the non–local character of the process translates into an expression of the source term that involves the zeroth moment of the photon distribution function. This makes the Boltzamnn equation an integro–differential equation. From the numerical point of view, the problem is even more challenging when dealing with high energy plasmas. In these regimes the

cross sections correspondent to astrophysically important radiative processes (like Compton scattering and pair production) can present a high degree of anisotropy and a strong dependence on the photon frequency. As a consequence, a detailed description involves the numerical evaluation of multiple integrals of the photon distribution function weighted by a suitable kernel.

Due to these complexities, usually one has to introduce some simplifying assumptions to make the analysis tractable and the present status of the art shows that any attempt to solve the relativistic problem requires a compromise between accuracy and computational cost.

The first approximation that can be introduced involves the geometry of the flow and the symmetry properties of the background metric: the simplest situation that has been investigated is the stationary, 1–dimensional problem. Different approaches for the solution of the relativistic transfer problem in the case of planar or spherical geometry have been suggested. They can be grouped, schematically, into three wide classes: direct solution of the CTE using discretization techniques, moment expansion and integration of the CTE along its characteristic directions.

The solution of the CTE by finite differencing, like in the DOME method (Hauschildt & Wehrse 1991), works well in geometrically thin layers, but the treatment of extended atmospheres requires a prohibitive number of discrete elements to obtain a fair angular resolution. In the relatively simple case examined by Hauschildt & Wehrse, the numerical calculations must be performed on supercomputers even for low resolution grids. Since in

this thesis we are mainly interested to the properties of the continuum emission in accretion flows, we will not enter in detail in the description of this method.

Approaches based on the expansion of the specific intensity in spherical harmonics (moments) are in fact a more powerful tool for solving this kind of problems. In this case the solution of the transfer problem is reconduced to the solution of a recursive system of partial differential equations that must be truncated at a given order, introducing a certain number of closure conditions. These methods have the main advantage of reducing the dimensionality of the problem since the angular dependence is suppressed. The technique is standard in the non-relativistic case (see e.g. Chandrasekhar 1960) and the first step toward a relativistic extension is due to Lindquist (1966). This pioneering work was particularized to spherical flows and only the zeroth and the first moments equations were considered. Later on, Anderson & Spiegel (1972) noted that this simple treatment was inadequate to include the effects of the shear and calculated the second moment equation, successfully reproducing Thomas' radiative viscosity. The resulting formalism, however, is so complex that it has never been applied to a marginally thick situation. Moreover, another limitation is related to the fact that in these papers a minimal closure was assumed, i.e. all moments of order higher than the order of truncation were put to zero. The issue of providing an exact closure function is at the basis of the flux limited diffusion theory (FDT) developed by Levermore & Pomraining (1981) and generalized by Pomraining (1983), Anile & Sammartino (1989) and Anile & Romano (1992). In the gray case the FDT provides a self–consistent answer by solving the differential equation for the flux limiter, but the extension to the

frequency–dependent problem seems far from being obvious.

A very sophisticated, general–relativistic variant of the moment formalism was presented by Thorne (1981). His analysis, based on an expansion in projected, symmetric, trace–free (PSTF) moments, presents some particularly interesting characteristics. First of all, the complexity of the formalism can be highly reduced in presence of symmetries. Second, the set of moment equations can be in principle truncated at an arbitrary order, allowing to achieve, in every particular problem, a good compromise between accuracy and computational cost. Even in the frequency–dependent problem, the reduced dimensionality permits a fast, direct solution for dynamical, thermodynamical and radiation variables, at least when the expansion is truncated at the second order. This method has been fruitfully applied to the solution of astrophysical problems with planar or spherical symmetry, both in the gray and in the frequency–dependent case (see e.g. Turolla & Nobili 1988, Nobili, Turolla & Zampieri 1993, Zampieri, Turolla & Treves 1993, Rezzolla & Miller 1994, 1996, Miller & Rezzolla 1995, Zampieri, Turolla, Zane & Treves, 1995, Zampieri, Miller & Turolla 1996, Rezzolla 1996). In these applications the required number of closure functions was specified "a priori" and they should reproduce the correct asymptotic limits for the radiation moments when free streaming and diffusion are approached.

The last kind of approach to the solution of the transfer problem is based on the use of the characteristics formalism. These methods start directly from the integration of the Boltzmann equation, so they give an exact (numerical) solution for the photon distribution function. The main point is that the hyperbolic character of the Boltzmann equation implies

that the CTE can be always reduced to a single ordinary differential equation along the characteristic rays. The tangent ray method (TRM) developed in a series of papers by Mihalas and coworkers (Mihalas, Kunasz & Hummer 1975, 1976a, b, Mihalas 1980) uses a semi–characteristic approach in which the integration is performed along the characteristics of the "spatial" part of the differential operator (the tangent rays), while the frequency derivative is treated by means of a standard finite–differences scheme. A fully characteristic method for the solution of the general–relativistic transfer problem has been discussed by Schmidt–Burgk (1978), Schinder (1988) and Schinder & Bludman (1989). All these investigations dealt with stationary, spherically symmetric space–times, which admit three Killing vectors: the existence of the associated constants of the motion can be used to obtain simple expressions for the characteristic rays. The analysis by Schinder & Bludman (1989) was actually restricted to a spacetime characterized by a stationary Lagrangian line–element, which corresponds to a vanishing Eulerian velocity field for the fluid. The work by Schmidt–Burgk (1978), although finalized to accretion onto a Schwarzschild hole, is, to our knowledge, the only example of an exact solution of the CTE taking into account both the effects of dynamics and strong gravity. For their simple mathematical structure, characteristic methods seem to be promising in coping with realistic astrophysical problems. Moreover, as it will be discussed later on, they naturally overcome some of the limitations that arise in the framework of moments expansion.

As anticipated, the second kind of difficulties encountered when the transfer problem is tackled, are related to the description of radiative processes. Previous investigations

were mainly concerned with the development of efficient methods for the solution of the CTE, assuming rather simple, often "ad hoc", expressions for the emission and absorption coefficients. This approach is completely justified if one is interested in investigating the formation of particular spectral features, like lines or absorption edges. On the other hand, in all situations in which attention is focussed on the continuum, an accurate treatment of all relevant radiative processes becomes important. Solutions presented by Schmidt–Burgk (1978) refers to a hot, magnetized plasma and take into account scattering absorption and synchrotron absorption/emission; the collisional term in the Boltzmann equation is written using suitable approximations. However, the expression of the source term can be very complex even restricting to the simple case of unmagnetized plasmas, if high temperature regimes are investigated. In this case the dominant radiative processes are non–conservative scattering, pair production and bremsstrahlung.

A rigorous treatments of the Compton scattering can be found in Kershaw, Prasad & Beason (1986), Kershaw (1987), Shestakov, Kershaw & Prasad (1988), but prior of this analysis their results have never been included in transfer codes devoted to astrophysical applications. Very recently, the time–dependent photon kinetic equation for Compton scattering, the corresponding radiative transfer equation and their zeroth and first moments have been reconsidered by Psaltis & Lamb (1997), who pointed out important corrections to almost all the above derivations and investigate the role of second order velocity terms in the problem.

The purpose of this thesis is to reconsider the issue of determining the solution of the

radiative transfer problem, in the framework of computing the spectral properties of particular classes of X–ray and γ–ray sources powered by accretion onto compact objects. The work presented here is organized in different levels. First, the comoving transfer equation and the PSTF moments formalism (Thorne 1981) for its solution are introduced. As already mentioned, this approach has the enormous advantage to allow a simplified, fast investigation of the full hydrodynamical problem and in many situations this level of approximation can be fully satisfactory. However, the method presents some drawbacks that makes it not completely suitable for the solution of more complicated problems. A number of reasons have motivated our interest in other kinds of formalism, and in particular in the reconsideration of the characteristic approaches.

First of all, in solving the moments equations, the lack of any information about the angular dependence of the radiation field makes impossible the treatment of processes like photon–photon pair production and non isotropic scattering, that start to be important above $T \gtrsim 10^8$ K. Approaches based on moment expansion (see e.g. Pomraining 1973 and references therein, Thorne 1981, Prasad *et al.* 1988) usually treat the Compton scattering in the Fokker–Planck approximation.

Second, in view of a future extension of the method, we are interested to investigate a formalism that could be easily applied to the study of radiation transfer in multidimensional systems. In fact, in many astrophysical scenarios rotation or other deviations from spherical symmetry can be important, as for example when dealing with accretion disks, hot coronae, cooling of neutron stars or radiatively driven jets. The necessity of an axially symmetric or

even 3D treatment of relativistic radiation hydrodynamics is not restricted to applications in which the metric itself is multidimensional; several axisymmetric situations also occur in non self–gravitating flows around slowly rotating compact objects, when the radiation field is non–spherical, but the background metric can still be approximated as spherical. Also, magnetic fields may introduce asphericity in the radiation field and accretion onto magnetic stars can be funnelled onto polar caps, eventually producing localized hot spots. Both these magnetized situations can be described assuming axisymmetry in the radiation field. On the other hand, the application of the moment formalism to the bidimensional case is numerically troublesome, and involves the solution of complicated systems of partial differential equations. In this respect, characteristic methods seems to be more promising since they can be quite naturally extended to more than one spatial dimension, the major complication coming from the higher number of ordinary differential equations (ODEs) that must be solved to compute the characteristic trajectories.

Last but not least, the fact that characteristic approaches provide an exact solution for the photon distribution function is particularly appealing from the point of view of theoreticians. When using a moment expansion, a number of degrees of freedom is always introduced in the problem, due to the arbitrary choice of the closure functions. In the frequency–integrated problem this is probably not a too serious problem and the advantages of the method greatly outweight the disadvantages. In fact, in a wide number of applications, the influence of these degrees of freedom becomes quite unimportant when the system is truncated at higher order and, in the gray case, a large number of moments can be used

without a prohibitive computational cost (Turolla & Nobili, 1988). However, a recent investigation by Dullemond (1997b) shows that in particular dynamical situations, which are related to the presence of shocks, the solution to the finite (truncated) set of moment equations may become unconditionally singular when the velocity gradient of the medium exceeds a critical value. In particular, in regions of strong differential motion with a negative velocity gradient, the method of moments will also fail, no matter how large the order of truncation is. The situation is even more delicate when frequency–dependent transfer is tackled. In fact, to make the numerical solution affordable, only the first two moments can be taken into account, so that the choice of the closures has a non negligible impact on the results. Moreover, the extension of the moment formalism to the bidimensional case requires the specification of an increasing number of closure relations, making the method unacceptably dependent on the choice of a large number of free functions. The amount of degrees of freedom put into the investigation can be as big as the amount of dependent variables one likes to solve for, making the full approach questionable.

In this thesis we present a new, fully characteristic approach for the solution of the transfer problem. The formalism will be described in its more general form; results are then specialized to stationary, spherically–symmetric or plane–parallel configurations. A numerical code has been developed, and solutions for both the radiation field in a fixed background or for the full radiation–hydrodynamical problem have been obtained in spherical and plane-parallel geometry. In order to obtain a detailed description of the microphysics, particular care is devoted to the evaluation of the source term taking into account for the main radia-

tive processes that take place in astrophysical flows. As first step we present a method for the numerical evaluation of $e^- - p$, $e^- - e^-$ bremsstrahlung, Thomson and Compton scattering. In particular, Compton terms are directly calculated from integrals of the Compton scattering kernel, without resorting to the Kompaneets approximation. Radiative effects due to magnetic fields are neglected. Chapters 2, 3, 4 of this thesis contain the description of both the theoretical formalism and the numerical code, and conclude the first part of the work here presented.

Using the numerical techniques previously described, different models for accretion onto black holes and neutron stars are investigated. This is the topic of the second part of this thesis, in which we report the astrophysical results. As first application we present a spectral analysis of spherical, stationary accretion onto non–rotating black holes. This problem has been throughly investigated in the past (see e.g. Nobili, Turolla and Zampieri 1991, hereafter NTZ91 and reference therein) and represents a classical application of relativistic radiation transfer in differentially–moving media. The accreting matter reaches, in fact, not only $r/r_g \sim 1$ (here r_g is the gravitational radius) with $v/c \sim 1$, but, often, temperatures high enough ($T \gtrsim 10^9$ K) to make a full treatment of Comptonization necessary. As pointed out by NTZ, a distinctive feature of black hole accretion is the presence of a bimodal behaviour. In fact, for the same value of the accretion rate $\dot{m}$ which is the only free parameter, two solutions may coexist: a "cold", low–luminosity and a "hot", high–luminosity one. NTZ investigation was restricted to the frequency–integrated case. However, making use of an approximated treatment of Comptonization, they concluded that the two branches

of solution are expected to be characterized by very different spectral properties. Roughly speaking, the 'cold' one is characterized by low temperature and negligible Comptonization, the second by high luminosity and strong Comptonization. We reconsidered these two regimes, deriving the spectral properties in both cases (Chapter 5). Solutions are obtained numerically, and the radiation field is computed by using the characteristic code previously described.

For near–Eddington accretion, low–luminosity solutions start to develop an inner region optically thick to both free–free and scattering. Under these conditions, bulk motion Comptonization in the converging flow (Blandford & Payne 1981a, b; Payne & Blandford 1981, PB in the following; Nobili, Turolla & Zampieri 1993) acts efficiently at high frequencies where true absorption is very low. The synthetic spectrum derived via a numerical analysis shows some distinctive, intrinsically relativistic features and motived a reconsideration of the effects of dynamical comptonization, even from an analytical point of view. The result of our analysis, that is an extension of the Payne & Blandford investigation to the relativistic regime and includes the analysis of the wind problem, is reported in Chapter 6.

We have recently reconsidered the reprocessing of thermal radiation in geometrically thin, static atmospheres around accreting neutron stars. As in the case of black hole accretion, at high luminosities ($L \gtrsim 10^{36}$ erg/s) the equilibrium solutions show a bimodal behaviour and a hot, strongly comptonized state coexist with a cold one for the same values of the model parameters (see Turolla *et al.* 1994). We present an analysis of the spectral properties of the cold solution, extending previous results by Zel'dovich, & Shakura (1969,

ZS) and Alme, & Wilson (1973, AW) to cover the low luminosities ($L \lesssim 10^{34}$ erg/s) typical of old, isolated neutron stars (ONSs) accreting the interstellar medium ($L \lesssim 10^{34}$ erg/s). We found that, as the luminosity decreases, the emergent spectrum shows a significant hardening with respect to the blackbody at the neutron star effective temperature. This result has been first derived using a moment formalism for the solution of the radiation field, and then confirmed with the characteristic code (Chapter 7).

In order to obtain a solutions in the high–energy regime, we extended our first version of the code, including radiative processes as $e^+ - e^+$, $e^- - e^+$, $e^+ - p$ bremsstrahlung, and pair production-annihilation, typical of relativistic plasmas. Using this algorithm, we analized the spectral properties of the 'hot' solution, and we investigated the possibility to drive on–off transitions between the two branches. This possibility is particularly appealing from the observational point of view: the onset of the "hot" state represents a possible physical mechanism for producing efficiently high–energy radiation from weakly magnetized, accreting neutron stars and may be of interest in connection with hard X–ray transients, at present observed with SIGMA and BATSE. This is the topic of Chapter 8.

Finally, in Chapter 9 we briefly review some observational consequences related to the spectral properties of the cold solution around neutron stars. As first anticipated, our analysis shows that the hardening factor of the emitted spectrum becomes more pronounced at low luminosities. This circumstance has important consequences and stimulated a lot of work aimed to the observability of single ONSs accreting the ISM with X–ray and UV detectors on board ROSAT and EUVE.

In order to estimate their collective emission, a numerical code for the integration of stellar orbits in the Galactic potential well has been constructed: following the evolution of the distribution function over the Galaxy lifetime, we obtained the phase–space distribution of galactic ONSs. Results are then used together with the synthetic spectra to estimate the ONSs contribution to the unresolved soft X–rays background in the $0.5 - 2$ keV band. Performing a similar analysis, we have also shown that ONSs accretion luminosity can account for a sizable fraction, possibly most, of the diffuse soft X–ray emission observed in the direction of the Galactic Center.

To conclude, a critical analysis of the main hypothesis under which these results have been derived and a review of the present status of observations follow.

2 Radiative Transfer

In this chapter we introduce some general concepts in relativistic radiative transfer theory, the fundamental variables, the basic equation together with the approaches to its solution and our notation. In section 2.1 we discuss the structure of the radiative transfer equation in the comoving frame. Section 2.2 contains a review of the PSTF moment formalism (Thorne 1981, hereafter Th81), while in section 2.3 we present our treatment of the characteristic method (CRM). In order to shed light on their capabilities and limitations, both methods will be first described in the more general case, when no symmetries are present, and then specialized to symmetric configurations.

Unless otherwise stated, geometrized units ($c = G = h = 1$) are used throughout and lengths are in units of the gravitational radius $r_g = 2M$. Our choice of units for the PSTF moments will be ergcm^{-3}Hz^{-1}. All bold–face symbols denote four–vectors, four–vectors that are orthogonal to some fiducial four–velocity are regarded as three–vectors. We use a signature -+++, latin indices range from 0 to 3, while greek indices go from 1 to 3.

2.1 The Radiative Transfer Equation

As it is well known, in the standard classical theory of radiative transfer the radiation field is well described by taking as macroscopic independent variable the specific intensity I_ν. However, when relativistic transfer is tackled and a covariant formulation is needed, a more natural dependent variable is the occupation number of the photons' quantum mechanical states, N or, equivalently, the photon distribution function in the phase–space, f. This is because, at variance with I_ν, N and f are relativistic invariants. If the radiation is unpolarized, i.e. if N is independent of polarization, the number density of states in phase space is $2/h^3$ and $f = 2N/h^3 = c^2 I_\nu/h^4\nu^3 = I_\nu/\nu^3$, where ν is the photon frequency.

The relativistic transfer equation, written in covariant form, is an evolution equation for the photon distribution function $f(\mathbf{x}, \mathbf{p})$ that reproduces the standard non–relativistic equation if is expressed in a flat space–time or in a global Lorentz frame:

$$\frac{df}{d\xi} = g(\mathbf{x}, \mathbf{p}, f) \tag{2.1}$$

Here $\mathbf{p} \equiv d\mathbf{x}/d\xi$ is the photon 4–momentum, ξ is an affine parameter along the null geodesic and the collisional term g accounts for the interactions between matter and radiation (see e.g. Lindquist 1966, Th81). We stress that the differential operator in equation (2.1) acts not merely in spacetime but in the full photon phase–space, made up by the spacetime plus the null tangent space at each point along the photon trajectory. Since $f(\mathbf{x}, \mathbf{p})$ is a relativistic invariant, equation (2.1) holds in any frame and, in absence of interactions, the photon occupation number is conserved along each photon trajectory. However, the material properties (e.g. opacity and emission coefficients, scattering cross–section), which

enter the expression of the source term g, are naturally defined with respect to observers who are locally and instantaneously at rest with the matter (LRF). In the following we adopt a fiducial observer comoving with the fluid, which carries a tetrad $\mathbf{e}_{\hat{a}}$ and has 4–velocity $\mathbf{u} \equiv \mathbf{e}_{\hat{0}}$.

If spacetime, matter and radiation share some common symmetries, the orientation of some of the spatial vectors of the tetrad follows in a natural way. For example, in spherical symmetry, as it will be discussed in detail later on, it is convenient to chose $\mathbf{e}_{\hat{1}}$ orthogonal to the θ and ϕ coordinate directions. With respect to the tetrad, the components of the photon 4–momentum can be written as

$$p^{\hat{a}} = (E, E\mu, E(1-\mu^2)^{1/2}\cos\Phi, E(1-\mu^2)^{1/2}\sin\Phi) \tag{2.2}$$

where E is the photon energy, μ is the cosine of the angle between the photon direction and $\mathbf{e}_{\hat{1}}$, and Φ is the corresponding azimuthal angle, all measured in the LRF. The three quantities E, μ and Φ have an immediate physical meaning and they will be used as independent variables (momentum variables) together with the spacetime coordinates x^i to tick events on the light–cone of the phase–space. Because $\mathbf{p}$ is a null vector, it has only three independent components. It follows that, in the most general case, the distribution function in the phase space depends on 7 variables

$$f = f(x^i, E, \mu, \Phi)\,, \tag{2.3}$$

and 7 partial derivatives appear in the original differential operator. The total derivative

in equation (2.1) can be explicitated as

$$\begin{aligned} \frac{\partial f}{\partial x^i}p^i \quad &+ \quad \frac{\partial f}{\partial p^{\hat{a}}}\frac{dp^{\hat{a}}}{d\xi} = \\ \frac{\partial f}{\partial x^i}p^i \quad &- \quad \frac{\partial f}{\partial p^{\hat{a}}}\Gamma^{\hat{a}}_{\hat{b}\hat{c}}p^{\hat{b}}p^{\hat{c}} = g\,, \end{aligned} \tag{2.4}$$

where $p^i = p^{\hat{a}}e^i_{\hat{a}}$, $\Gamma^{\hat{a}}_{\hat{b}\hat{c}} = e^{\hat{a}}_i e^j_{\hat{b}} e^i_{\hat{c};j}$ are the Ricci rotation coefficients and the equations of the null geodesic have been used. We note that all the information about the spacetime curvature and the flow dynamics are contained in the tetrad field and enter the Boltzmann equation via the tetrad vectors themselves and their local rates of change which appear in the Ricci coefficients.

On the other hand, all information about the input physics are contained in the source term. From the mathematical point of view, the main complication arises because g may contain terms involving integrals of f. Just to give an example, even restricting to the simple case in which only isotropic, coherent scattering is accounted for, the expression of g depends on the monochromatic mean intensity

$$J_\nu = \frac{1}{4\pi}\int I_\nu d\Omega = \frac{1}{4\pi}\int f\nu^3 d\Omega\,. \tag{2.5}$$

As a consequence, the evaluation of the radiation field in a scattering medium relies on the numerical solution of a multi–dimensional integro–differential equation.

Moreover, in a realistic model, the influence of radiation on the hydrodynamical and thermal behaviour of the system, together with the backreaction of the gas on the radiation field must be self–consistently accounted for. The full solution of the radiation hydrodynamical problem requires the simultaneous integration of the transfer equation together

with the Euler, continuity and energy equations that, in turn, depend on the gray mean intensity J and on the mean gray radiative flux H:

$$J = \frac{1}{4\pi}\int_0^\infty d\nu \int I_\nu d\Omega = \frac{1}{4\pi}\int_0^\infty d\nu \int f\nu^3 d\Omega \tag{2.6}$$

$$H = \frac{1}{4\pi}\int_0^\infty d\nu \int I_\nu \mu d\Omega = \frac{1}{4\pi}\int_0^\infty d\nu \int f\nu^3 \mu d\Omega\,. \tag{2.7}$$

The coupled solution of the transfer and gasdynamical equation poses, therefore, the same difficulty encountered in the integration of the transfer equation alone in presence of scattering.

2.2 The PSTF Moments Expansion

As previously discussed, we use two different approaches to the solution of the relativistic transfer problem. In this section we describe the PSTF moments formalism, first introduced by Th81, with the purpose to outline some basic concepts together with the main advantages and disadvantages of the method.

The formalism is particularly elegant and represents a covariant generalization of the standard approach used in classical radiative transfer theory (see e.g. Chandrasekhar 1960). The basic idea is to introduce some kind of expansion for the dependence of the photon distribution function on the photon propagation direction. The coefficients of this expansion are just the moments of f, i.e. the angular averages of f weighted over the basis functions. The second step consists in performing the same kind of averages in the Boltzmann equation. In such a way, the original integro–differential Boltzmann equation can be reduced to a

recursive, infinite system of partial differential equations where the new unknowns variables are the moments of f.

Obviously, in order to make a numerical solution possible, the expansion must be truncated at a given, finite order. Nevertheless, the counterpart is that the dimensionality of the problem is highly reduced: now, in fact, the unknown variables (i.e. the moments) only depend on spacetime location and on the photon frequency. In many situations this approximate treatment is fully satisfactory and the application of this method allow a fast, direct solution of the full radiation hydrodynamical problem with a relatively low computational cost.

In this section we will focus on the mathematical structure of the moments equations, while the discussion of the explicit expression of the source term will be postponed to Chapter 3. Although the original treatment by Th81 is fully covariant, we restrict our attention on the derivation of the set of comoving moments equations, so that the four–velocity $\mathbf{u}$ of our fiducial observer coincides with the flow velocity. Let us also introduce the tensor

$$P^{ij} = g^{ij} + u^i u^j \,, \tag{2.8}$$

where g^{ij} are the metric coefficients; P^{ij} is the operator which projects orthogonal to $\mathbf{u}$. As it is well known, as a photon travels along its trajectory, the frequency measured in the comoving frame varies due to the observer 4–acceleration $\mathbf{a}$, expansion Θ and shear σ_{ij}. These quantities appear explicitily in the covariant derivative of the 4–velocity, that can be

written as (see e.g. Misner, Thorne & Wheeler 1973, MTW)

$$u_{i;j} = -a_i u_j + \frac{1}{3}\Theta P_{ij} + \sigma_{ij} + \omega_{ij}\,, \tag{2.9}$$

where ω_{ij} is the vorticity.

Following Th81, let us now to consider an event $\mathcal{P}$ in spacetime and define the kth moment of the photon distribution function by an integral over the photon 4–momentum lying on the future light cone at $\mathcal{P}$:

$$M_\nu^{A_k} \equiv M_\nu^{a_1\ldots a_k} = \int \frac{2N\delta\left(\mathbf{p}\cdot\mathbf{u}+\nu\right)}{\left(-\mathbf{p}\cdot\mathbf{u}\right)^{k-2}} p^{a_1}\ldots p^{a_k} dV_{\mathbf{p}}\,. \tag{2.10}$$

Here $\delta(x)$ is the Dirac delta–function, A_k denotes the string of indices $a_1\ldots a_k$, the pedix "ν" indicates the dependence on the photon frequency, and $dV_{\mathbf{p}}$ is the invariant volume element on the light cone. In particular, in the comoving frame it is

$$dV_{\mathbf{p}} = \left(-\mathbf{p}\cdot\mathbf{u}\right) d\Omega d\left(-\mathbf{p}\cdot\mathbf{u}\right)\,, \tag{2.11}$$

where $\int ..d\Omega$ denotes integration over the solid angle on the unit sphere in the projected tangent space. If we indicate by $\mathbf{n}$ an arbitrary unit vector on this sphere, the null vector $\mathbf{p}$ can be written as

$$\mathbf{p} = \left(-\mathbf{p}\cdot\mathbf{u}\right)\left(\mathbf{u}+\mathbf{n}\right)\,. \tag{2.12}$$

Substituting expressions (2.11), (2.12) together with the definition of I_ν into (2.10) yields

$$M_\nu^{a_1\ldots a_k} = \int I_\nu \left(n^{a_1}+u^{a_1}\right)\ldots\left(n^{a_k}+u^{a_k}\right) d\Omega\,. \tag{2.13}$$

This is the covariant generalization of the standard moments of the specific intensity introduce by Th81. The integration is over the photon propagation directions, and I_ν must be

regarded as a function of spacetime location $\mathcal{P}$, $\mathbf{n}$ and ν. In a similar way, it is possible to introduce the moments $S_\nu^{a_1..a_k}$ of the source function

$$\begin{aligned} S_\nu^{a_1...a_k} &= \int \frac{g\delta(\mathbf{p}\cdot\mathbf{u}+\nu)}{(-\mathbf{p}\cdot\mathbf{u})^{k-2}} p^{a_1}...p^{a_k} dV_{\mathbf{p}} \\ &= \nu^3 \int g\,(n^{a_1}+u^{a_1})...(n^{a_k}+u^{a_k})\,d\Omega\,. \end{aligned} \tag{2.14}$$

The explicit derivation of the correspondent recursive system of moments equations is possible and has been done (see again Th81). The calculation can be performed via direct substitution of the definitions (2.13), (2.14) in the successive moments of the transfer equation, or, alternatively, evaluating the divergence of $M_\nu^{A_k b}$ in a local Lorentz frame. The resulting equations have the structure

$$E_\nu^{A_k} \equiv M_\nu^{A_k b}{}_{;b} - \left(\frac{\partial}{\partial\nu}\right)\left(\nu M_\nu^{A_k bc} u_{b;c}\right) - (k-1)\,M_\nu^{A_k bc} u_{b;c} - S_\nu^{A_k} = 0\,. \tag{2.15}$$

However, this system is highly redundant, because the unprojected moment of order k, $M_\nu^{A_k}$, contains within itself full information about the values of all moments of lower order. The complication can be overcome by making use of the 'projected, symmetric, trace–free' (PSTF) tensors, since the only new information contained in the kth moment is its PSTF part. To be more precise, for a given tensor C^{A_k}, the PSTF part (here indicated with capital script letters)

$$\mathcal{C}^{a_1..a_k} \equiv (C^{a_1..a_k})^{PSTF} \tag{2.16}$$

can be evaluated by successive applications of three tensorial operations. The first one is the projection onto the local fluid–frame spatial hypersurface

$$(C^{a_1..a_k})^P \equiv P_{b_1}^{a_1}...P_{b_k}^{a_k} C^{b_1..b_k} \tag{2.17}$$

the second is the symmetrization

$$(C^{a_1..a_k})^S \equiv C^{(a_1..a_k)}\,, \tag{2.18}$$

and the last one is the construction of the 'trace–free' part

$$(C^{a_1..a_k})^{TF} \equiv \sum_{i=0}^{[k/2]} d_{ki} P^{(a_1 a_2}...P^{a_{2i-1}a_{2i}} C^{a_{2i+1}a_k)b_1...b_i}{}_{b_1...b_i}\,. \tag{2.19}$$

In the last expression $[k/2]$ denotes the largest integer less or equal to $k/2$ and

$$d_{ki} = (-1)^i \frac{k!\,(2k-2i-1)!!}{(k-2i)!\,(2k-1)!!\,(2i)!!}\,. \tag{2.20}$$

By making use of these definitions, it is possible to evaluate the PSTF moments of both the photon distribution function, $\mathcal{M}_\nu^{A_k} \equiv (M_\nu^{A_k})^{PSTF}$, and the source term, $\mathcal{S}_\nu^{A_k} \equiv (S_\nu^{A_k})^{PSTF}$. In particular, $\mathcal{M}_\nu^{A_k}$ will play the role of dependent variables in the resulting, non–redundant, system of differential equations.

The final result is

$$\begin{aligned}
\mathcal{E}^{A_k} &= \left\{\mathcal{M}_\nu^{A_k b}{}_{;b} + \mathcal{M}_\nu^{A_k}{}_{;b}u^b + \frac{k}{2k+1}\left[\mathcal{M}_\nu^{A_{k-1};a_k} - \left(\frac{k-1}{2k-1}\right)\left(\mathcal{M}_\nu^{A_{k-2}b}{}_{;b} - \mathcal{M}_\nu^{A_{k-2}b}a_b\right)\right.\right. \\
&\times \left.\left. P^{a_{k-1}a_k}\right] - (k-1)\mathcal{M}_\nu^{A_k bc}\sigma_{bc} - (k-1)\mathcal{M}_\nu^{A_k b}a_b + \frac{4}{3}\mathcal{M}_\nu^{A_k}\Theta \right. \\
&+ \frac{5k}{2k+3}\left[\mathcal{M}_\nu^{A_{k-1}b}\sigma_b^{a_k} - \left(\frac{k-1}{2k-1}\right)\mathcal{M}_\nu^{A_{k-2}bc}\sigma_{bc}P^{a_{k-1}a_k}\right] - k\mathcal{M}_\nu^{A_{k-1}b}\omega_b^{a_k} \\
&+ \frac{k\,(k+3)}{2k+1}\left[\mathcal{M}_\nu^{A_{k-1}}a^{a_k} - \left(\frac{k-1}{2k-1}\right)\mathcal{M}_\nu^{A_{k-2}b}a_b P^{a_{k-1}a_k}\right] \\
&+ \frac{(k-1)\,k\,(k+2)}{(2k-1)\,(2k+1)}\left[\mathcal{M}_\nu^{A_{k-2}}\sigma^{a_{k-1}a_k} - \frac{2\,(k-2)}{2k-1}\mathcal{M}_\nu^{A_{k-3}b}\sigma_b^{a_{k-2}}P^{a_{k-1}a_k}\right. \\
&+ \left.\left.\frac{(k-2)\,(k-3)}{(2k-1)\,(2k-3)}\mathcal{M}_\nu^{A_{k-4}bc}\sigma_{bc}P^{a_{k-3}a_{k-2}}P^{a_{k-1}a_k}\right]\right\}^{PS} \\
&- \frac{\partial}{\partial\nu}\nu\left\{\mathcal{M}_\nu^{A_k bc}\sigma_{bc} + \mathcal{M}_\nu^{A_k b}a_b + \frac{1}{3}\mathcal{M}_\nu^{A_k}\Theta\right.
\end{aligned} \tag{2.21}$$

$$
\begin{aligned}
&+ \frac{2k}{2k+3}\left[\mathcal{M}_\nu^{A_{k-1}b}\sigma_b^{a_k} - \left(\frac{k-1}{2k-1}\right)\mathcal{M}_\nu^{A_{k-2}bc}\sigma_{bc}P^{a_{k-1}a_k}\right] \\
&+ \frac{k}{2k+1}\left[\mathcal{M}_\nu^{A_{k-1}a^{a_k}} - \left(\frac{k-1}{2k-1}\right)\mathcal{M}_\nu^{A_{k-2}b}a_b P^{a_{k-1}a_k}\right] \\
&+ \frac{(k-1)k}{(2k-1)(2k+1)}\left[\mathcal{M}_\nu^{A_{k-2}}\sigma^{a_{k-1}a_k} - \frac{2(k-2)}{2k-1}\mathcal{M}_\nu^{A_{k-3}b}\sigma_b^{a_{k-2}}P^{a_{k-1}a_k}\right. \\
&+ \left.\left.\frac{(k-2)(k-3)}{(2k-1)(2k-3)}\mathcal{M}_\nu^{A_{k-4}bc}\sigma_{bc}P^{a_{k-3}a_{k-2}}P^{a_{k-1}a_k}\right]\right\}^{PS} \\
&- \mathcal{S}_\nu^{A_k} = 0
\end{aligned}
$$

This is the most general set of moments equations, holding without any presupposed symmetry in the background metric, or in the velocity and radiation field. It must be noted that, when truncated, this system is not closed. The moments equation of order k depends on $\mathcal{M}_\nu^{A_{k+1}}$ and $\mathcal{M}_\nu^{A_{k+2}}$, so that a set of suitable closure conditions must be introduced for all components of these tensorial quantities. Since $\mathcal{M}_\nu^{A_k}$ has $2k+1$ independent components, even in the simple case in which only the first two moments equations are retained, 12 arbitrary functions must be introduced in the model. Moreover, in this general form the resulting system (2.21) still shows a very complicated mathematical structure that makes the numerical solution troublesome.

In the original paper by Th81 two additional variants of the formalism, specialized to particular situations, were presented: a frequency–integrated version and one holding in presence of a 'universal redshift function'. In both cases the main simplification is that the behaviour of the radiation field is regulated by a set of equations similar to (2.21), with all $\partial/\partial\nu$ terms absent. In the latter case the reason is that the frequency mixing can be removed by using a suitable "redshifted frequency" in lieu of the standard independent variable ν. This is possible in every situation in which the change of the photon energy from

event $\mathcal{P}$ to event $\mathcal{Q}$, as measured by the comoving observer, only depends on the spacetime coordinates. However, even in this simple case, the general formalism remains so messy that, up to now, it has never been applied to astrophysical situations.

A more important simplification in the mathematical structure arises when the formalism is specialized to problems sharing spherical, plane–parallel or pseudo–spherical symmetry. In these cases it is convenient to orient the first tetrad four–vector along the four–acceleration, $\mathbf{e}_{\hat{1}} \equiv \mathbf{a}/a$. With this choice, in fact, the fiducial congruence becomes irrotational, $\omega_{ij} = 0$, and the only non–vanishing components of the shear tensor can be expressed in term of one scalar quantity σ. As far as the velocity and gravitational field quantities are concerned, the simplified moment equations will depend on a, Θ, σ and on the extrinsic curvature $b = \Gamma_{212} = \Gamma_{313}$ of the bidimensional spatial hypersurfaces S_2 orthogonal to $\mathbf{u}$ and $\mathbf{a}$.

In addition, the isotropy of the radiation field on S_2 translates in a local axisymmetry of f and g which are now independent on the azimuthal angle Φ. This allows to compute all components of the tensors of order k in terms of one single scalar moment

$$w^k_\nu = \mathcal{M}^{\hat{1}\ldots\hat{1}}_\nu = 2\pi \frac{k!\,(2k+1)}{(2k+1)!!} \int I_\nu P_k(\mu) d\mu \,, \tag{2.22}$$

$$s^k_\nu = \mathcal{S}^{\hat{1}\ldots\hat{1}}_\nu = 2\pi \frac{k!\,(2k+1)}{(2k+1)!!} \int \nu^3 g P_k(\mu) d\mu \,, \tag{2.23}$$

where $P_k(x)$ is the Legendre polynomial of order k. The appearance of the Legendre polynomials in the formalism is not surprising: actually, the expansion of f in PSTF moments is equivalent to the more familiar expansion in spherical harmonics. As the local axisymmetry of the radiation field collapses the number of independent component of $\mathcal{M}^{A_k}_\nu$ from $2k+1$

down to a single one, the $2k+1$ spherical harmonics $Y_{km}(\theta,\Phi)$, with k fixed, all vanish for axial symmetry except Y_{k0}. This circumstance makes the full formalism completely scalar (i.e. only dependent on scalar variables). We note that the first three PSTF scalar moments are related to the more familiar, standard monochromatic moments J_ν, H_ν and K_ν by

$$w_\nu^0 = 4\pi J_\nu \quad w_\nu^1 = 4\pi c H_\nu \quad w_\nu^2 = 4\pi\left(K_\nu - \frac{1}{3}J_\nu\right).$$

The final expressions of the moments equations are

$$\begin{aligned} & w_\nu^{k+1}{}_{,\hat{1}} + [(2-k)\,a + (2+k)\,b]\,w_\nu^{k+1} + w_\nu^{k+1}{}_{,\hat{0}} + \left[\frac{4}{3}\Theta + \frac{5k\,(k+1)}{2\,(2k-1)\,(2k+3)}\sigma\right] w_\nu^k \\ & + \frac{k^2}{(2k-1)\,(2k+1)} w_\nu^{k-1}{}_{,\hat{1}} + \frac{k^2\,[(k+3)\,a + (1-k)\,b]}{(2k-1)\,(2k+1)} w_\nu^{k-1} \\ & - \frac{3}{2}(k-1)\,\sigma w_\nu^{k+2} + \frac{3\,(k-1)^2\,k^2\,(k+2)}{2\,(2k-3)\,(2k-1)^2\,(2k+1)}\sigma w_\nu^{k-2} \\ & - \frac{\partial}{\partial\nu}\left\{ a w_\nu^{k+1} + \left[\frac{1}{3}\Theta + \frac{k\,(k+1)}{(2k-1)\,(2k+3)}\sigma\right] w_\nu^k + \frac{k^2}{(2k-1)\,(2k+1)} a w_\nu^{k-1} \right. \\ & \left. + \frac{3}{2}\sigma w_\nu^{k+2} + \frac{3\,(k-1)^2\,k^2}{2\,(2k-3)\,(2k-1)^2\,(2k+1)}\sigma w_\nu^{k-2} \right\} = s_\nu^k . \end{aligned} \tag{2.24}$$

Explicit expressions of the 6 quantities

$$w_\nu^k{}_{,\hat{1}} \quad w_\nu^k{}_{,\hat{0}} \quad \Theta \quad a \quad \sigma \quad b$$

have been reported by Th81 for spherical flows in both Schwarzschild and flat spacetime and for planar flows in flat spacetime.

In its scalar variant, the method has been fruitfully used to investigate a variety of astrophysical situations. It has been probed to be a fast, powerful tool for tackling problems of relativistic radiation hydrodynamics for 1–dimensional flows, at least when the expansion is truncated at $k = 1$ and only the first two moments equations are solved. Stationary, gray

and frequency dependent applications has been presented by many authors (see e.g. Thorne, Flammang & Żytkow 1981, Nobili, Turolla & Zampieri 1991, 1993, Zampieri *et al.* 1995, Dullemond 1996a, Shemi 1994), while the time–dependent, frequency–integrated case was recently considered by Rezzolla & Miller (1994, 1996), Miller & Rezzolla (1995), Zampieri, Miller & Turolla (1996), Rezzolla (1996). The role of the closure functions and the behaviour of the critical points in the frequency integrated, stationary system were analized by Turolla & Nobili 1988, Dullemond 1996b.

However, even in presence of symmetries, the construction of numerical models involves the solution of a complicated system of partial differential equations. The choice of boundary conditions is very delicate and, in some regimes, the problem can be computationally challenging. Moreover, the structure of the differential operator depends on both the expression of the source term and the choice of the closure conditions. A general analysis of its mathematical character is not possible "a priori", depending on the input physics included in the problem, but some particular cases has been studied by Turolla, Zampieri, Nobili (1995). As they showed, in Comptonized converging flows or when gravity is taken into account, the behaviour of the operator could be very complex and the system of equations may become of the mixed type, switching from hyperbolic to elliptic.

2.3 The Characteristics Approach

In this section we present our approach for solving the transfer equation using a fully characteristics method. This chapter contains the description of the formalism, while in

chapters 3 and 4 we will present the treatment of the radiative processes and a detailed description of our numerical code. All these results, together with applications reported in Chapter 5 of this thesis, have been published in Zane *et al.* 1996a.

As it was already outlined, when using characteristic approaches the main idea is to reconsider the Boltzmann equation in its original form

$$\frac{df}{d\xi} = g(\mathrm{x}, \mathrm{p}, f)\,, \tag{2.25}$$

and to integrate it directly, as ordinary differential equation, using the parameter ξ as the independent variable. Clearly the differential operator in the transfer equation is Pfaffian, so it is always possible to solve the Boltzmann equation along its characteristic directions, i.e. along the photon trajectories in the 7–dimensional phase–space.

In the non–relativistic, static limit trajectories are simply parallel straight lines, while for moving media characteristic rays depart from these lines and must be in general evaluated numerically. For a given background metric and a given velocity field, their structure can be obtained by solving a system of 7 ordinary differential equations, which must be coupled with equation (2.25). To be more precise, the run of the spacetime coordinates along the photon trajectory is derived by solving the four equations

$$\frac{dx^i}{d\xi} = p^i = p^{\hat{a}} e^i_{\hat{a}}\,, \tag{2.26}$$

while the variation of E, μ and Φ can be obtained from the equation of the null geodesic, written in terms of $p^{\hat{a}}$

$$\frac{dp^{\hat{a}}}{d\xi} = -\Gamma^{\hat{a}}_{\hat{b}\hat{c}} p^{\hat{b}} p^{\hat{c}}\,. \tag{2.27}$$

Recalling the expression of $p^{\hat{a}}$ given in equation (2.2), the last three equations can be explicitly written as

$$\frac{dE}{d\xi} = -\Gamma^{\hat{0}}_{\hat{b}\hat{c}} p^{\hat{b}} p^{\hat{c}} \tag{2.28}$$

$$\frac{d\mu}{d\xi} = -\frac{1}{E}\left(\Gamma^{\hat{1}}_{\hat{b}\hat{c}} - \mu\Gamma^{\hat{0}}_{\hat{b}\hat{c}}\right) p^{\hat{b}} p^{\hat{c}} \tag{2.29}$$

$$\frac{d\Phi}{d\xi} = -\frac{1}{E(1-\mu^2)^{1/2}}\left(\cos\Phi\Gamma^{\hat{3}}_{\hat{b}\hat{c}} - \sin\Phi\Gamma^{\hat{2}}_{\hat{b}\hat{c}}\right) p^{\hat{b}} p^{\hat{c}}\,. \tag{2.30}$$

At variance with what happens using other methods, like for example expansion in PSTF moments, this kind of approach makes a great simplification in the mathematical structure of the problem: in fact, the non–grey problem can be solved without integration of complicated systems of partial differential equations. Moreover, no closure is needed and this formalism gives as result the full coordinate, frequency and angle dependent intensity. As we will discuss in detail in the next section, it is just the knowledge of the angular dependence of the distribution function, lost when the moments of f are used as dependent variables, that makes possible to use the characteristic rays method to describe anisotropic radiative processes, as Compton scattering, in their more general form. Moreover, this approach naturally preserves the hyperbolic character of the Boltzmann equation.

The main drawback of the method is related to the fact that, to ensure a sufficient resolution in f, a very large number of characteristic rays must be used. In some sense, characteristic codes solve the microscopic behaviour of photons, so that they require a large amount of sample rays. From the computational point of view, this approach is surely more time–consuming with respect to other techniques based on suitable expansions of f and the situation may be particularly delicate in radiation–hydrodynamical calculations (see

Dullemond 1996a for a discussion about this point).

Nevertheless, we stress the fact that the formalism is completely general, holding in any differentially moving media in a curved spacetime. The only complication is in the total number of ordinary differential equations that must be integrated numerically and in the storage and handling of large matrices for f. Computer modeling of multidimensional systems is a rapidly advancing science, and we believe that the method is particularly promising to explore stationary radiation hydrodynamical problems.

Clearly, its capabilities are exploited at best in presence of symmetries, when the dimensionality is reduced. In addition, the existence of conserved quantities allows to derive analytical expressions for the photon trajectories in phase space, lowering the computational cost. Since the numerical code and all applications presented in this thesis will deal with symmetric configurations, in the following we will focus on these cases only.

2.3.1 Transfer in Spherically–symmetric Spacetimes

Let us consider the more general spherically–symmetric spacetime, described, in spherical coordinates, by the line–element

$$ds^2 = g_{00}(r,t)dt^2 + g_{11}(r,t)dr^2 + r^2(d\theta^2 + \sin^2\theta d\phi^2)\,. \tag{2.31}$$

Spherical symmetry implies that there exist two constants of the motion, L_z and L, which are related to the components of the photon 4–momentum by $L_z = p_3 = r^2\sin^2\theta p^3$, $L^2 = r^4[(p^3)^2\sin^2\theta + (p^2)^2]$. These two expressions take a very simple form, and lead to a major simplification in the transfer equation, if the fluid configuration and the radiation field are

themselves spherically–symmetric. In this case the spatial 3–velocity $\vec{v}$ of the comoving observer, measured by the stationary observer $\delta^i_0/\sqrt{-g_{00}}$, is in the radial direction and the most convenient choice for the tetrad is

$$\begin{aligned} e^i_{\hat{0}} &= \left(\frac{\gamma}{\sqrt{-g_{00}}}, \frac{\gamma v}{\sqrt{g_{11}}}, 0, 0\right) \\ e^i_{\hat{1}} &= \left(\frac{\gamma v}{\sqrt{-g_{00}}}, \frac{\gamma}{\sqrt{g_{11}}}, 0, 0\right) \\ e^i_{\hat{2}} &= (0, 0, r^{-1}, 0) \\ e^i_{\hat{3}} &= (0, 0, 0, r^{-1}\sin^{-1}\theta) \end{aligned} \tag{2.32}$$

where $\gamma = (1 - v^2)^{-1/2}$. The constants L_z and L may be then expressed in terms of the tetrad components $p^{\hat{a}}$ as

$$L_z = L \sin\Phi \sin\theta \tag{2.33}$$

$$L^2 = r^2 E^2 (1 - \mu^2)\,. \tag{2.34}$$

In spherical symmetry, the photon distribution function must be independent on both the polar angles ϕ and θ. Since, from equation (2.33), we have $\Phi = \Phi(\theta)$, it follows that isotropy in coordinate space implies also that $\partial f/\partial\Phi = 0$ and the Boltzmann equation reduces to

$$\frac{\partial f}{\partial t}p^0 + \frac{\partial f}{\partial r}p^1 + \frac{\partial f}{\partial E}\frac{dE}{d\xi} + \frac{\partial f}{\partial \mu}\frac{d\mu}{d\xi} = g\,. \tag{2.35}$$

In the further hypothesis that the spacetime is stationary, the existence of a time–like Killing vector provides a third conserved quantity, $p_0 \equiv -E_\infty$, which can be used to obtain a simple expression for the photon energy along each ray in the LRF

$$E = \frac{E_\infty}{y(1 + \mu v)}\,; \tag{2.36}$$

in the previous expression $y = \gamma\sqrt{-g_{00}}$ is the specific energy of the fluid, as measured by a static observer at infinity.

In the case at hand, the photon trajectories lie in a 4–dimensional hypersurface and can be obtained solving equations (2.28) and (2.29) together with

$$\frac{dt}{d\xi} = p^0 = -\frac{E_\infty}{g_{00}} \tag{2.37}$$

$$\frac{dr}{d\xi} = p^1 = \frac{Ey}{r_g}(\mu + v)\,. \tag{2.38}$$

Actually, the existence of the two constants of motion L and E_∞ yields analytical expressions for both μ and E, as functions of r, along each photon trajectory:

$$\mu = \frac{-y^2 v b^2 \pm r\left(r^2 + b^2 g_{00}\right)^{1/2}}{r^2 + b^2 y^2 v^2} \tag{2.39}$$

$$E = \frac{b^2 y^2 v^2 + r^2}{\left[r^2 \pm r v \left(r^2 + b^2 g_{00}\right)^{1/2}\right] y} E_\infty \tag{2.40}$$

where the impact parameter $b = L/E_\infty$ has been introduced. Due to spherical symmetry, only positive b's need to be considered, negative values of the angular momentum give exactly the specular picture, so in the following b^2 will be used as a parameter. It can be easily shown that the plus/minus sign in equations (2.39), (2.40) refers to photons for which $\mu + v$ is always positive/negative. This implies, see equation (2.38), that the radial coordinate is always increasing/decreasing along the path and that the condition $\mu + v = 0$ defines the locus of turning points for the trajectories. This is just a manifestation of aberration: the turning points, in fact, are located where the cosine of the angle between the photon and radial directions, measured by the stationary observer, vanishes.

In the following we will specialize on the vacuum Schwarzschild solution, and in this case

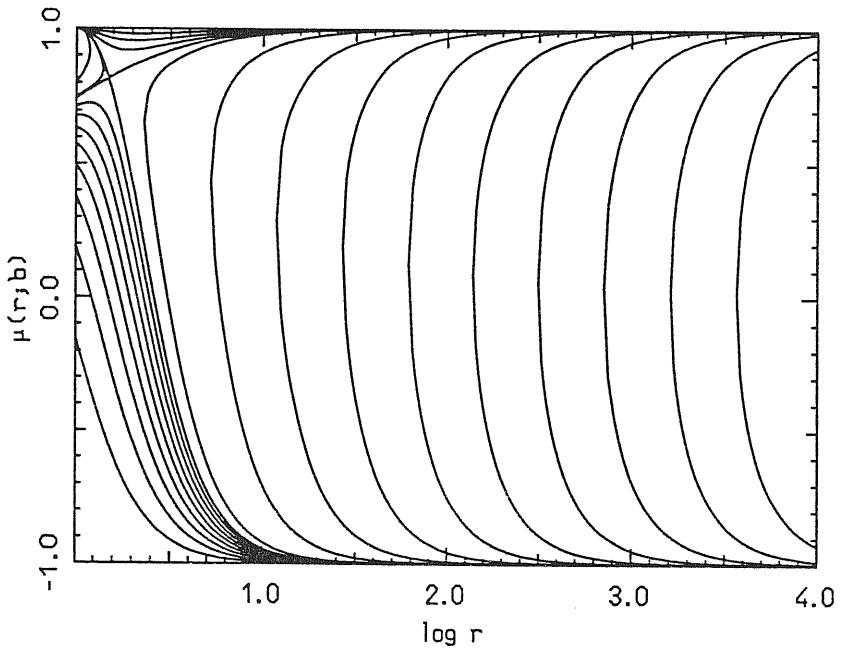

Figure 2.1: *The run of the cosine of the angle between the photon momentum and the radial direction, as measured by a free-falling observer, along the characteristic rays. Different curves correspond to different values of the impact parameter b.*

the structure of the photon trajectories in physical space is well known (see e.g. MTW). Without to enter in details, we just review here a few basic concepts that will be useful later on, when the numerical code will be described, for a better understanding of some technical points. Following MTW, the photon trajectories may be divided into three classes: a) those connecting radial infinity with the event horizon, characterized by impact parameters in the range $0 \leq b^2 < 27/4$; b) those that are trapped in the region $1 \leq r < 3/2$ and c) those for which it is always $r > 3/2$. Trajectories of the latter two types have $b^2 > 27/4$. The limiting value $b^2 = 27/4$ corresponds to the circular photon orbit. The plot of $\mu = \mu(r; b)$ and of $E/E_\infty = \epsilon(r; b)$ is shown in figures 2.1 and 2.2 for a free–fall velocity law, $u^1 = r^{-1/2}$.

As can be seen from the the figures, photons starting at the horizon can reach infinity

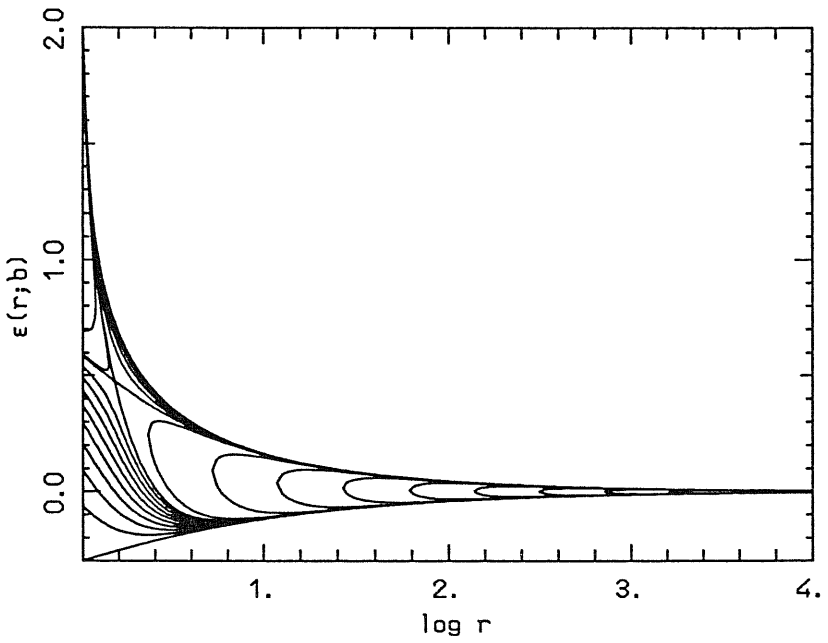

Figure 2.2: *Same as in figure 1a for the photon energy normalized with respect to* E_∞.

with non–zero energy only if they are emitted exactly in the radial direction ($\mu = 1$) with an infinite energy, while ingoing photons that leave infinity with zero angular momentum reach the horizon halving their initial energy. At large values of r all rays concentrate at $\mu = \pm 1$, as radial streaming is approached. Trajectories with an impact parameter equal to the critical value $b^2 = 27/4$ exhibit a saddle point at $r = 3/2$.

In the following we will concentrate on the case in which both matter and the radiation field are stationary. Under this assumption the distribution function depends only on three variables, r, E and μ, and since it is $E = E(r)$, $\mu = \mu(r)$ (see equations [2.39], [2.40]), the radial coordinate itself can serve as a (non–affine) parameter along the null geodesics. The Boltzmann equation can be then integrated in the domain of existence of each photon trajectory. This particular choice appears to be convenient for a number of reasons, although it poses some numerical problems, as it will be discussed later on. First of all, the treatment

of boundary conditions is much simpler when the radial coordinate is the independent variable and this avoids also the integration of equation (2.38) along with the transfer equation. Moreover, when scattering is taken into account, the source term depends on the integrals of f over angles, which must be evaluated at both constant r and E. The knowledge of $f(r)$ avoids the use of spline or other interpolation algorithms, which is time–consuming and would be needed in the case of a different parametrization of the photon trajectories. In conclusion, in differentially moving media in a curved spacetime, at least for what concerns the radiation field, the transfer problem can be solved integrating numerically the single differential equation

$$\frac{df}{dr} = \frac{r_g}{y(\mu + v)} \frac{g}{E} \tag{2.41}$$

for different values of the two parameters b and E_∞.

We outline that the existence of the three constants of the motion L_z, L, E_∞ only depends on the symmetry properties of the metric. Similar simplifications can therefore be introduced in all problems in which non self–gravitating matter in a Schwarzschild spacetime are considered. For example, in a stationary axisymmetric situation (e.g. accretion disks around non–rotating black holes) the distribution function depends on 5 variables

$$f = f(r, \theta, E, \mu, \Phi) \tag{2.42}$$

but it is possible to avoid the numerical integration of 3 characteristics equations exploiting the expressions of the conserved quantities.

In our first application we focus our attention on the calculation of the radiation field and, thus, we restrict our discussion to the case in which velocity, density and temperature

profiles are fixed *a priori*, similarly to what was done by Mihalas (1980) in the special relativistic case and Schinder & Bludman (1989) in the general relativistic, static case. A numerical technique for the solution of the integro–differential scattering equation is discussed in Chapter 3. The same method can be applied to the solution of the full radiation hydrodynamical problem and examples are presented in Chapter 7,8.

2.3.2 Boundary Conditions

Because there is not a one–to–one map between r and ξ, equation (2.41) must be integrated twice for each value of b^2, in correspondence with the two solutions for μ and E given by equations (2.39), (2.40). At the same time, two different boundary conditions for the distribution function f must be imposed, taking into account that the plus (minus) sign in equations (2.39), (2.40) corresponds to outgoing (ingoing) trajectories. The boundary condition for ingoing characteristics of type a) is prescribed in the standard way: for a non–illuminated atmosphere, for example, it is just $f = 0$ at the outer edge of the integration domain. This is also the only condition required to integrate the transfer equation along all characteristics of type c), since integration can be started at large r with, say, $f = 0$ and carried out until the turning point is reached storing the computed value of f, which is then used as the initial condition along the outgoing branch of the trajectory. The remaining rays, including characteristics of type b), can be treated much in the same way if there exists a region in the flow where the effective depth τ_{eff} becomes larger than unity at any frequency and LTE is attained. In this case, in fact, the required boundary condition is simply $f = B_\nu(T)/E^3$, $B_\nu(T)$ is the Planck function at temperature T, at a radius $\overline{r}$ such

that $\tau_{eff}(\bar{r}) > 1$.

Although this is the standard case for stellar atmospheres, including accretion flows onto compact stars, a different situation may arise when dealing with accretion onto black holes: for low values of the accretion rate, for example, the flow is optically thin all the way down to the horizon (see e.g. Nobili, Turolla & Zampieri 1991). Now a boundary condition for f must be imposed at $r = 1$ for rays starting at the event horizon. Since E goes to infinity there, both the distribution function and g must vanish. The product $E(\mu + v)$, however, does not vanish for all outgoing rays at the horizon, so $g = 0$ implies also $df/dr = 0$. In order to avoid numerical overflows, integration is started at a radius r_{in} fractionally larger than unity, with the regularity condition $df/dr = 0$. The two rays with $b^2 = 27/4$ are peculiar since they intersect at $r = 3/2$ (the saddle point) which is also a critical point for equation (2.41). We still integrate the transfer equation along these particular rays taking as a regularity condition $g = 0$ at $r = 3/2$. Strictly speaking, this condition is exact only in the case in which the effective optical depth is larger than unity at the last photon orbit; in other cases there is no physical reason to ask for thermalization and the value of f may be undetermined. However, since the radial derivative of f diverges at the critical point, we found that, in a finite differences numerical scheme, the solution of the differential equation relaxes fast and the final result is probably not strongly affected by the value of the distribution function at $r = 3/2$.

3 The Source Function

In this chapter we focus our attention on the source term corresponding to radiative processes of astrophysical relevance. We present the explicit expression of g together with the expressions of $\mathcal{S}_\nu^{A_k}$ that are needed when solving the moments equations. In the following we deal with an unmagnetized, fully ionized, non–degenerate hydrogen gas in which emitters and absorbers are in local thermal equilibrium at a temperature T, i.e. in which the Kirchoff law holds. We consider also the case in which electrons are relativistic ($T \gtrsim 5 \times 10^9$ K), and present a fully general treatment of Compton scattering. For the sake of simplicity, as a first step we focus our attention only on thermal emission and absorption together with scattering from free electrons and we do not include a discussion of other processes, as pair production and double Compton scattering, that may be relevant at such high temperatures. The numerical treatment of the Compton source term is described in detail, and in Chapter 5 we report some astrophysical applications. However we stress that the characteristics method we have presented is completely general and additional radiative processes may be easily included. Source terms not involving integrals of the photon distribution function can be simply accounted for once the corresponding emissivity and opacity

coefficients are provided. On the other hand, as it will be discussed later on, our iterative scheme allows for the solution of integro–differential equations and can be used to include also different integral source terms as, for instance, those related to pair production or bound–bound emission. Actually, a self–consistent treatment of pair production entails the solution of the full radiation hydrodynamical problem, with the addition of the pair balance equation and was left out on purpose in our first applications which are obtained keeping the hydrodynamics fixed.

In a second phase we implemented our code to account for photon–photon pair production–annihilation and, consistently, for $e^+ - e^+$, $e^- - e^+$, $e^+ - p$ bremsstrahlung. The method will be presented in Chapter 8.

In this section physical units are used; γ and τ denote the dimensionless photon energy and electron temperature, both in units of $m_e c^2$; $K_p(x)$ is the modified Bessel function of the second kind.

3.1 Thermal Bremsstrahlung

The source term for spontaneous emission and absorption, including stimulated emission, can be written as

$$g = \frac{\eta}{4\pi h c E^2} - \chi E f \,, \tag{3.1}$$

where η and χ are the emission and absorption coefficients, measured in the comoving frame. Because of the assumed equilibrium, Kirchoff law yields:

$$\frac{\eta}{4\pi\chi} = B_\nu(T) \tag{3.2}$$

with $\nu = E/h$. In the medium we are considering, the dominant true emission and absorption processes are electron–proton and electron–electron bremsstrahlung; in the following we will denote with $\kappa_{ff} = (\kappa_{ff})_{e^- - p} + (\kappa_{ff})_{e^- - e^-}$ the correspondent total opacity. The free–free contribution to the source term is then

$$\frac{g_{ff}}{E} = \varrho \kappa_{ff} \left(\frac{B_\nu}{hcE^3} - f \right) . \tag{3.3}$$

The photon spectrum from bremsstrahlung is usually described in terms of the velocity–averaged Gaunt factor G. Since the expression of G is not analytical, we used some suitable fitting formulae, derived from exact results in different regimes. In the non–relativistic regime, our fits were based on the tables for G presented by Karzas & Latter (1961). However, as discussed by Gould (1980), contributions to the total energy loss rate due both to relativistic corrections in the electron velocity distribution and to electron–electron bremsstrahlung are already of order 10 % at $T \sim 10^8$ K and become as large as 30 % at $T \sim 10^9$ K. Free–free emissivity from a relativistic thermal plasma has been investigated by several authors (see e.g. Alexanian 1968; Quigg 1968; Haug 1975; Gould 1980; Stepney & Guilbert 1983; Dermer 1984, 1986). The photon spectrum from $e^- - p$ emission involves a single quadrature over the relative Lorentz factor of the interacting particles γ_r (see e.g. Dermer 1986)

$$\eta_{e^- - p}(\gamma, \tau) = \frac{n_e n_p c}{\tau K_2(1/\tau)} \int_{1+\gamma}^{\infty} d\gamma_r \left(\gamma_r^2 - 1 \right) \frac{d\sigma_{B-H}(\gamma, \gamma_r)}{d\gamma} \exp\left(-\frac{\gamma_r}{\tau} \right) , \tag{3.4}$$

where $d\sigma_{B-H}(\gamma, \gamma_r)/d\gamma$ is the Bethe–Heitler cross section corrected for the Elwert factor (see e.g. Heitler 1936) and n_e, n_p are the number density of electrons and protons. The

previous expression holds for $\tau \ll m_p/m_e$, so that protons can assumed to be at rest in the lab–frame.

Electron–electron emissivity is more complicated since now both particles have the same mass and a quadrupole contribution appears. The standard expression involves a five–fold integral of the totally differential cross–section (Haug 1975), but, as shown by Dermer (1984, 1986), it can be reduced to a triple integral exploiting the covariance of Haug's formula to evaluate the cross–section in the CM–frame. The final result is

$$\begin{aligned} \eta_{e^-e^-}(\gamma,\tau) &= \frac{n_e^2 c}{4\tau K_2^2(1/\tau)} \int_1^\infty d\gamma_r \frac{(\gamma_r^2-1)}{[2\,(\gamma_r+1)]^{1/2}} \int_0^{\zeta(\gamma_r)} \frac{d\gamma^*}{\gamma^*} \frac{d\sigma^*_{e^-e^-}(\gamma^*,\gamma_r)}{d\gamma^*} \\ &\times \exp\left\{-\frac{[2\,(\gamma_r+1)]^{1/2}}{\tau}\left(\frac{\gamma^2+\gamma^{*2}}{2\gamma\gamma^*}\right)\right\} \end{aligned} \tag{3.5}$$

(see Dermer 1986 for notation).

The numerical evaluation of both η_{e^-p} and $\eta_{e^-e^-}$ poses no particular problems and has been carried out following Dermer (1986) in the ranges $2\times10^{-2} \le \tau \le 10$, $2\times10^{-2} \le h\nu/KT \le 25.12$. Numerical results for the total Gaunt factor were then fitted with the analytical function (see Stepney & Guilbert 1983)

$$G = \begin{cases} (A+Bx)\ln(1/x) + C + Dx, & x = h\nu/KT \le 2.51 \\ \\ \alpha x^2 + \beta x + \gamma + \delta/x, & x > 2.51, \end{cases}$$

deriving, for each τ, the set of coefficients $A,\ldots,\delta$. The Gaunt factor can be then obtained at any value of τ and $h\nu/KT$ by means of a suitable interpolation/extrapolation. At temperatures below $\sim$ 10 keV ($\tau \lesssim 0.01$), the asymptotic limits of Gould (1980) are used for both $e^- - p$ and $e^- - e^-$ emissivity.

Once $\eta = \eta_{e^--p} + \eta_{e^--e^-}$ is known, the correspondent total opacity is simply derived from the relation $\kappa_{ff} = \eta/(4\pi\varrho B_\nu)$.

Whenever, as in this case, the emission coefficient and the opacity are isotropic, the evaluation of the moments of the source term is straightforward. The quantities $\mathcal{S}_\nu^{A_k}$ turn out to be equal to an emissivity term plus a suitable opacity–weighted sums over the moments $\mathcal{M}_\nu^{A_k}$. In LTE it is

$$\mathcal{S}_\nu = \varrho k_{ff}(4\pi B_\nu - \mathcal{M}_\nu) \quad k = 0\,; \tag{3.6}$$

$$\mathcal{S}_\nu^{A_k} = -\varrho k_{ff}\mathcal{M}_\nu^{A_k} \qquad k \geq 1\,. \tag{3.7}$$

3.2 Electron Scattering

The second important radiative process we consider is scattering from free electrons: we recall that one of the major complications encountered in solving the transfer equation comes from its non–local character. In fact, even limiting to the coherent and isotropic case, the source term is

$$\frac{g_{es}}{E} = \varrho\kappa_{es}(j_\nu - f)\,, \tag{3.8}$$

where κ_{es} is the Thomson opacity and

$$j_\nu = \frac{1}{2}\int_{-1}^{1} f(r,\mu,E)d\mu \tag{3.9}$$

is the zero–th moment of the distribution function. Allowing for the more realistic case of Thomson scattering, the correspondent cross section has a monopole plus a quadrupole

angular dependence (see e.g. Chandrasekhar 1960) yielding

$$\frac{g_{es}}{E} = \varrho\kappa_{es}\left[\frac{3}{8}\left[(3j_\nu - k_\nu) - \mu^2\left(j_\nu - 3k_\nu\right)\right] - f\right], \tag{3.10}$$

where

$$k_\nu = \frac{1}{2}\int_{-1}^{1} f\left(r,\mu,E\right)\mu^2 d\mu\,. \tag{3.11}$$

The Thomson limit can be assumed to correctly describe electron scattering when the energy exchange in a single collision can be safely ignored. On the other hand, in high temperature regions non–conservative effects and quantum corrections play a fundamental role in shaping the emergent spectrum. The derivation of the general expression for the Compton source term can be found e.g. in Pomraning (1973) and is briefly outlined below, mainly to introduce some basic ideas which will be used later on when the numerical scheme is discussed. With reference to a single scattering, $\vec{n}$ denotes the incident photon direction and $\xi = \vec{n}\cdot\vec{n}'$, where primed quantities refer to the scattered photon. For an incident photon energy γ and an electron velocity $\vec{v}_e$, the Klein–Nishina formula gives the probability of scattering into the energy γ' and the direction $\vec{n}'$

$$\begin{aligned}\sigma\left(\gamma\rightarrow\gamma',\vec{n}\rightarrow\vec{n}',\vec{v}_e\right) &= \frac{r_0^2}{2\gamma\nu\lambda}\left\{1+\left[1-\frac{(1-\xi)}{\lambda^2 DD'}\right]^2+\frac{(1-\xi)^2\gamma\gamma'}{\lambda^2 DD'}\right\} \\ &\times\ \delta\left[\xi-1+\lambda\frac{D}{\gamma'}-\lambda\frac{D'}{\gamma}\right],\end{aligned} \tag{3.12}$$

where

$$D = 1-\vec{n}\cdot\vec{v}_e/c, \qquad D' = 1-\vec{n}'\cdot\vec{v}_e/c, \qquad \lambda = \left(1-\frac{v_e^2}{c^2}\right)^{-1/2}, \tag{3.13}$$

r_0 is the classical electron radius and δ is the Dirac delta function. Integration over the

relativistic maxwellian distribution

$$f_e(v_e) = \frac{\lambda^5 \exp(-\lambda/\tau)}{4\pi\tau c^3 K_2(1/\tau)} \tag{3.14}$$

gives the Compton Scattering Kernel (CSK)

$$\begin{aligned} \sigma(\gamma \to \gamma', \xi, \tau) &= \frac{3}{16\pi\gamma\nu} \int d\vec{v}_e \frac{f_e(v_e)}{\lambda} \left\{ 1 + \left[1 - \frac{1-\xi}{\lambda^2 D D'} \right]^2 \right. \\ &+ \left. \frac{(1-\xi)^2 \gamma\gamma'}{\lambda^2 D D'} \right\} \delta\left(\xi - 1 + \lambda\frac{D}{\gamma'} - \lambda\frac{D'}{\gamma} \right) . \end{aligned} \tag{3.15}$$

Here the CSK is normalized with respect to $\kappa_{es}\varrho$, which is reciprocal of the Thomson mean free path; the inverse probability, related to the scattering emissivity, can be obtained from the detailed balance condition

$$\sigma(\gamma \to \gamma', \xi, \tau)\, \gamma^2 \exp(-\gamma/\tau) = \sigma(\gamma' \to \gamma, \xi, \tau)\, \gamma'^2 \exp(-\gamma'/\tau) . \tag{3.16}$$

Further integrations over all outgoing photon directions and energies provide the source term appearing in the Boltzmann equation

$$\begin{aligned} \frac{g_C}{E} &= \kappa_{es}\varrho \int_0^\infty d\gamma' \int_{4\pi} d\Omega' \left(\frac{\gamma'}{\gamma} \right)^2 \sigma(\gamma' \to \gamma, \xi, \tau)\, f(r, \vec{n}', \gamma') \left[1 + \frac{f(r, \vec{n}, \gamma)}{2} \right] \\ &- \kappa_{es}\varrho \int_0^\infty d\gamma' \int_{4\pi} d\Omega' \sigma(\gamma \to \gamma', \xi, \tau)\, f(r, \vec{n}, \gamma) \left[1 + \frac{f(r, \vec{n}', \gamma')}{2} \right] . \end{aligned} \tag{3.17}$$

Inserting equation (3.16) into equation (3.17), the latter can be written in the more compact form

$$\begin{aligned} \frac{g_C}{E} &= \kappa_{es}\varrho \int_0^\infty d\gamma' \left[\exp\left(-\frac{\gamma - \gamma'}{\tau} \right) \left(\frac{f}{2} + 1 \right) - \frac{f}{2} \right] \int_{4\pi} d\Omega' \sigma(\gamma \to \gamma', \xi, \tau)\, f' \\ &- \kappa_{es}\varrho\sigma_{00} f , \end{aligned} \tag{3.18}$$

where $f' = f(r, \vec{n}', \gamma')$ and

$$\sigma_{00} = \int_0^\infty d\gamma' \int_{4\pi} d\Omega' \sigma\left(\gamma \rightarrow \gamma', \xi, \tau\right) \tag{3.19}$$

is the zero–th moment of the CSK (Shestakov, Kershaw & Prasad 1988). In the previous expressions, non–linear terms account for stimulated scattering.

The general task of computing the moments of the CSK was undertaken by Shestakov, Kershaw & Prasad (1988). They have shown that by performing the integration over γ' first and exploiting the δ–function, the expression of the zero–th moment, which is originally a fivefold integral, can be reduced, after a lot of non–trivial algebra, to a single quadrature

$$\sigma_{00} = \frac{1/\gamma}{2K_2\left(1/\tau\right)} \int_0^\infty dz \gamma z \sigma_0\left(\gamma z\right) \exp\left[-\frac{1}{2\tau}\left(z + \frac{1}{z}\right)\right] \tag{3.20}$$

where:

$$\begin{aligned} y\sigma_0\left(y\right) &= \frac{3}{8y}\left[\frac{y^2 - 2y - 2}{y} \ln\left(2y+1\right) + \frac{2y^3 + 18y^2 + 16y + 4}{\left(2y+1\right)^2}\right] \\ &= y\left(1 - 2y + \frac{26}{5}y^2 - \frac{133}{10}y^3 + \frac{1144}{35}y^4 - \cdots\right) \quad \text{for } |y| < \frac{1}{2}. \end{aligned} \tag{3.21}$$

The full evaluation of the Compton source term involves a number of very complicated six dimensional integrals of the distribution function weighted by the CSK for each value of γ, τ, μ. Because only discrete values of the distribution function will be available, all the six quadratures should be, in principle, evaluated numerically at each grid–point and this would make the integration of the transfer equation prohibitively time–consuming. However, as discuss by Kershaw, Prasad & Beason (1986), two of the three integrals in the CSK become analytical if a particular polar axis for projecting the electron velocity is chosen. Moreover, Kershaw (1987) presented an efficient method for calculating the single integral of the CSK

over γ' or ξ and the double integral over both these variables. A detailed discussion of our algorithm for the evaluation of the first addendum in the Compton source term, that is essentially a re–adaptation of Kershaw's method, is presented later on.

The treatment we have just described is the most general to handle Comptonization and proved to be reasonably fast. However, it still remains time–consuming when compared with other approximated treatments of Comptonization, that can provide a satisfactory description of the process in the non–relativistic or midly–relativistic regime. For this reason it is useful to have approximated expressions of g_C that can be used at lower temperatures.

As it is well known, the complicated nature of the CSK led many authors to model the Boltzmann equation by a diffusion equation in the frequency space. This approach, the Fokker–Planck approximation, was firstly used by Kompaneets (1956) in the limit of small γ and τ. Relativistic corrections to the Kompaneets equation can be included modifying the diffusion coefficient, and a number of efforts were devoted to extend its original form (Fraser 1966, as quoted in Pomraning 1973, Cooper 1971). More recently, Prasad *et al.* (1988) derived an exact analytical expression for the diffusion coefficient that holds for arbitrary values of γ and τ, in the assumption of a nearly isotropic radiation field. The main simplification introduced by the Fokker–Planck approximation is that the integral operator in the transfer equation is replaced by an infinite–order differential operator that, for small values of γ and τ, truncates at a finite order. The method, originally developed for the non–relativistic transfer equation, is based on an expansion of the specific intensity

in a Taylor series about $\nu' = \nu$. At first order in γ and τ, Fraser's result is

$$\begin{aligned} g_C E^2 &= -\kappa_{es}\varrho\,(1-2\gamma)\,I + \kappa_{es}\varrho \int_{4\pi} d\Omega' \sum_{n=0}^{3} \left(\frac{2n+1}{4\pi}\right) P_n\,(\xi)\, S_n I \\ &- \frac{3\kappa_{es}\varrho}{16\pi}\frac{c^2}{h\nu^3}\gamma I \left(1-\nu\frac{\partial}{\partial\nu}\right) \int_{4\pi} d\Omega' \left[1-\xi+\xi^2-\xi^3\right] I' , \end{aligned} \tag{3.22}$$

where P_n is the Legendre polynomial of order n and S_n $(n = 0,\ldots,3)$ are second order differential operators (see Pomraning 1973). Using the standard relation

$$\xi = \mu\mu' + \sqrt{1-\mu'^2}\sqrt{1-\mu^2}\cos\left(\Phi-\Phi'\right) , \tag{3.23}$$

the previous expression can be cast into the form

$$\begin{aligned} \frac{g_C}{E} &= \kappa_{es}\varrho\left[A_1 + \mu A_2 + \left(1-\mu^2\right)A_3 + \mu\left(3-5\mu^2\right)A_4\right] - \kappa_{es}\varrho f\,\{1-2\gamma \\ &+ \tau\left[A_5 - \mu^2 A_6 + \mu\left(3\mu^2-5\right)A_7 + \mu\left(3-5\mu^2\right)A_8\right]\} . \end{aligned} \tag{3.24}$$

The quantities A_i, containing the first four moments of f' and their first and second frequency derivatives, are reported in Appendix A. This is the expression of g_C needed in the general relativistic transfer equation in Fraser's approximation. We stress that up to now no assumptions have been made about the angular dependence in the energy exchange terms. A further simplification can be introduced if all terms, but f, in equation (26) are assumed to be isotropic and are replaced with their zero–th moments. The Compton source term becomes then

$$\begin{aligned} \frac{g_C}{E} &= \kappa_{es}\varrho j_\nu \left\{1-\gamma+\gamma\frac{\partial \ln J_\nu}{\partial \ln \nu} + \tau\left[\frac{\partial^2 \ln J_\nu}{\partial \ln \nu^2} + \left(\frac{\partial \ln J_\nu}{\partial \ln \nu}\right)^2\right.\right. \\ &- \left.\left. 3\frac{\partial \ln J_\nu}{\partial \ln \nu}\right]\right\} - \kappa_{es}\varrho f\left[1-2\gamma+\frac{1}{m_e\nu^2}J_\nu\left(1-\frac{\partial \ln J_\nu}{\partial \ln \nu}\right)\right] , \end{aligned} \tag{3.25}$$

where

$$J_\nu = \frac{1}{2}\int_{-1}^{1} I d\mu\,, \tag{3.26}$$

is the mean intensity. The approximated expressions (3.24) and (3.25) are to be preferred whenever a non–relativistic plasma is considered, since their evaluation is much faster than that of the general source term given by equation (3.18). Moreover, equation (3.25) contains far fewer terms than (3.24), and has the great advantage that all the angular dependence is contained in f.

The evaluation of the moments $\mathcal{S}_\nu^{A_k}$ is straightforward and follows in a natural way by averaging the previous expressions over angles. In particular, because Thomson scattering is elastic, the rate of change of the energy density must vanish, i.e. $\mathcal{S}_\nu = 0$. In this limit, it is

$$\begin{aligned} (\mathcal{S}_\nu)_{es} &= 0 \\ \left(\mathcal{S}_\nu^{ab}\right)_{es} &= -\frac{9}{10}\varrho\kappa_{es}\mathcal{M}_\nu^{ab} \\ \left(\mathcal{S}_\nu^{A_k}\right)_{es} &= -\varrho\kappa_{es}\mathcal{M}_\nu^{A_k} \qquad \text{for} \quad k \neq 0,2\,. \end{aligned} \tag{3.27}$$

These expressions can be easily understood on a physical ground: all moments except $k = 0, 2$ are destroyed by scattering interactions at the full Thomson rate $\varrho\kappa_{es}c$. On the other hand, the presence of a quadrupole contribution in the Thomson cross section translates in a different, reduced rate of disruption for the second moment of the radiation field, while the zeroth moment is not destroyed at all.

As previously stated, using the moments formalism, the only possible kind of description of Compton scattering is based on the Kompaneets approximation. The correspondent expression of $\mathcal{S}_\nu$ can be cast in a compact form as (see again Th81):

$$(\mathcal{S}_\nu)_C = \varrho\kappa_{es}\gamma\frac{\partial}{\partial\nu}\nu^4\left[\frac{kT}{h}\frac{\partial}{\partial\nu}\left(\frac{\mathcal{M}_\nu}{\nu^3}\right)+\left(\frac{\mathcal{M}_\nu}{\nu^3}\right)+\frac{c^2}{8\pi h}\left(\frac{\mathcal{M}_\nu^2}{\nu^6}\right)\right]. \tag{3.28}$$

To conclude, we note that all forms of the Compton source term based on the Fokker–Planck approximation contain both first and second frequency–derivatives of the moments of the distribution function. As noted by Nobili, Turolla & Zampieri (1993), in connection with the system of the first two PSTF moment equations, Compton terms act as singular perturbations, changing the mathematical character of the differential operator that becomes elliptic. As we discuss in detail later on, our numerical code is based on an iterative scheme in which integral terms, together with their derivatives, are treated as forcing terms, the only full–fledged differential operator being the one contained in the Boltzmann equation. On the other hand, the characteristic ray method provides the angular and frequency dependence for f that allows to write the Compton source term in its original form without resorting to the Fokker–Planck approximation. In this case the problem of radiative transfer with comptonization can be solved exactly in any range of energies and optical depths, and the hyperbolic character of the Boltzmann equation is naturally preserved.

4 The Numerical Method

In this chapter we describe in some detail the numerical scheme we have developed for solving the transfer problem using the characteristics method. The more general case, which corresponds to spherical flows in a Schwarzschild spacetime, is discussed in subsection (4.1); in subsection (4.2) a simplified version of the code, for the solution of the full radiation hydrodynamical problem in static, plane–parallel atmospheres is presented; finally subsection (4.3) is devoted to the numerical evaluation of the Compton source term.

4.1 The Spherical Case

As it is well known, in a scattering medium, the transfer equation is an integro–differential equation, while it has a simple structure when only true emission–absorption is included; in particular, it reduces to an ODE when written in its characteristic form. This suggests that its solution can be found using an iterative method in which the starting point is just the solution of the transfer problem with only free–free processes taken into account. Following this idea, equation (2.41) has been integrated numerically, with the boundary

conditions previously discussed, for a given set of values of the parameters b^2 and E_∞ and with the source term $g = g_{ff}$. This provides the zero–th order approximation, $f^{(0)}(r, \mu, E)$ of the distribution function, that can be used to evaluate the scattering integrals appearing in g_{es} or g_C. In the second step, we use the full expression for g to obtain the first order approximation $f^{(1)}(r, \mu, E)$. This is the solution of the transfer equation written in the form

$$\frac{y(\mu + v)}{r_g}\frac{df^{(1)}}{dr} = \frac{g_{ff}}{E} + \alpha[f^{(0)}] - \beta[f^{(0)}]f^{(1)}\,. \tag{4.1}$$

All the expressions of the scattering source term discussed in the previous section can be cast, and have been presented, in this form. In equations (3.8), (3.10), (3.24) and (3.25) β can be immediately identified with the coefficient of f; in equation (3.18) α is the integral term. The scheme is iterated until convergence is reached, improving at each iteration the functionals α and β making use of the distribution function computed in the previous step. As a convergence test, we compared each element of the matrix j_ν with its value relative to the previous iteration and stored the maximum relative correction. Cauchy criterion has been applied to verify the convergence of the succession of such corrections.

Equation (2.41) has been integrated using a a finite differences method originally developed by Nobili & Turolla (1988), in which the algebraic system is iteratively solved using the Henyey technique for matrix manipulation. The entire radial domain $[r_{in}, r_{end}]$ is divided by M points; rays of type a) are integrated using this grid. For trajectories which exhibit a turning point, the transfer equation is solved on the same mesh, picking up the subset of grid points which cover their region of existence. Although, as we already mentioned, the choice of r as the parameter along the geodesics has a number of advantages, it results in a

divergent derivative of f at $\mu = -v$. While, for those branches which approach the turning point, this introduces some errors at most in the last few points, trajectories moving away from the turning points may be systematically affected by an inaccurate determination of their boundary condition. However, it should be taken into account that when the optical depth at the turning point is either large or very small, f tends to B_ν/hcE^3 or remains vanishingly small, independently on the boundary condition for equation (2.41). Numerical errors, if any, are, then, restricted to rays inverting in regions of moderate optical depth.

The choice of the b–grid strongly constraints the final angular resolution of f, and requires special care. Let us first assume that a black hole is the central source; in this case the interval $0 \leq b^2 < 27/4$ corresponds to ingoing and outgoing trajectories of class a). For these two subclasses, we fix N_1 and N_2 values of the impact parameter in such a way to produce an equally–spaced μ–grid, in the range $[-1, 1]$, at the critical point $r = 3/2$. To discretize the range $b^2 \geq 27/4$, we exploit the one–to–one correspondence between b^2 and the position of the turning points, $r = r_n$,

$$b_n^2 = \frac{r_n^3}{r_n - 1}. \tag{4.2}$$

We fix N_3 and N_4 values of r_n, the first at $r \leq 3/2$ and the latter at $r \geq 3/2$; the r_n's are just the radii of the spherical shells tangent to the orbits of types b) and c). In such a way, the total number N of μ–points in the interval $-1 \leq \mu \leq 1$ is r–dependent, and it is bounded by $N_1+N_2+1 \leq N \leq N_1+N_2+2N_3-1$ for $r \leq 3/2$ and $N_1+N_2+1 \leq N \leq N_1+N_2+2N_4-1$ for $r \geq 3/2$. A better angular resolution in all the radial domain can be obtained increasing the number of photon trajectories. In the case the central source is a star of radius r_*, the

μ–gridding works in a very similar way, but the values of b in the range

$$0 \leq b^2 < \frac{r_*^3}{r_* - 1} \tag{4.3}$$

now produce an equally–spaced μ–mesh at the star radius, the N_4 points refers to $r > r_*$ while no trajectory of type b) is present. We have found more convenient to derive the values of the impact parameter starting from the radial coordinate of the turning points, and not vice versa, since in this way the radial extent of the photon trajectories, and hence the integration range of equation (2.41), is specified without solving the cubic equation (4.2).

Once the rays are fixed, equation (2.41) must be integrated for different values of the parameter E_∞ along each trajectory. The range of E_∞ should be chosen in such a way that, at each value of r, we can compute the distribution function in an interval of the local energy, $[E_{min}, E_{max}]$, large enough to cover the interesting portion of the spectrum. The parameter range $[(E_\infty)_{min}, (E_\infty)_{max}]$ must be larger than $[E_{min}, E_{max}]$ at any given radius, since both gravity and dynamics act in changing the photon energy along the geodesics. For $r < r_{end}$, in fact, the energy interval $[E_{min}, E_{max}]$ is actually influenced by some characteristic rays starting at r_{end} with E_∞ in the range

$$(E_\infty)_{min} = [y\,(1+v)]_{r_{min}}\, E_{min} \leq E_\infty \leq [y\,(1-v)]_{r_{min}}\, E_{max} = (E_\infty)_{max}\,. \tag{4.4}$$

In the numerical calculations we have used the dimensionless energy $x = E/KT_*$, where T_* is a suitable normalization temperature. For later applications, we found more convenient to divide the storage window $[x_{min}, x_{max}]$ by means of L points equally–spaced in $\ln x$; the

same grid is maintained at all radii and f is stored at these points as a function of the local dimensionless energy using an interpolation. In the two remaining ranges $[(x_\infty)_{min}, x_{min}]$ and $[x_{max}, (x_\infty)_{max}]$, $2P$ values of x_∞ has been specified. For these values of the energy at infinity, the transfer equation has been integrated only along the trajectories of those photons that, at some r, have a local energy within our storage window. Loading the matrix $f(r_i, \mu_j, E_k)$ is particularly convenient since it allows a more direct calculation of the scattering integrals, that are evaluated at both constant r and E. All angular integrals can be obtained simply performing a weighted sum of f over the μ–index without any additional scanning of the array or extra interpolations. This has, also, the advantage that the we are free to choose the most suitable numerical scheme to integrate over energies since the rearrangement of the energy points at each radius follows automatically. The numerical evaluation of the frequency–dependent moments of f has, however, to be carried out with some care. In particular, when the optical depth drops below unity and radial streaming is approached, the integration over μ becomes troublesome and we found more convenient to perform the quadrature over b^2, using equation (11a). Since the same change of variable works well near the horizon, where outgoing rays concentrate towards $\mu = 1$, it has been used in all the radial range. However, because of the divergence of $d\mu/db^2$ where $\mu = -v$, in a small region around this point the original μ–integration was performed at each value of r.

4.2 The Static, Plane–parallel Case

The numerical scheme we have just presented allows the solution of the transfer equation along the geodesic rays in the more general case, when gravity, dynamics and sphericity are all accounted for. In many astrophysical applications, however, transfer of radiation through a static, geometrically–thin atmosphere is of interest, like, for example, when studying reprocessing of thermal radiation in the atmosphere of X–ray bursting neutron stars. In all these cases, a plane–parallel approach to the solution of the transfer problem is fully justified since the atmospheric scale height is much less than the star radius, although the effects of the strong gravitational field must still be considered. The assumption of hydrostatic equilibrium introduces a major simplification in the treatment of radiative transfer because advection and aberration are no more present. For a vanishing velocity field, equation (2.36) reduces to $E = E_\infty/\sqrt{-g_{00}}$, implying that the value of the local energy at a given radius is the same along all rays. This is just another way of stating the existence of Thorne's (1981) Universal Red–shift Function. The rays are now symmetrical with respect to the $\mu = 0$ line. A further, drastic, simplification follows if it can be assumed that the radial coordinate is constant in the atmosphere and equal to the star radius. This is commonly done in non–relativistic transfer theory, replacing the height above the base of the atmosphere with the optical depth. The rays are just straight lines, $\mu = const$, while the photon energy seen at infinity is simply the energy at any depth red–shifted by the constant factor $(1-1/r_*)^{1/2}$. In the light of these considerations, we have developed and tested a reduced version of our code which uses the scattering depth as the independent variable. The angular mesh is obtained

specifying directly the values of μ; the energy points at which f is computed coincide with the energy grid, which is the same at all depths. The calculation proceeds exactly in the same way as in a non–relativistic problem and the spectrum at infinity is simply obtained by applying the gravitational red–shift factor to the spectrum emerging at the top of the atmosphere.

Applications to isolated neutron stars accreting at low rates are presented in Chapters 7 and 8. In this problem electrons are far from being relativistic so Comptonization can be safely treated in the diffusion approximation using expression (3.25) for the scattering source term. The much shorter computational time allowed us to solve also the thermal and pressure structure of the atmosphere, coupling the hydrostatic balance and the radiative energy equilibrium to the transfer equation. The hydro equations are solved iteratively, exploiting the scheme for the computation of the scattering integral we have already discussed. Pressure and temperature profiles are computed at each iteration step, once the frequency–integrated moments have been obtained.

4.3 Numerical Evaluation of the Compton Source Term

As discussed in Chapter 3, the Compton source term, in the form (3.18), is the sum of two contributions. The second addendum, which requires the calculation of the zero–th moment of the CSK, σ_{00}, poses no problem since it involves a single quadrature of an analytical function. As proposed by Shestakov, Kershaw & Prasad (1988), upon the change

of variable

$$u = \frac{1}{\sqrt{2\tau}}\left(\sqrt{z} - \frac{1}{\sqrt{z}}\right), \tag{4.5}$$

σ_{00} can be efficiently evaluated using a Gauss–Hermite quadrature. We have tested that six points give an accuracy better than 3 parts in 1000, sufficient for our purposes.

We are left, then, with the problem of finding a fast algorithm for the numerical calculation of the multiple integral

$$\int_0^\infty d\gamma' \left[\exp\left(-\frac{\gamma-\gamma'}{\tau}\right)\left(\frac{f}{2}+1\right) - \frac{f}{2}\right] \int_{4\pi} d\Omega' \sigma\left(\gamma \to \gamma', \xi, \tau\right) f' . \tag{4.6}$$

First of all, we note that the scattering probability may become strongly peaked; in the Thomson limit, for example, the CSK tends toward a δ–function at $\gamma = \gamma'$. In all regimes in which the integrand is fast–varying particular care must be used to account for delicate cancellations between opposite terms. We start considering the CSK itself. As discussed by Kershaw, Prasad and Beason (1986), the complicated three–dimensional integral in the electron velocity space can be reduced to a single integral when the solid angle element is defined with respect to a particular polar axis. In fact, taking the polar axis in the direction of the photon momentum transfer $\vec{s} = (\gamma'\vec{n}' - \gamma\vec{n})/q$, $q = \sqrt{\gamma^2 + \gamma'^2 - 2\gamma\gamma'\xi}$, and using the Dirac δ–function to integrate over the polar angle, the integration over the azimuthal angle becomes analytical. The final form of the CSK is then

$$\begin{aligned} \sigma(\gamma \to \gamma', \xi, \tau) &= \frac{3}{32\gamma\nu\tau K_2(1/\tau)} \exp\left(-\lambda_+/\tau\right)\left\{\frac{2\gamma\gamma'\tau}{q}\right. \\ &+ \left.\int_{\lambda_+}^\infty \exp\left(-\frac{\lambda-\lambda_+}{\tau}\right)\left\{\frac{1}{(1-\xi)^2}\right.\right. \end{aligned} \tag{4.7}$$

$$\times \left[\frac{(\lambda+\gamma)(1/\gamma+1/\gamma')-(1+\xi)}{\left[(\lambda+\gamma)^2+\omega^2\right]^{3/2}} + \frac{(\lambda-\gamma')(1/\gamma+1/\gamma')+(1+\xi)}{\left[(\lambda-\gamma')^2+\omega^2\right]^{3/2}} \right]$$
$$+ \left[-\gamma\gamma' + \frac{2}{1-\xi} + \frac{2}{\gamma\gamma'(1-\xi)^2} \right]$$
$$\times \left[\left[(\lambda+\gamma)^2+\omega^2\right]^{-1/2} - \left[(\lambda-\gamma')^2+\omega^2\right]^{-1/2} \right] \Big\} d\lambda \Big\}$$

where the Lorentz factor λ is now the integration variable, $\omega^2 = (1+\xi)/(1-\xi)$ and

$$\lambda_+ = \frac{\gamma'-\gamma}{2} + \left\{ \left[1+\gamma\gamma'\frac{1-\xi}{2} \right] \left[1+\frac{(\gamma-\gamma')^2}{2\gamma\gamma'(1-\xi)} \right] \right\}^{1/2} . \tag{4.8}$$

As stressed by Kershaw *et al.* , the main features of the scattering probability are contained in the $\exp(-\lambda_+/\tau)/q$ term: everything is smoothly varying with respect to this quantity, in particular with respect to the exponential. Kershaw *et al.* proposed two methods for the numerical evaluation of the λ–integral in equation (4.7); in both cases the CSK is reduced to an approximate analytical expression. Here we adopt their fastest, although less accurate, algorithm which is based on a suitable division of the integration domain into subintervals where the exponential is replaced by a linear interpolation. To avoid delicate cancellations when $\tau \to 0$, a Taylor expansion of the inner expression in curly brackets is used to obtain an asymptotic series in terms of Legendre polynomials for the integral; only terms up to second order are retained. Using this method the evaluation of the CSK becomes analytical with an accuracy of about 3 parts in a thousand in all parameter ranges. The CPU time for a single evaluation is typically few microseconds on an alpha DEC–3000.

The algorithm we adopt for computing integrals involving the CSK follows the original method presented by Kershaw (1987) for evaluating the total scattering cross–section and

it is based on the fact that λ_+ has a minimum in both γ' and ξ. The most important contribution to the CSK comes, in fact, from regions near this minimum; everywhere else the scattering probability goes to zero exponentially fast with an e–folding length that is simply τ in λ_+. Having these considerations in mind, the double angular integral in expression (4.6) can be written, taking ξ and $\overline{\phi}$ as the polar and azimuthal angles, as

$$\int_{4\pi} d\Omega' \sigma\left(\gamma \rightarrow \gamma', \xi, \tau\right) f' = \int_{-1}^{1} d\xi \sigma\left(\gamma - \gamma', \xi, \tau\right) \int_{0}^{2\pi} d\overline{\phi} f\left(r, \mu', \gamma'\right) . \tag{4.9}$$

For each value of r, μ, γ', ξ the azimuthal integral is evaluated using a Lobatto quadrature. The values of the distribution function at

$$\mu_l' = \mu\xi + \sqrt{1-\mu^2}\sqrt{1-\xi^2}\cos\overline{\phi}_l \tag{4.10}$$

where $\overline{\phi}_l$ are the Lobatto abscissae, are obtained from a linear interpolation. Once this is done, for each value of γ, γ', τ, the integration over all polar directions is carried out picking up the ξ range, within the interval $|\xi| \leq 1$, that provides a non–negligible contribution to the scattering probability: as we anticipated, this is the region around the minimum of λ_+. For fixed γ, γ' and τ, the e–folding lengths in λ_+, $n\tau$, immediately provide the e–folding lengths in ξ, ξ_n. Denoting, in fact, with $\xi_m = 1 - |\gamma - \gamma'|/(\gamma\gamma')$ the value of ξ where λ_+ is minimum, ξ_n is the root of the equation

$$\lambda_{+m1} + n\tau = \lambda_+\left(\gamma, \gamma', \xi_n\right) , \tag{4.11}$$

where $\lambda_{+m1} = \lambda_+\left(\gamma, \gamma', \xi_M\right)$ and

$$\xi_M = \max\left(\min\left(\xi_m, -1\right), 1\right) . \tag{4.12}$$

Within each e–folding interval we use a 4–points Lobatto quadrature and the number of intervals is fixed by the request that either the fractional contribution of the last e–folding is less than the desired accuracy (5×10^{-3} in the present case) or the boundary $\xi = \pm 1$ is reached. At $\gamma = \gamma'$ and $\xi = 1$ the CSK has an integrable ($\sim \sqrt{1-\xi}$) singularity, that can be easily eliminated with the change of variable $\eta = \sqrt{1-\xi}$.

The integration in energy is carried out in a similar way. Since the most important contribution to the inner integral (over ξ in our scheme) comes from regions where λ_+ is near λ_{+m1}, the larger contribution to the outer integral (over γ') is provided by regions where λ_{+m1} itself is minimum. Clearly, the lowest values of λ_{+m1} correspond to $\xi_M = \xi_m$, i.e. to $\xi_m \geq -1$; the inequality $\xi_m \leq 1$ is always satisfied. We distinguish two cases: for $\gamma' \leq \gamma$ the previous condition is verified in the interval

$$\frac{\gamma}{1+2\gamma} \leq \gamma' \leq \gamma \tag{4.13}$$

that we call region A, while for $\gamma' \geq \gamma$ it holds in two different domains, that we call in general region B, depending on the value of γ:

$$\begin{aligned} \gamma \leq \gamma' \leq \frac{\gamma}{1-2\gamma} \quad &\text{if} \quad \gamma < 1/2 \\ \gamma \leq \gamma' < \infty \quad &\text{if} \quad \gamma \geq 1/2\,. \end{aligned} \tag{4.14}$$

Since in region A $\lambda_{+m1} = 1$, the search for the e–folding lengths is not required and integration is straightforward. This is not the case in region B, where $\lambda_{+m1} = 1+\gamma'-\gamma$. Now, although its minimum value is still $\lambda_{+m2} = 1$, λ_{+m1} is *not* a constant. The corresponding

e–folding lengths γ'_n are to be derived solving the equation

$$\lambda_{+m2} + n\tau = \lambda_+ (\gamma, \gamma'_n, \xi_M) \ , \tag{4.15}$$

which reduces to

$$1 + n\tau = 1 + \gamma'_n - \gamma \tag{4.16}$$

and gives simply $\gamma'_n = \gamma + n\tau$. In region B integration over γ' is carried out using the same procedure introduced for the ξ–quadrature. To complete our discussion, we need to consider the two intervals

$$0 \leq \gamma' < \frac{\gamma}{1+2\gamma} \ , \tag{4.17}$$

region C, and, if $\gamma < 1/2$,

$$\frac{\gamma}{1-2\gamma} \leq \gamma' < \infty \ , \tag{4.18}$$

region D. In both cases $\lambda_{+m1} = \lambda_+ (\gamma, \gamma', -1)$ and its minimum is reached at

$$\lambda_{+m2} = \lambda_{+m1}|_{\gamma'=\gamma/(1+2\gamma)} \tag{4.19}$$

or

$$\lambda_{+m2} = \lambda_{+m1}|_{\gamma'=\gamma/(1-2\gamma)} \tag{4.20}$$

in regions C and D respectively. The corresponding e–folding lengths are obtained from equation (4.15). Lobatto rule is used everywhere and stepping is terminated when its fractional contribution becomes less than 5×10^{-3}. The most convenient number of Lobatto points depends on the typical relative values of the photon energy and gas temperature. In fact, for different values of γ and τ, $\lambda_+(\gamma')$ can be either strongly peaked or very broad

near its minimum. Optimization requires some numerical experimenting, looking for the best agreement between the direct evaluation of the CSK double integral and σ_{00} computed using equations (3.20). For the test model presented in Chapter 5, we used either a six or a ten points quadrature. Accordance between the values of σ_{00} obtained using the two methods is better than 3–4%, with the larger errors in the external region where the radiation temperature (mean photon energy) is very far away from the gas temperature. On the other hand, where the Compton parameter Y_C (see e.g. Rybicki & Lightman 1979) is greater than unity, accuracy is better than 7 parts in a thousand. We finally note that the choice of a gaussian–type quadrature is motivated, basically, by the fact that we need to perform integrals of the CSK times f. The distribution function must be interpolated to obtain its values at the integration points. Clearly, gaussian–type quadratures with a fixed number of abscissae are much faster, although less accurate, than step–adaptive schemes, as the Simpson rule originally used by Kershaw. Computational feasibility is also the reason for which we decided to evaluate the integral (4.6) using the values of f relative to the previous iteration. Clearly, it is possible to rewrite expression (4.6) as

$$\begin{aligned} & \frac{f}{2} \int_0^\infty d\gamma' \left[\exp\left(-\frac{\gamma-\gamma'}{2}\right) - 1\right] \int_{4\pi} d\Omega' \sigma\left(\gamma \rightarrow \gamma', \xi, \tau\right) f' \\ & + \int_0^\infty d\gamma' \exp\left(-\frac{\gamma-\gamma'}{2}\right) \int_{4\pi} d\Omega' \sigma\left(\gamma \rightarrow \gamma', \xi, \tau\right) f' \end{aligned} \tag{4.21}$$

since f does not depend on γ'. Now f is just the dependent variable of the transfer equation at any iterative step. The drawback is that the computing times is about doubled, because of the two multiple integrals. The CPU time for a single evaluation of expression (4.6) is typically ~ 0.1 s and, in an production run, a $\sim 2 \times 10^5$ evaluation are required, implying

a total time of about 6 hr.

5 Spherical Accretion onto Black Holes

In this chapter we shall deal with the problem of computing the spectral properties of radiation produced in stationary, spherical accretion onto black holes. Although, under these assumptions, this is an highly idealized problem, at the same time it represents an ideal proving ground to allow for more and more complex description of the radiative processes, just because of the simplifications introduced by the presence of symmetries. Despite the fact that applications have a limited validity, in some astrophysical situations the assumption of spherical symmetry seems to be not unreasonable. As an example, the inner part of advective dominated disks seems to be well described by a spherical model (....). Observations of BH candidates in the high state also provide several clues about the validity of this approximation to model the inner region of the flow. In fact, the spectrum of these sources shows the clear presence of a power–law, high energy tail that is well explained in terms of dynamical comptonization in a free–falling gas (..).

The emission properties of the accreting material have been investigated by several authors, in the attempt to provide a self–consistent description of the phenomenon and

to obtain an evaluation of the net energy output emitted as electromagnetic radiation. At variance with what happens for stationary accretion onto neutron stars, where the requirement that all the kinetic energy is converted into radiation at the surface of the stars fixes the efficiency, in the case of a black hole matter can cross the horizon carrying a considerable fraction of its gravitational binding energy. The efficiency of the process is not fixed a priori, and depends on the relative effectiveness of the radiative processes against the strong velocity field.

After the first qualitative analysis by Shvartsman (1971), optically thin models were presented by Shapiro (1973a, b) and Mèszàros (1975). These solutions are characterized by low accretion rates ($\dot{m} < 1$) and high temperatures. Due to the typical low densities, cooling processes are inefficient in converting gravitational energy into radiation and the emitted luminosity turns out to be very low. However, when the accretion rate increases, the inner region starts to develop an optically thick core. The transition between optically thin and optically thick models has been considered in some details by Soffel (1982), while solutions in diffusion regime were provided by a number of authors (see e.g. Tamazawa *et al.* 1974, Maraschi, Reina & Treves 1974, Kafka & Mèszàros 1976, Vitello 1978, Begelman 1979, Gillman & Stellingwerf 1980, Freihoffer 1981, Flammang 1982, 1984) and the hypercritical regime at high $\dot{m}$ has been investigated by Blondin (1986). Actually, thin (à la Shapiro) and thick (à la Blondin) solutions represent the tails of the same, continuous branch in the plane $(\log \ell, \log \dot{m})$ (here ℓ is the luminosity in Eddington units, $L_{Edd} = 4\pi GMc/\kappa_{es}$ for a black hole of mass M). Although the luminosity output in optically thick models is higher

with respect to the optically thin ones, the total flux always remains quite low and the efficiency of the process is not considerably increased by increasing $\dot{m}$. From a qualitative point of view, the physical reason can be easily understood: as the accretion rate increases, the formation of an inner, thick core where LTE is reached initially causes an increase in both temperature and luminosity. However, this behaviour is partially countered by the fact that at the same time the inner region becomes also optically thick with respect to electron scattering. The consequent appearance of a trapping radius (Rees 1978, Begelman 1978), below which a substantial fraction of radiative energy is advected into the hole, slows the rate of increase of the efficiency with $\dot{m}$.

On the other hand, all these investigations neglected the role of Comptonization in the accreting flow. As first pointed out by Wandel, Yahil & Milgrom (1984) and then confirmed with a more detailed analysis by Park (1990a.b), allowing for this process reveals a distinctive feature of black hole accretion, i.e. the appearance of a bimodal behaviour at high accretion rates ($3 \lesssim \dot{m} \lesssim 100$). At high enough values of $\dot{m}$ two disconnected branches of solutions coexist for the same $\dot{m}$; the new branch, dominated by effects of Comptonization, is characterized by higher temperatures and luminosities.

The issue of a simultaneous determination of the two branches as solutions of a unique, self-consistent model was addressed by Nobili, Turolla and Zampieri (1991, here NTZ91 as already indicated). Detailed models were computed in a range of $\dot{m}$ spanning more than four decades, confirming the previous analysis and performing a systematic investigation of the role of preheating in bounding the region of existence of the "high" states. The resulting

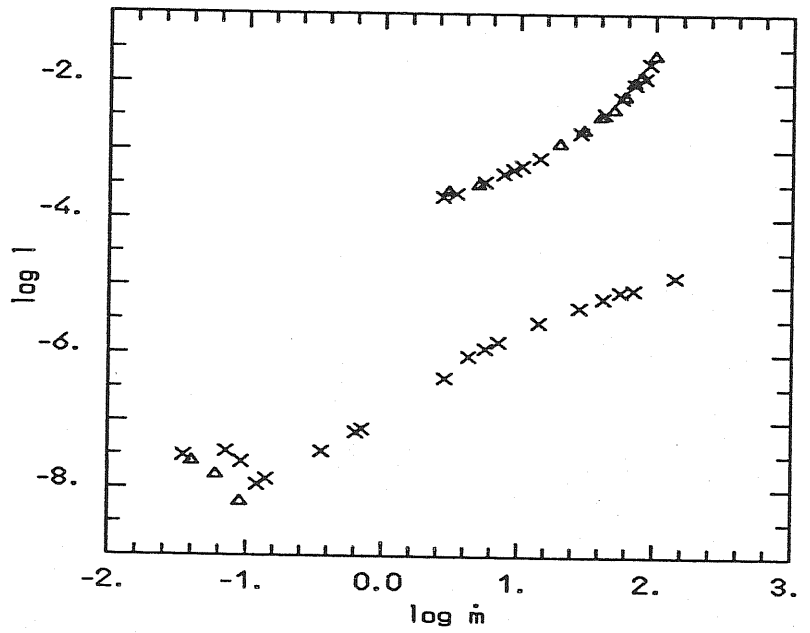

Figure 5.1: *The* $(\log \ell, \log \dot{m})$ *diagram for the NTZ91 solutions (crosses); some of Park's (1990a) models (open triangles are also shown for comparison. Taken from NTZ91.*

$(\log \ell, \log \dot{m})$ diagram is reported in figure 5.1.

NTZ91 solutions were obtained by solving the first two frequency–integrated PSTF moments equations (see chapter 2) coupled with the Euler, energy conservation and continuity equations (see again NTZ91):

$$(P+\varrho)\frac{y'}{y} + P' + \frac{r r_g s^1}{y} = 0\,, \tag{5.1}$$

$$\varrho' - (P+\varrho)\frac{\varrho_0'}{\varrho_0} + \frac{r r_g s^0}{yv}\,, \tag{5.2}$$

$$\frac{(vy)'}{vy} + \frac{\varrho_0'}{\varrho_0} + 2 = 0\,. \tag{5.3}$$

Here P, ϱ_0, ϱ are the gas pressure, rest mass and energy densities respectively, s^0 and s^1 are the frequency–integrated, PSTF scalar moments of the source term, while a prime denotes

differentiation with respect to $\ln r$ and, as usual, r is the radial coordinate in units of r_g. A pure hydrogen plasma was considered; the equation of state and the expression of ϱ incorporate effects of ionization and contributions from relativistic electrons, while the source term includes $e-p$, $e-e$ bremsstrahlung, free-bound and bound–bound transitions together with Compton scattering in Kompaneets approximation. The correspondent expressions of the two source moments s^0 and s^1 are

$$s^0 \equiv \int_0^\infty s^0_\nu d\nu = \frac{\varrho_0^2 \Lambda}{m_p^2 c}\left(1 - \frac{w^0}{aT^4}\right) + \kappa_{es}\varrho_0 w^0 \frac{4k}{m_e c^2}(T - T_\gamma)\,, \tag{5.4}$$

$$s^1 \equiv \int_0^\infty s^1_\nu d\nu = -\varrho_0 k_1 w^1\,, \tag{5.5}$$

where k_1 includes both the Rosseland mean opacity and the scattering contribution, Λ is the cooling function, w^0 and w^1 denote the first two frequency integrated PSTF moments and T_γ is the radiation temperature

$$T_\gamma = \frac{1}{4k}\frac{\int_0^\infty h\nu w^0_\nu d\nu}{\int_0^\infty w^0_\nu d\nu}\,. \tag{5.6}$$

An important approximation must be introduced in the problem just because of the dependence of s^0 on T_γ in presence of Compton scattering. In fact, this quantity can not be self–consistently calculated in a frequency–integrated analysis, and it was estimated by NTZ91 as solution of an additional phenomenological equation, originally proposed by Park & Ostriker (1989) and Park (1990a)

$$\frac{T'_\gamma}{T_\gamma} = 4\frac{kT}{m_e c^2}\max\left(\tau_{es}, \tau_{es}^2\right)\frac{T - T_\gamma}{T}\,. \tag{5.7}$$

As a first application of our characteristic code, we present in this chapter the numerical solutions of the transfer problem for the two different accretion regimes. In these calculations

we only focus on the solution of the transfer problem, while the flow hydrodynamics is kept fixed, using the numerical results derived by NTZ91. Since our present goal is to test the capabilities of our method, no attempt has been made to explore the model parameter space: we just present results for a single model which we judge useful in illustrating the main features of our integration scheme.

No previous solutions for black hole accretion spectra are available, at least for models which contain an optically thick core. Our attempt to cross-check results presented in section 5.1 integrating the moment equations were hindered by severe numerical problems which arise when the flow is not effectively thick at the horizon at all frequencies. The moment method can not, also, be used to compute radiative transfer in "hot" models, where Compton scattering must be treated outside the Fokker–Planck approximation.

In both examples radiative effects due to magnetic fields and pair production–annihilation are not accounted for. This is not a too crucial approximation as far as low–luminosity solutions are concerned. In fact, referring to the model in section 5.1, it can be easily shown that, for typical temperatures and densities in the photospheric region, the cyclotron emission is lower than the free-free emission if $B \lesssim 10^7$ G (see e.g. Schmid–Burgk, 1978). This limiting value exceeds the maximum strength of the tangled B–field derived assuming equipartition between magnetic and thermal energy densities. However, in the inner regions of high–luminosity models electrons become relativistic and both pair processes and synchrotron emission could play a role.

5.1 Accretion onto Black Holes: Low–luminosity Solutions

In this section we focus on the "low" luminosity case, and we consider a model with high accretion rate, $\dot{m} \gtrsim 1$ in Eddington units. As previously discussed, in this regime low–luminosity solutions start to develop an inner region optically thick to both free–free and scattering and show negligible Comptonization; consequently, electron scattering can be treated in the Thomson limit, using the simple expression (3.10). On the other hand, the accreting matter reaches $r \sim 1$ with $v \sim 1$, so that a detailed analysis of these models provide a powerful tool to shed light on the effects of dynamical comptonization, that turns out to be the more important process in shaping the high energy tail of the spectral distribution.

This particular model corresponds to the NTZ91 solution characterized by $\dot{m} = 0.71$, and by a value of the density at the horizon $\varrho_H = 10^{-6}\,\mathrm{g\,cm^{-3}}$. As in NTZ91, here and in the following section we consider a black hole mass of $M = 3M_\odot$, $M_\odot$ is the solar mass. The run of some hydrodynamicals variables, as derived by NTZ91, is reported in figure 5.2 (note the difference of notation between this thesis and NTZ91; in figure 5.2 and 5.6: $\tau \equiv \tau_{es}$).

As can be seen from figure 5.2, the location of the sonic point is very far away with respect to the photosphere (where the effective optical depth τ_{eff} is close unity), so that we can safely assume that matter is free–falling with $u^1 = r^{-1/2}$ in our region of interest. This fact is quite general, and turns out to be true also for the model presented in next section. The gas temperature is in the range $2 \times 10^4\ \mathrm{K} \lesssim T \lesssim 5 \times 10^5\ \mathrm{K}$, so we have chosen a normalization temperature $\ln T_* = 11$. The dimensionless energy window is $x_{\min} = 0.1 < x < x_{max} = 40$, corresponding to the range 0.5–206 eV; here $L = 30$ points have been used (see section 4.1).

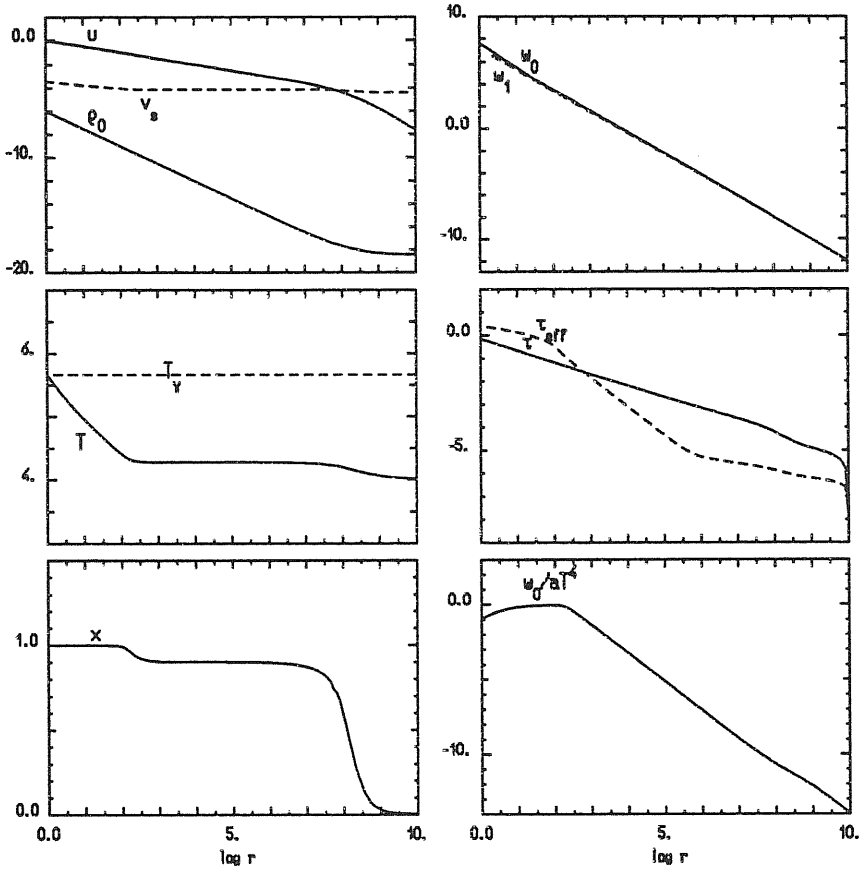

Figure 5.2: *From top left to bottom right the run of: 4-velocity* $u = yv$*, sound speed* v_s *and matter density* ϱ_0*; radiation energy density* w_0 *and radiation flux* w_1*, both in* $\mathrm{erg\,cm^{-3}}$*; gas and radiation temperatures,* T *and* T_γ*; electron scattering and effective optical depths,* τ *and* τ_{eff}*; ionization degree* x*;* w_0/aT^4 *ratio. Here* $(\varrho_0)_H = 1 \times 10^{-6}\ \mathrm{g\,cm^{-3}}$*,* $\dot{m} = 0.71$*. Taken from NTZ91.*

Outside this range, $P = 10$ energies has been fixed in each of the two additional intervals of x_∞ we need, as discussed in section 4.1. Since the effective optical depth at our larger energies is everywhere < 1, we solved the transfer problem for $10^{-2} \leq \log r \leq 5$, imposing the boundary condition $df/dr = 0$ along trajectories starting at r_{in}. The radial domain has been divided by $M = 250$ points; the grid is not uniformly spaced and points are tighter around $r = 3/2$. To obtain a good angular resolution, 90 trajectories have been followed at each energy, $N_1 = N_2 = 20$, $N_3 = 10$, $N_4 = 40$. In such a way, the number of μ points, which is minimum at $r = 3/2$, is always greater than 21. At each value of x within the storage window the scattering source term was calculated using a linear interpolation for both the matrices j_ν and k_ν; outside this window an extrapolation has been used.

Figures 5.3 and 5.4 show the mean intensity J_ν and radiation pressure K_ν at different energies, together with the Planck function at $T(r_{in})$; each curve corresponds to a different value of the radial coordinate. The effective frequency–dependent optical depth goes from 3×10^3 to 10^{-4} for the lowest frequency, while high energy photons stream freely at all radii. The low energy portion of the spectral distribution is a superposition of thermal bremsstrahlung emission at different temperatures while bulk motion Comptonization produces a power law high–energy tail. In this model the inner region is only marginally thick with respect to electron scattering, being the scattering optical depth ~ 0.7 at the horizon. As a consequence, dynamical comptonization is not very efficient in boosting soft photons toward high energies; its effects is not saturated (but is yet visible in the power–law distribution) and the calculated spectral index turns out to be $\alpha = -2.9$.

On the other hand, although results are not reported here, we also computed the emitted spectrum of "cold" solutions correspondent to different values of $\dot{m}$, increasing the value of the optical depth in the inner region. This systematic analysis revealed some unexpected effects of bulk motion comptonization. In fact, we always found that this process tends to create a power–law, high energy tail, but the value of the spectral index depends on the optical depth at the horizon. This is in contrast with the analytical results derived by Payne & Blandford (1981), who found that, in the limit $\tau_{es} \gg 1$, the spectral index only depends on the velocity gradient and is $\alpha = -2$ for a free–fall velocity profile. These results led to reconsider the problem even from an analytical point of view, extending the classical analysis by Payne & Blandford to the relativistic case. We found that, when these corrections are taken into account, the numerical results are in perfect agreement with the theoretical one (see chapter 6).

At large radii, where radial streaming is approached, all moments fall off as r^{-2}: the asymptotic radial gradient we have found is -1.99. While the evaluation of even moments does not pose particular problems, in the inner regions, where the radiation field is nearly isotropic, a direct numerical quadrature for computing odd moments becomes troublesome because of the delicate cancellations between contributions of opposite sign. To avoid this problem, the monochromatic flux, presented in figure 5.5, has been replaced with its analytical expression in the diffusion approximation every time it is $\tau_{eff} > 10$. A typical production run required 10–11 iterations to converge with a fractional accuracy better than 10^{-4}, with a total CPU time of about 20 minutes on an alpha DEC–3000.

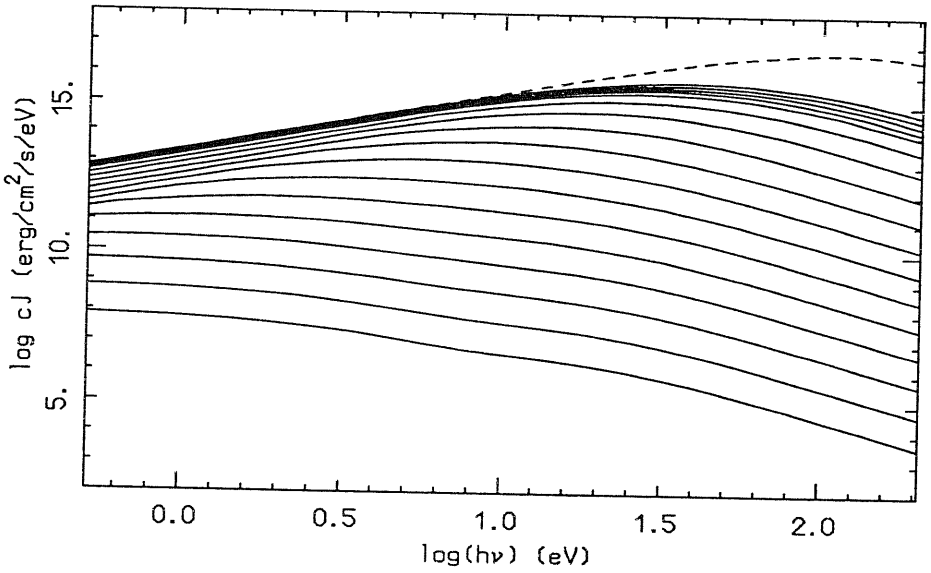

Figure 5.3: *Monochromatic mean intensity at different radii (full lines), together with the blackbody function at $T(r_{in})$ (dashed line), for "cold" accretion onto a black hole with $\dot{m} = 0.71$.*

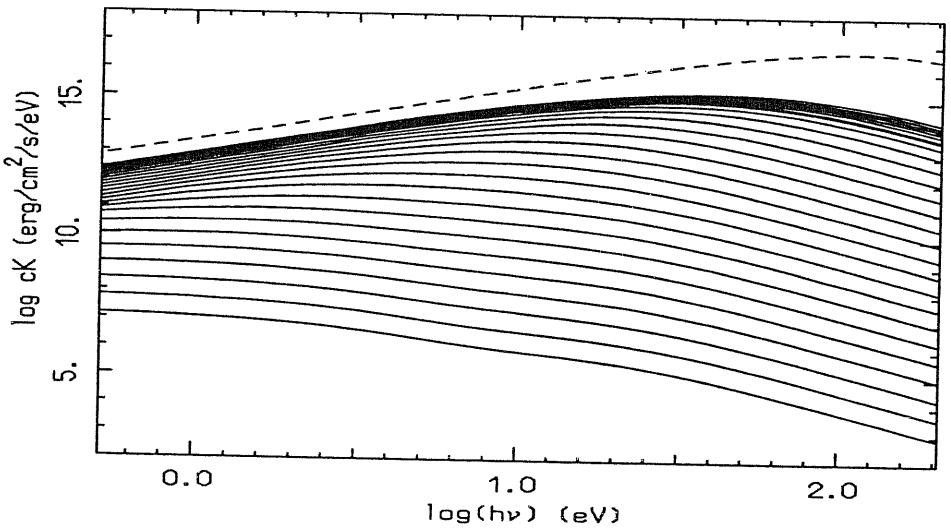

Figure 5.4: *Same as in figure 5.3 for the monochromatic radiation pressure.*

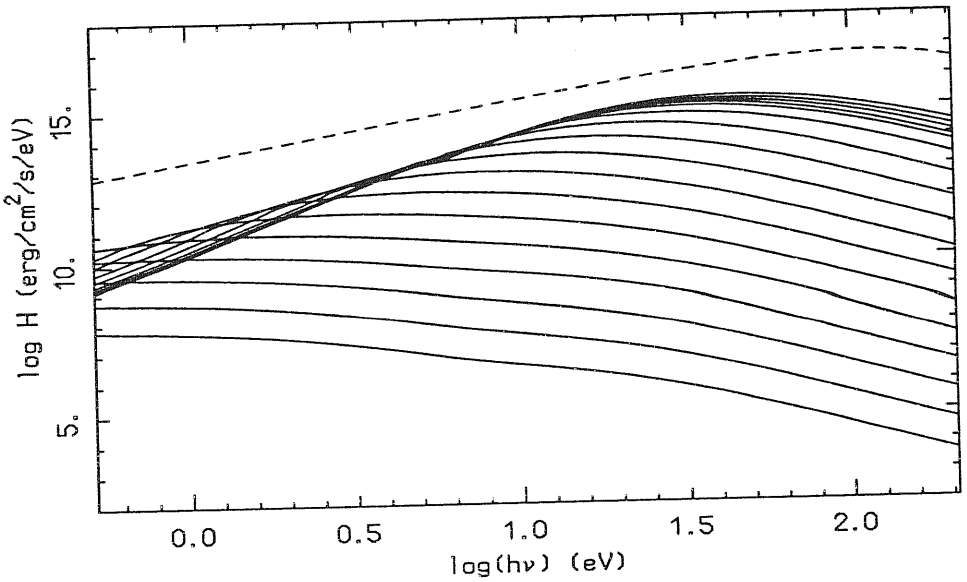

Figure 5.5: *Same as in figure 5.3 for the monochromatic flux.*

5.2 Accretion onto Black Holes: High–luminosity Solutions

In "hot" solutions temperature is much higher, typically $\sim 10^{10}$ K near to the horizon. As a consequence, free–free absorption is much lower than in "cold" models, even for larger accretion rates. Along the high–luminosity branch, thermal Comptonization is the dominant radiative process and it must be treated in its more general form, using expression (3.18). Here we consider the "hot" solution of NTZ91 with $\dot{m} = 71$, $\varrho_H = 10^{-4}\,\mathrm{g\,cm^{-3}}$; results from their frequency–integrated analysis are summarized in figure 5.6.

The flow is now effectively thin at all frequencies, although an inner core optically thick to scattering is present. The gas temperature in this model is in the range 10^5 K $\leq T \leq 10^{10}$ K, so we have chosen $\ln T_* = 21$ and $x_{\min} = 0.008$. Now the energy window is 0.9–4500 keV and $L = 35$ points have been used. Since the evaluation of the CSK integrals is very

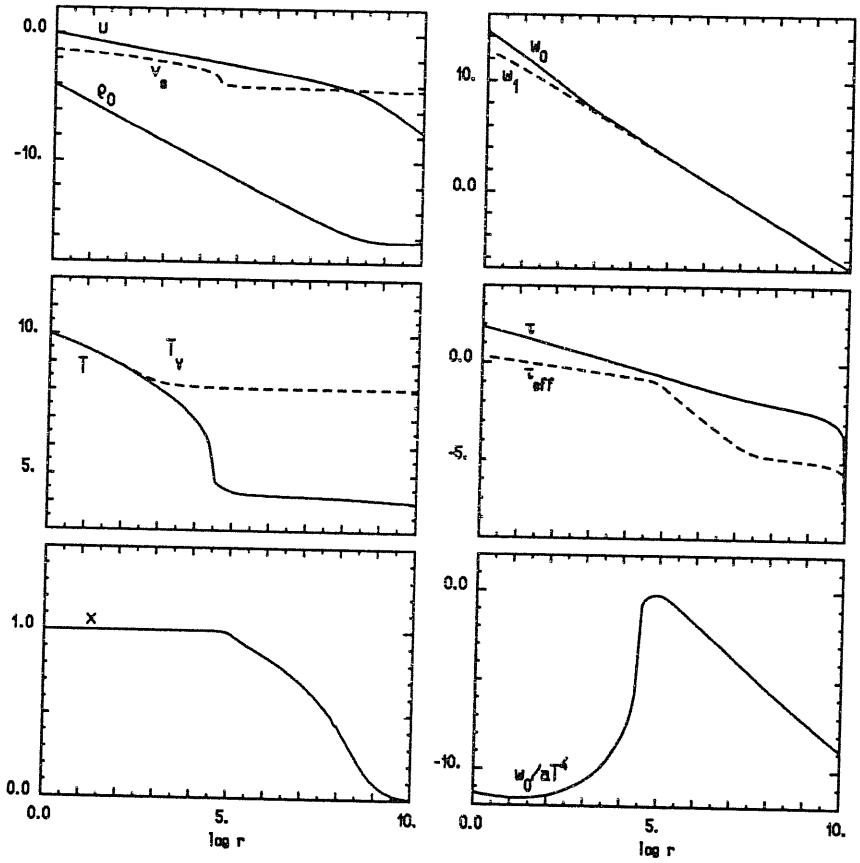

Figure 5.6: *Same as figure 5.2, but for* $(\varrho_0)_H = 1 \times 10^{-4}\ \mathrm{g\,cm^{-3}}$, $\dot{m} = 071$, *high-luminosity model. Taken from NTZ91.*

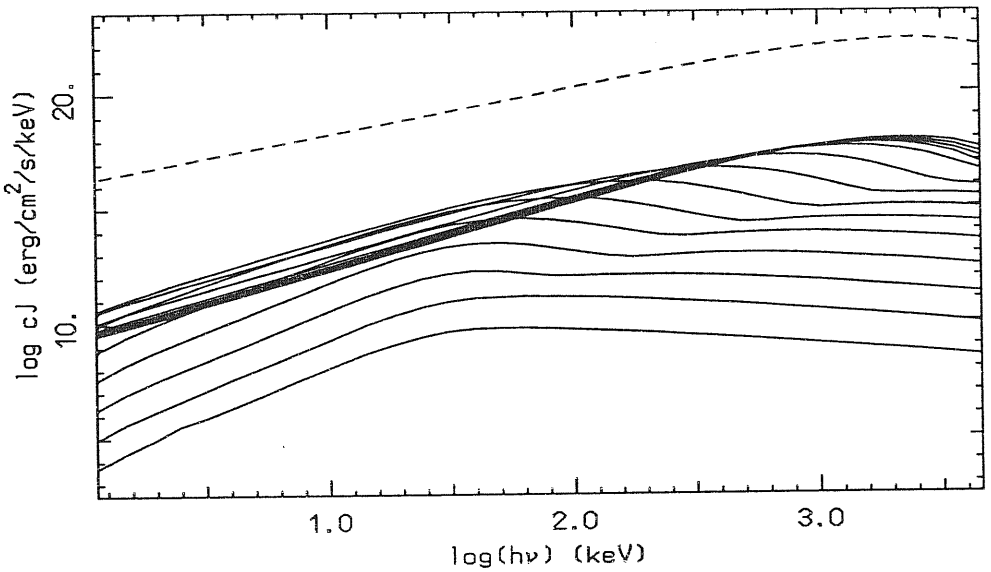

Figure 5.7: *Monochromatic mean intensity at different radii (full lines), together with the corresponding blackbody function at $T(r_{in})$ (dashed line), for "hot" accretion onto a black hole with $\dot{m} = 71$.*

time–consuming, both angular and radial resolution has been reduced with respect to the previous model: $N_1 = N_2 = N_3 = 10$, $N_4 = 30$ and $M = 110$ in the same radial domain. In this model convergence has been reached with a fractional accuracy better than 0.02, and the calculated radial gradient at infinity is -2.04.

The resulting mean intensity is presented in figure 5.7. In high temperature models, the mean intensity is always less than B_ν, but despite the accreting gas radiates less efficiently than in low–luminosity optically thick solutions, the efficiency of accretion process is higher, due to the fact that the matter temperature is now higher in the whole photospheric region. Since the emergent spectrum is peaked at about 40 keV, these solutions, if stable (see NTZ91 and Zampieri, Miller & Turolla 1996), seem to provide a natural way to produce hard X–ray radiation with reasonable efficiency out of spherical accretion onto black holes.

6 Dynamical Comptonization in Spherical Flows

It was realized long ago (Cowsik & Lee 1982 and references therein) that the divergence of the velocity field in astrophysical flows can provide a very efficient mechanism to transfer energy from the fluid to particles (photons, neutrinos, cosmic rays) diffusing through the medium, even in the absence of shocks. In the case of photons undergoing multiple scatterings off cold electrons, this effect is germane to thermal Comptonization, with the flow velocity v playing the role of the thermal velocity, and is sometimes referred to as dynamical Comptonization. In a series of papers Blandford & Payne (1981a,b; Payne & Blandford 1981, here PB as already defined) were the first to emphasize the importance of repeated scatterings in a steady, spherical flow of depth $\tau_{es} \gg 1$. They have shown that monochromatic photons injected in a region where $\tau_{es} v/c \sim 1$ always gain energy, because of adiabatic compression, and emerge with a broad distribution which exhibits a distinctive power–law, high–energy tail. Under the assumption that $v \propto r^{\beta}$, the spectral index depends only on β.

Cowsik & Lee (1982), and later Schneider & Bogdan (1989), stressed that Blandford &

Payne diffusion equation for the photon occupation number could be regarded as a particular case of the standard cosmic–ray transport equation in which the diffusion coefficient, $\kappa \propto r^{\alpha}\nu^{\gamma}$, does not depend on the photon energy ($\gamma = 0$) and $\alpha - \beta = 2$. Starting from this result, Schneider & Bogdan were able to generalize PB analysis to include the transition between Thomson ($\gamma = 0$) and Klein–Nishina ($\gamma = 1$) scattering cross–sections. The competitive role of dynamical and thermal Comptonization in accretion flows with a non–zero electron temperature was studied by Colpi (1988). More recently, Mastichiadis & Kylafis (1992) investigated the effects of dynamical Comptonization in near–critical accretion onto a neutron star. Their approach is very similar to PB, but the presence of a perfectly reflecting inner boundary (either the NS surface or the magnetosphere) was taken into account. They have shown that, in this case, the emergent spectrum is much harder than in PB and that the spectral index depends both on β and on the depth at the inner boundary.

Even when dealing with black hole accretion, all previous analyses neglected both special and general relativity. The presence of an event horizon was not considered and only terms up to first order in v/c were retained. In this Chapter we first review the PB calculations and then we present an extension of their analysis, accounting for relativistic effects on radiative transfer which arise when the flow velocity approaches the speed of light in the vicinity of the hole horizon. The motivation for this work is twofold. First: to investigate the properties of the emergent spectrum in a more realistic accretion scenario, in which the optical depth near the horizon is not so large to prevent photons from escaping. Second: to check by means of an analytical calculation the numerical results obtained with the

characteristics code, solving the complete transfer problem. Computed spectra show, in fact, a power–law, high–energy tail but the spectral index depends on the optical depth at the horizon, even for fixed $\beta = -1/2$, and it is always smaller than 2 (PB result). Here we show that advection/aberration effects in the high–speed flow near the horizon, due to the finiteness of the depth there, produce a power–law tail flatter with respect to PB and enable photons to drift also towards energies lower than the injection energy. The possible consequences of these results have been discussed by Nobili (1997) in connection with radiatively driven jets.

The calculation presented here is a part of a more general work about effects of dynamical comptonization, that has been recently published by Turolla *et al.* (1996). In this paper we also presented an analysis of expanding atmospheres, carried out under the same assumptions of PB. We found that the solution for the emergent flux shows specular features with respect to PB. Adiabatic expansion produces a drift of injected monochromatic photons to lower energies and the formation of low–energy, power–law tail. However, the spectral index is now independent on the velocity gradient and turns out to be always equal to -3. The details of the calculation will not be reported here, since they outside the hope of this thesis; however, for the sake of completeness, in section 6.3 we report a short review of the main results.

6.1 Radiative Transfer in a Converging Flow

In this and in the following sections we deal with the transfer of radiation through a scattering, steady, spherical flow, characterized by a power–law velocity profile $v \propto r^{\beta}$. Under these assumptions the rest–mass conservation yields immediately a density profile $\varrho \propto r^{-2-\beta}$ from which it follows that the electron–scattering optical depth is $\tau_{es} = \kappa_{es}\varrho r/(1+\beta) \propto r^{-1-\beta}$. The parameter β is positive for outflows and it has to be $\beta > -1$ for the optical depth to decrease with increasing r.

Blandford & Payne (1981a, b) and PB restricted their analysis to converging flows with a non–relativistic bulk velocity and to conservative and isotropic scattering in the electron rest frame. Combining the first two moment equations, written in an inertial frame, they found that, in diffusion approximation, the (angle–averaged) photon occupation number

$$n = \frac{1}{2}\int_{-1}^{1} N d\mu \tag{6.1}$$

obeys a Fokker–Planck equation. Defining $\tau^* = 3\tau_{es}v$ and looking for separable solutions of the form

$$n(\nu, \tau^*) = f(\tau^*)\tau^{*3+\beta}\nu^{-\lambda}, \tag{6.2}$$

the resulting second order ordinary differential equation for f reduces to a confluent hypergeometric equation (here the sign of β is the opposite with respect to PB, e.g. $\beta = -1/2$ for free–fall, according to the assumptions at the beginning of this section). As discussed by PB, the solution corresponding to a constant radiative flux at infinity and to adiabatic compression of photons for $\tau_{es} \to \infty$ is expressed in terms of the Laguerre polynomial $L_n^{(3+\beta)}(\tau^*)$.

The above two conditions give rise to a discrete set of eigenvalues for the photon index λ which are given by

$$\lambda_n = \frac{3\,(n+3+\beta)}{(2+\beta)} \qquad (n = 0, 1, 2, \ldots) \tag{6.3}$$

The general solution is written as the superposition of different modes. Assuming that monochromatic photons with $\nu = \nu_0$ are injected at $\tau^* = \tau_0^*$, it is

$$n \propto \tau^{*3+\beta} \sum_{n=0}^{\infty} \frac{\Gamma(n+1)}{\Gamma(n+4+\beta)} L_n^{(3+\beta)}(\tau_0^*) L_n^{(3+\beta)}(\tau^*) \left(\frac{\nu}{\nu_0}\right)^{-\lambda_n} . \tag{6.4}$$

In this case, bulk motion comptonization tends to create a power law, high energy tail. Defining the spectral index as

$$\alpha = -\frac{d \ln L\,(\nu, 0)}{d \ln \nu} \tag{6.5}$$

where L is the luminosity, PB found

$$\lim_{\nu \to \infty} \alpha = \frac{3}{2+\beta} \tag{6.6}$$

showing that the spectral slope at high frequencies is dominated by the fundamental mode $n = 0$. In particular, it is $\alpha = 2$ for a free–falling gas.

The same results can be recovered using the (scalar) PSTF moment formalism introduced by Th81, as shown by Nobili, Turolla & Zampieri (1993). Here we outline the general method, mainly to introduce some basic concepts that will be used in the following sections. In particular, we consider the first two PSTF moment equations, specializing the system (2.24) to a Schwarzschild metric, with only Thomson scattering included in the source term.

In the frame comoving with the fluid they read

$$\frac{\partial w^1_\nu}{\partial \ln r} + 2w^1_\nu + \frac{y'}{y}\left(w^1_\nu - \frac{\partial w^1_\nu}{\partial \ln \nu}\right) - v\left[\frac{\partial w^0_\nu}{\partial \ln r} + (1-\beta)\frac{\partial w^2_\nu}{\partial \ln \nu} - (2+\beta)\left(\frac{1}{3}\frac{\partial w^0_\nu}{\partial \ln \nu} - w^0_\nu\right)\right] = 0 \tag{6.7}$$

$$\begin{aligned}\frac{1}{3}\frac{\partial w^0_\nu}{\partial \ln r} &+ \frac{\partial w^2_\nu}{\partial \ln r} + 3w^2_\nu - \frac{y'}{y}\frac{\partial w^2_\nu}{\partial \ln \nu} + \frac{y'}{y}\left(w^0_\nu - \frac{1}{3}\frac{\partial w^0_\nu}{\partial \ln \nu}\right) - v\left[-\frac{3}{5}(4+\beta)w^1_\nu\right. \\ &- \left.\frac{1}{5}(2+3\beta)\frac{\partial w^1_\nu}{\partial \ln \nu} + \frac{\partial w^1_\nu}{\partial \ln r} + (1-\beta)\left(w^3_\nu + \frac{\partial w^3_\nu}{\partial \ln \nu}\right)\right] + \frac{(1+\beta)\tau_{es}}{y}w^1_\nu = 0\,.\end{aligned} \tag{6.8}$$

where a prime denotes the total derivative wrt $\ln r$, v is taken positive for inward motion and the quantity $y = \sqrt{1-1/r}/\sqrt{1-v^2}$ was already introduced in chapter 2. As discussed by Turolla & Nobili (1988, see also Thorne, Flammang & Żytkow 1981), in diffusion approximation the hierarchy of the frequency–integrated PSTF moments w^l is such that

$$\begin{aligned} w^1 &\sim \frac{w^0}{\tau_{es}} \\ w^2 &\sim \frac{w^0}{\tau_{es}}\left(\frac{1}{\tau_{es}} - v\right) \\ w^3 &\sim \frac{w^0}{\tau^2_{es}}\left(\frac{1}{\tau_{es}} - v\right)\,. \end{aligned} \tag{6.9}$$

The same hierarchy can be assumed to hold also for frequency–dependent moments in a scattering medium.

PB result can be reproduced in the limit of large τ_{es} and small v, i.e. retaining in equations (6.7), (6.8) only terms of order w^0_ν, vw^0_ν and w^0_ν/τ_{es}, and suppressing gravity, which is equivalent to set $y = 1$ and $y' = 0$. In particular, under such hypothesis, all terms

containing both w_ν^2 and w_ν^3 can be neglected and the moment equations become

$$\frac{\partial w_\nu^1}{\partial \ln t} - v\frac{\partial w_\nu^0}{\partial \ln t} - 2w_\nu^1 + v(2+\beta)\left(w_\nu^0 - \frac{1}{3}\frac{\partial w_\nu^0}{\partial \ln \nu}\right) = 0 \tag{6.10}$$

$$v\frac{\partial w_\nu^0}{\partial \ln t} - tw_\nu^1 = 0\,, \tag{6.11}$$

where $t = (1+\beta)\tau^*$. Equations (6.10) and (6.11) can be combined together to yield a second order, partial differential equation for the radiative flux

$$t\frac{\partial^2 w_\nu^1}{\partial t^2} - (t+1-\beta)\frac{\partial w_\nu^1}{\partial t} + \left(1 - \frac{2\beta}{t}\right)w_\nu^1 - \frac{2+\beta}{3}\frac{\partial w_\nu^1}{\partial \ln \nu} = 0\,. \tag{6.12}$$

Following PB, the solution of equation (6.12) can be found by separation of variables. Writing $w_\nu^1 = t^p h_1(t)\nu^{-\alpha}$, it is easy to show that for $p = 2$ and for $p = -\beta$, equation (6.11) becomes a confluent hypergeometric equation for h_1. Actually the requirement of constant radiative flux at infinity is met only for $p = 2$, and in this case we get

$$t\frac{d^2 h_1}{dt^2} + (3+\beta-t)\frac{dh_1}{dt} - \left(1 - \frac{2+\beta}{3}\alpha\right)h_1 = 0\,. \tag{6.13}$$

As previously discussed, the physical solution for w_ν^1 can be obtained as a superposition of the Kummer functions $M(-n, 3+\beta, t) \propto L_n^{(2+\beta)}(t)$, for $n = 0, 1, \ldots$, with corresponding eigenvalues

$$\alpha_n = \frac{3(n+1)}{2+\beta}\,. \tag{6.14}$$

In this case

$$w_\nu^1 = t^2 \sum_{n=0}^{\infty} A_n L_n^{(2+\beta)}(t)\nu^{-\alpha_n}\,, \tag{6.15}$$

where the A_n's are constants to be fixed by the boundary conditions. At sufficiently large frequencies the spectrum is dominated by the fundamental mode; in particular, for $\beta = -1/2$, it is again $\alpha_0 = 2$.

6.2 Importance of Relativistic Effects

Here we consider the effects of dynamical Comptonization in spherical accretion onto a non–rotating black hole, taking into full account both gravity and velocity terms in the moment equations. With reference to this particular problem, we can assume that matter is free–falling, $v = r^{\beta}$ with $\beta = -1/2$. In this case dynamics cancels, locally, gravity, so that $y = 1$, $y' = 0$. The moment equations look then "non–relativistic" in form, although v can be arbitrarily close to unity. Corrections due to large values of the flow velocity were not considered in previous works despite the fact that they are bounded to become important near the event horizon where $v \sim 1$. We note that the bulk of the emission in realistic accretion models is expected to come precisely from the region close to r_g. As in the non–relativistic analysis presented in the last section, we consider the diffusion limit, truncating self–consistently both equations (6.7), (6.8) to terms of order w^0_ν/τ_{es}. The moments hierarchy, expressions (6.9), shows that all terms containing w^3_ν can be always neglected in equation (6.8), since they are of order w^0_ν/τ^2_{es}. In the present case, however, all other terms must be retained. In fact, $vw^1_\nu \sim w^1_\nu \sim w^0_\nu/\tau_{es}$ when $v \sim 1$ and $w^2_\nu \sim w^0_\nu/\tau_{es}$, at least for $v \sim 1 \gtrsim 1/\tau_{es}$ (see again expressions [6.9]). This implies that w^1_ν and w^2_ν contribute to the same extent to the anisotropy of the radiation field. Note that under such conditions it is $w^2 = 4\pi(K - J/3) < 0$, as already pointed out by Turolla & Nobili (1988), so that in high–speed, diffusive flows K may become less than $J/3$. Contrary to the case discussed in section 6.1 where w^2_ν is negligible, now the system of the first two moment equations is not closed. However, up to terms of order w^0_ν/τ_{es}, the second moment equation does not

contain moments of order higher than w_ν^2 and provides then the required closure equation

$$v\frac{\partial w_\nu^2}{\partial \ln t} - \frac{4}{15}\frac{\partial w_\nu^1}{\partial \ln t} - \frac{15}{14}vw_\nu^2 - \frac{4}{15}w_\nu^1 + \frac{2}{5}vw_\nu^0 + \frac{3}{14}v\frac{\partial w_\nu^2}{\partial \ln \nu} - \frac{2}{15}v\frac{\partial w_\nu^0}{\partial \ln \nu} + \frac{3}{10}\frac{t}{v}w_\nu^2 = 0\,. \quad (6.16)$$

The complete system (6.7), (6.8) and (6.16) is awkward and a solution can be obtained only numerically. It is possible, nevertheless, to find an analytical solution if we consider the closure condition for w_ν^2 which follows from equation (6.16) with only terms of order w_ν^0 retained

$$w_\nu^2 = \frac{4}{9}\frac{v}{t}\left(\frac{\partial w_\nu^0}{\partial \ln \nu} - 3w_\nu^0\right)\,. \quad (6.17)$$

With this closure, w_ν^2 is always negative provided that $\partial w_\nu^0/\partial \ln \nu < 0$. This implies that equation (6.17) is strictly valid only for $\tau_{es}v \gtrsim 1$ (see expression [6.9]), that is to say below the trapping radius. Introducing the new dependent variables $f_0 = vw_\nu^0$, $f_1 = w_\nu^1$ and $f_2 = vw_\nu^2$, the moment equations become

$$t\frac{\partial f_0}{\partial t} + \frac{1}{2}\frac{\partial f_0}{\partial \log \nu} - 2f_0 - t\frac{\partial f_1}{\partial t} + 2f_1 - \frac{3}{2}\frac{\partial f_2}{\partial \log \nu} = 0 \quad (6.18)$$

$$\frac{t}{3}\frac{\partial f_0}{\partial t} - \frac{1}{6}f_0 - \frac{t}{t_h}\left[t\frac{\partial f_1}{\partial t} + \frac{1}{10}\frac{\partial f_1}{\partial \log \nu} + \left(\frac{t_h}{3} - \frac{9}{10}\right)f_1\right] + t\frac{\partial f_2}{\partial t} - \frac{7}{2}f_2 = 0 \quad (6.19)$$

$$f_2 - \frac{4}{9t_h}\left(\frac{\partial f_0}{\partial \log \nu} - 3f_0\right) = 0\,, \quad (6.20)$$

where t_h is the value of t at the radius where $v = 1$, i.e. at $r = 1$ in the case under examination. We note that for $t_h \to \infty$ equations (6.18), (6.19) give exactly the low–velocity limit of PB (equations [6.10], [6.11]), irrespective of the value of v. This is because when $t_h \to \infty$ the scattering depth itself near the horizon must be very large, so the radiation field there is very nearly isotropic. Departures from isotropy, due both to the radiative flux $w_\nu^1 \sim w_\nu^0/\tau_{es}$ and to the radiative shear $w_\nu^2 \sim (1/\tau_{es} - v)w_\nu^0/\tau_{es}$ become vanishingly

small, no matter how large velocity is. Under such conditions PB approach is still valid just because *both* w_ν^1 and w_ν^2 become negligible in the moment equations, although they may be of the same order.

The system (6.18), (6.19), (6.20) can be solved looking again for separable solutions of the type $f_i = g_i(t)\nu^{-\alpha}$. After some manipulation, it can be transformed into a pair of decoupled, second order, ordinary differential equation for $g_0(t)$ and $g_1(t)$, having the same structure. In particular for $g_1(t)$ it is

$$t^2(\beta t+\gamma)\frac{d^2g_1}{dt^2}+t(\delta t+\epsilon)\frac{dg_1}{dt}-(\eta t+\lambda)g_1=0 \tag{6.21}$$

where

$$\begin{aligned}
\beta &= 60t_h\,,\\
\gamma &= -(20/3)t_h\left[3t_h-4(3+\alpha)\right]\,,\\
\delta &= 20t_h^2-18(2\alpha+3)t_h-40\alpha(3+\alpha)\,,\\
\epsilon &= 30t_h\left[t_h-4(3+\alpha)\right]\,,\\
\eta &= 10(\alpha+2)t_h^2+\left(31\alpha^2/3+7\alpha-54\right)t_h-4\alpha(\alpha+3)(\alpha+9)\,,\\
\lambda &= (20/3)t_h\left[3t_h-28(3+\alpha)\right]\,.
\end{aligned}$$

Equation (6.21) can be reduced to a hypergeometric equation upon the change of variables $g_1(t)=t^p h_1(z)$ and $z=-(\beta/\gamma)t$, where p is the solution of the quadratic equation $\gamma p^2+(\epsilon-\gamma)p-\lambda=0$. A direct, but tedious, calculation shows that

$$\begin{aligned}
p_+ &= 2\\
p_- &= \frac{7}{2}-\frac{9t_h}{3t_h-4(3+\alpha)}\,;
\end{aligned} \tag{6.22}$$

in the limit $t_h \to \infty$, $p_- = 1/2$ as in the case considered in the previous section, and $p = p_+$ will be used in the following to meet the requirement of constant radiative flux at infinity. Equation (6.21) can be now written in the form

$$z(1-z)\frac{d^2h_1}{dz^2} + \left[\frac{\epsilon}{\gamma} + 2p - \left(\frac{\delta}{\beta} + 2p\right)z\right]\frac{dh_1}{dz} - \left[p(p-1) + p\frac{\delta}{\beta} - \frac{\eta}{\beta}\right]h_1 = 0 \qquad (6.23)$$

which is a hypergeometric equation. The general solution is expressed in terms of the hypergeometric function ${}_2F_1(a,b,c;z)$ and the three parameters a, b, c (see Abramowitz & Stegun 1972, AS in the following, for notation) are given by the relations

$$c = \frac{\epsilon}{\gamma} + 2p$$
$$a + b + 1 = \frac{\delta}{\beta} + 2p$$
$$ab = p(p-1) + p\frac{\delta}{\beta} - \frac{\eta}{\beta}.$$

Solving for a, b we obtain, after a considerable amount of algebra,

$$a = \frac{2-\alpha}{2} - \frac{2\alpha(\alpha+3)}{3t_h} \qquad (6.24)$$

$$b = \frac{t_h}{3} + \frac{11-\alpha}{10}. \qquad (6.25)$$

It can be seen from equations (6.24), (6.25) that, in the limit $t_h \to \infty$, b diverges while a stays finite; in the same limit the hypergeometric equation reduces to the confluent hypergeometric equation (see e.g. Sneddon 1956). As discussed in section 6.1, the relevant solution in the non-relativistic case is given by Laguerre polynomials and is recovered imposing $a = -n$, with $n = 0, 1, \ldots$. The solution of equation (6.23) which reduces to PB for $t_h \to \infty$ is found imposing again that a is either zero or a negative integer (although

other classes of solutions that do not match PB may exist). In this case h_1 is still polynomial and takes the form

$$h_1(z) = {}_2F_1(-n, b, c; z) = \frac{n!}{(c)_n} P_n^{(c-1,b-c-n)}(1-2z)\,, \tag{6.26}$$

where $P_n^{(p,q)}(z)$ is the Jacobi polynomial and $(c)_n = \Gamma(c+n)/\Gamma(c)$ is the Pochhammer's symbol (see again AS). For $t_h \to \infty$, it is $c \sim 5/2$, $b \sim t_h/3$, $z \sim 3t/t_h = t/b$ and

$$P_n^{(c-1,b-c-n)}\left(1-2\frac{t}{b}\right) \to L_n^{(3/2)}(t)\,, \tag{6.27}$$

so that, as expected, the solution of section 6.1 is recovered.

The discrete set of eigenvalues for the spectral index α_n follows immediately from (6.24) solving the quadratic equation $a = -n$. For each n both a positive, α_n^+, and a negative, α_n^-, mode is present

$$\alpha_n^{\pm} = \frac{-(12+3t_h) \pm \sqrt{(12+3t_h)^2 + 96(n+1)t_h}}{8}\,. \tag{6.28}$$

We checked that the eigenvalues of the equation for g_0 are again given by equation (6.28), in agreement with the starting hypothesis that α is the same for all moments.

The general solution for the spectral flux is obtained as a linear superposition of all modes

$$\begin{aligned} w_\nu^1 &= t^2 \left[\sum_{n=0}^{\infty} A_n^+ (-1)^n \frac{(b)_n}{(c)_n} G_n(b-n, c, z) \left(\frac{\nu}{\nu_0}\right)^{-\alpha_n^+} \right. \\ &+ \left. \sum_{n=0}^{\infty} A_n^- (-1)^n \frac{(b)_n}{(c)_n} G_n(b-n, c, z) \left(\frac{\nu}{\nu_0}\right)^{-\alpha_n^-} \right], \end{aligned} \tag{6.29}$$

where we have expressed h_1 in terms of the shifted Jacobi polynomials G_n. We remind that b, c and z are all functions of $\alpha_n^{\pm}$, although we dropped all indices to simplify the

notation. The two sets of constants $A_n^{\pm}$ are fixed imposing a boundary condition at the injection frequency $\nu = \nu_0$. The only boundary condition compatible with the assumption of a pure scattering flow for $t < t_h$ is that all photons are created in an infinitely thin shell at t_*. This is equivalent to ask that $w_\nu^1(t, \nu_0) \propto \delta(t/t_* - 1)$, as in PB.

At variance with the results discussed in section 6.1, now the series in equation (6.29) can not be summed using the polynomial generating function because b, c and z depend on n. The coefficients $A_n^{\pm}$ are solution of an upper triangular, infinite system of linear algebraic equations (see Appendix B). It can be easily shown that the two series in equation (6.29) do not converge for any value of ν/ν_0. In fact, the general term of the first series, which is of the type $f(n)(\nu_0/\nu)^{\alpha_n^+}$, can not be infinitesimal for arbitrarily small frequencies unless the series truncates, which is not the case if it must reproduce the δ–function at $\nu = \nu_0$. On the other hand, the series is absolutely convergent for $\nu > \nu_0$, provided that $|f(n)|$ is bounded. For $N \gg 1$, the series has a majorant $\propto \sum_{n=N}^{\infty}(\nu_0/\nu)^{\sqrt{n}}$ which is convergent because $\int_N^{\infty}(\nu_0/\nu)^{\sqrt{x}}\,dx$ is finite for $\nu > \nu_0$. The same argument applies to the second series for $\nu < \nu_0$, so that the solution satisfying our boundary condition is

$$w_\nu^1(t,\nu) = \begin{cases} t^2 \displaystyle\sum_{n=0}^{\infty} A_n^-(-1)^n \frac{(b)_n}{(c)_n} G_n(b-n,c,z) \left(\frac{\nu}{\nu_0}\right)^{-\alpha_n^-} & \text{if } \nu < \nu_0\,; \\ t^2 \displaystyle\sum_{n=0}^{\infty} A_n^+(-1)^n \frac{(b)_n}{(c)_n} G_n(b-n,c,z) \left(\frac{\nu}{\nu_0}\right)^{-\alpha_n^+} & \text{if } \nu \geq \nu_0\,. \end{cases} \tag{6.30}$$

Equation (6.30) exhibits two striking features, not shared by its non–relativistic counterpart, which arise from the presence of advection/aberration terms in the moment equations.

First of all, we note that according to equation (6.30) photons injected at $\nu = \nu_0$ can be shifted *both* to higher and lower energies by dynamical Comptonization. This is in apparent contrast with PB result that photons can only gain energy in scatterings with electrons in a converging flow (the adiabatic compression). PB statement is, however, correct up to $O(v)$ terms and their equation (8) is the low–velocity limit of the more general expression for the photon energy change along a geodesic (see e.g. Novikov & Thorne 1973)

$$\frac{1}{\nu}\frac{d\nu}{d\ell} = -\left(n^i a_i + \frac{1}{3}\theta + n^i n^j \sigma_{ij}\right) , \tag{6.31}$$

where n^i is the unit vector along the photon trajectory and a^i, θ and σ_{ij} are the flow 4–acceleration, expansion and shear, respectively. In free–fall a^i vanishes while it can be safely neglected in PB approximation being $O(v^2)$. The remaining two terms are both of order v

$$\begin{aligned} \theta &= -\frac{3}{2}\frac{v}{r} \\ n^i n^j \sigma_{ij} &= \frac{1}{2}\frac{v}{r}(3\mu^2 - 1) \end{aligned} \tag{6.32}$$

where μ is the cosine of the angle between the photon and the radial directions. The mean photon energy change can be obtained angle–averaging equation (6.31) over the specific intensity

$$I_\nu(\mu) = w_0 + 3\mu w_1 + \frac{15}{4}(3\mu^2 - 1)w_2 + \dots . \tag{6.33}$$

Recalling the behaviour of the radiation moments in the diffusion limit, we get

$$\left\langle \frac{1}{\nu}\frac{d\nu}{d\ell} \right\rangle = \frac{v}{r}\left[\frac{1}{2} + \frac{3}{\tau_{es}}\left(\frac{1}{\tau_{es}} - v\right)\right] . \tag{6.34}$$

The second term in square brackets arises because of shear and is negligible in PB approximation, being either $O(1/\tau_{es}^2)$ or $O(v/\tau_{es})$. This implies that the mean photon energy

change is always positive. However, when advection and aberration are taken into account (see equations [6.31], [6.32]) photons moving in a cone around the radial direction suffer an energy loss and the collective effect is stronger when the flow velocity approaches unity in regions of moderate optical depth.

The second important feature concerns the slope of the power–law, high–energy tail of the spectrum. From equation (6.28) the fundamental mode is

$$\alpha_0^+ = \frac{-(12+3t_h)+\sqrt{(12+3t_h)^2+96t_h}}{8}, \tag{6.35}$$

and, for large values of t_h, equation (6.35) gives

$$\alpha_0^+ = 2 - \frac{40}{3t_h} + \frac{1120}{9t_h^2} + O\left(1/t_h^3\right). \tag{6.36}$$

At large enough frequencies the spectral index is dominated by the fundamental mode which, for $t_h \gtrsim 1$, sensibly deviates from the value predicted by the non–relativistic calculation. Despite the fact that this effect is present below the trapping radius, we stress that, contrary to a widespread belief, the trapping radius does not act as a one–way membrane. Photons produced near or below the surface $\tau_{es}v = 1$ can still escape to infinity even if both the large optical depth and the strong advection caused by the inward flow dramatically reduce the emergent radiative flux. Moreover, these photons, although comparatively few, are the more strongly comptonized and will anyway dominate the high–energy tail of the spectral distribution. Equation (6.36) shows that the emergent spectrum turns out to be flatter with respect to PB case. The two main features of our solution, harder spectrum and drift of photons below ν_0, can be clearly seen in figure 6.1, where the emergent spectrum is shown for $t_h = 20$.

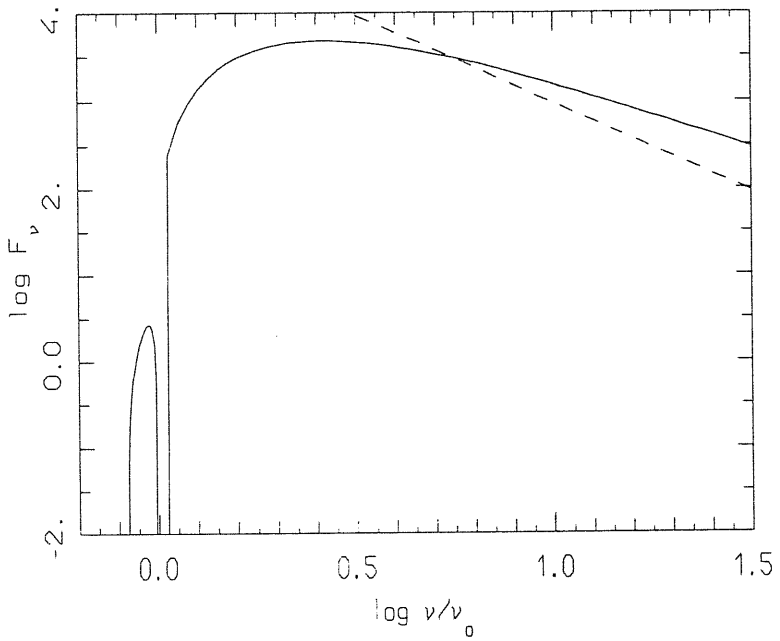

Figure 6.1: *Emergent flux F_ν (in arbitrary units) for spherical accretion onto a Schwarzschild black hole; here $t_h = 20$, $t_* = 0.9t_h$ and $\alpha_0^+ = 1.54$. At high energies the spectral index is flatter than 2, as can be seen by comparison with the dashed line.*

It is interesting to compare the present, analytical solution with the numerical result obtained using the fully GR characteristic–ray code previously described.

In figure 6.2 we show the emergent spectrum relative to the "cold" solution for black hole accretion by NTZ with $\varrho_h = 1.42 \times 10^{-5}$ g cm^{-3}. In this case both electron scattering and free–free emission/absorption are considered. At large enough frequencies scattering is the only source of opacity, so, in this limit, we expect our idealized analytical model to be representative of the realistic situation. The numerical model has $t_h \simeq 15$ which corresponds to $\alpha_0^+ = 1.43$. This value is in excellent agreement with the derived spectral index $\alpha = 1.36$.

On the other hand, due to the crudness of the assumptions under which the present

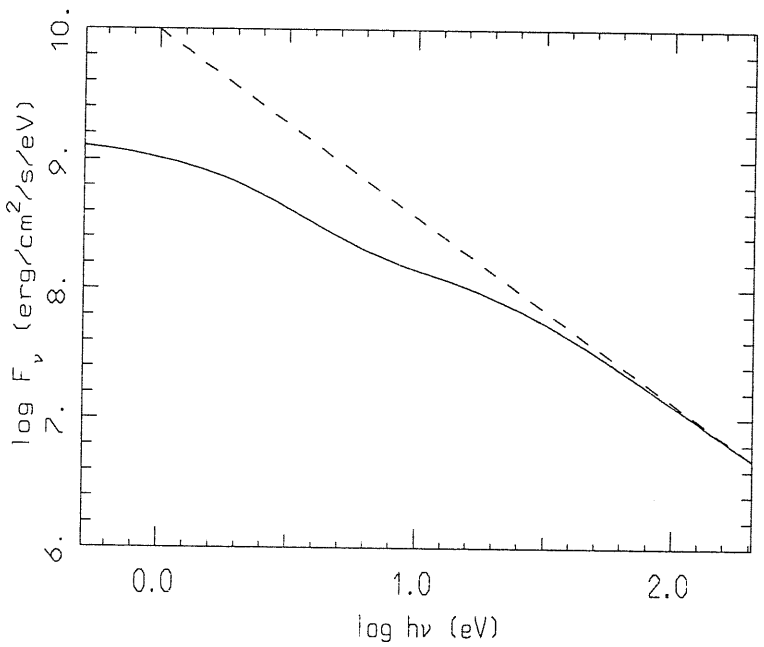

Figure 6.2: *Emergent flux F_ν computed using our CRM code; the derived spectral index is* 1.36. *In this model $t_h \simeq 15$ and the corresponding value of α_0^+ is* 1.43 *(dashed line).*

analytical investigation has been derived, its results can not be assumed to hold in all the parameter range along the "low" luminosity sequence of solutions. As an example, the model presented in section 5.1 corresponds to $t_h \sim 1$ (i.e. to a value of the scattering optical depth at the horizon $\tau_{es} \sim 0.3$). In that case the flow is optically thin all the way down the horizon and the diffusion approximation breaks down. Dynamical comptonization is still efficient in shaping a power–law, high energy tail, but its effects is not saturated. The emergent spectrum turns out to be softer ($\alpha = 2.9$), more reminding of the initial, thermal emission.

6.3 Radiative Transfer in an Expanding Atmosphere

In this section we briefly present results derived by Turolla *et al.* (1996) in the case of a pure scattering, expanding atmosphere. The basic assumptions are the same as in PB, and here we only review the main lines of the analytical calculation, to outline similarities and differences with respect to the case presented in section 6.1.

In the wind case, the power-law velocity profile can be written as $v = v_*(r/r_*)^3$, where the subscript "$_*$" refers to the base of the envelope, while the second order partial differential equation for the radiation flux is still given by equation (6.12). Clearly, the resulting equation could in principle be integrated using the same technique discussed in section 6.1 and looking for separable solutions $w_\nu^1 = t^2 h_1(t)\nu^{-\alpha}$. In fact, it can be easily checked that it can be still reduced to Kummer equation for $h_1(t)$, as in the converging flow case. A problem arises, however, as far as boundary conditions are concerned: in section 6.1 the only physically meaningful solution was selected asking that the flux become a constant for $t \to 0$ and that adiabatic compression of photons hold for $t \to \infty$. In that case the existence of these physical constraints was sufficient to fix univocally the mathematical solution. However, this particular issue turns out to be much more delicate in the wind problem.

There is, an alternative method of solution that looks more convenient when tackling with expanding flows, since it allows for an easier handling of boundary conditions. The starting point is the fact that, upon a suitable changement of both dependent and independent variables, the equation for w_ν^1 can be brought into a standard Fokker–Planck form,

describing diffusion of photons through the moving medium. The solution can be then found by performing a Fourier transform in the Fokker–Planck equation with respect to t, solving for the Fourier transform variable and then transforming back (see e.g. Risken 1989). Using this approach, the main advantage is that the Fourier transform automatically selects the regular solution. In fact, since it can be computed only for functions that are L_2 in $]-\infty,\infty[$, it is the method of solution itself which is suited for finding only regular solutions and in doing so no extra constraint is required.

Assuming as boundary condition that monochromatic photons of frequency ν_0 are injected at $t = t_*$, the final result can be written as

$$w_\nu^1 = \left(w_\nu^1\right)^0 \left(\frac{\nu}{\nu_0}\right)^{3/2} \left(\frac{t_*}{t}\right)^{(2+\beta)/2} \left[1-\left(\frac{\nu}{\nu_0}\right)^{3/(2+\beta)}\right]^{-1} \times \exp\left[-\frac{t+(\nu/\nu_0)^{3/(2+\beta)}\,t_*}{1-(\nu/\nu_0)^{3/(2+\beta)}}\right] I_{2+\beta}\left[2\sqrt{(\nu/\nu_0)^{2/(3+\beta)}t_* t}\Big/\left(1-(\nu/\nu_0)^{2/(3+\beta)}\right)\right], \tag{6.37}$$

where $\left(w_\nu^1\right)^0$ is the flux at $\nu = \nu_0$ and I_q are the modified Bessel function (see AS). The main result is that the spectrum is shifted now towards lower frequencies and it broadens at the same time, developing a power law, low–energy tail. The overall behaviour is similar to that of the converging flow but somehow reversed, since now photons can drift only to frequencies lower than ν_0. There is, however, a major difference in the power–law index α between the two cases since α does not depend on β for the wind solutions, as can be seen examining the spectral behaviour of equation (6.37) at low frequencies. Since $I_q(z) \sim (z/2)^q/\Gamma(q+1)$ when the argument is small, for $\nu \ll \nu_0$ the emergent luminosity is

$$L_\nu \propto \left(\frac{\nu}{\nu_0}\right)^3 \exp\left[-\frac{(\nu/\nu_0)^{(2+\beta)/3}\,t_*}{1-(\nu/\nu_0)^{(2+\beta)/3}}\right]\left[1-\left(\frac{\nu}{\nu_0}\right)^{(2+\beta)/3}\right]^{-3-\beta} \sim \left(\frac{\nu}{\nu_0}\right)^3. \tag{6.38}$$

This shows that $\alpha = -3$, irrespective of the value of β.

6.4 Summary and Concluding Remarks

In the previous chapter we presented the numerical computation of the emergent spectrum correspondent to "cold" solutions for black hole accretion. Due to the low temperatures expected in the atmosphere the thermal comptonization plays a negligible role: as a consequence, these regimes represent an ideal arena to perform a systematic investigation of effects of dynamics in the transfer of radiation in a scattering, spherically–symmetric medium. The presence in the spectrum of some unexpected features initially motivated our efforts in reconsidering the problem from an analytical point of view. Simple and physically intuitive analytic results, even those based on crude approximations, are, in fact, inavaluable aids in interpreting the output of more realistic numerical models.

Here we have presented the extension of the PB analysis of bulk motion comptonization in converging flows to the relativistic case. In the low–velocity limit and assuming diffusion approximation, PB found that monochromatic photons injected at the base of the atmosphere always gain energy as they propagate outwards. The emergent spectrum exhibits an overall shift to higher frequencies and a power–law, high–energy tail with a spectral index that only depends on the velocity gradient. Under the same assumptions, the wind solution shows similar, although reversed, features. Adiabatic expansion now produces an overall drift toward lower energies and the formation of a power–law tail at low frequencies. In this case, however, the spectral index is independent on the velocity gradient and turns out to

be always equal to -3.

Both these analyses are correct to first order in v/c and can be thought to adequately describe situations in which bulk motion is non–relativistic in regions of moderate scattering depth. Relativistic corrections are, in fact, related to the anisotropy of the radiation field and are washed out if $\tau_{es} \gg 1$. Obviously, if the flow is optically thin, repeated scatterings are ineffective no matter how large the velocity is. In outflowing atmospheres high velocities are expected at large radii, where the optical depth has dropped below unity, so that the assumption under which results presented in section 6.3 are obtained can be reasonable. On the other hand, in accretion flows onto compact objects the condition $\tau_{es} \gg 1$ where $v \sim 1$ is likely to be met only when the accretion rate becomes hypercritical. This shows that a relativistic treatment of dynamical comptonization is indeed required in investigating the emission properties of accretion flows. For $v \sim 1$ the diffusion limit is not recovered simply asking that the radiative flux is proportional to the gradient of the energy density, since the radiative shear is as important as the flux. Relativistic corrections produces two main effects: first, photons are shifted toward *both* higher and lower frequencies by dynamical comptonization and, second, the spectrum at large frequencies is sensibly flatter than in the non–relativistic case. The spectral index now depends not only on the velocity gradient, but also on the value of the scattering depth at the horizon and goes to its non–relativistic limit when $(\tau_{es})_h$ tends to infinity. Despite the fact that relativistic effects are important only where $\tau_{es} v > 1$, that is to say below the trapping radius, their signature is still present in the emergent spectrum. In particular, the high energy tail is populated by photons

coming from the region below the trapping radius. In the presence of a strong advection, these photons are comparatively few (yet, the emergent flux is rather sensitive to the value of the optical depth), but just these photons are also the most strongly comptonized by the repeated scattering. A similar effect was found by Mastichiadis & Kylafis (1992, see also Zampieri, Turolla, & Treves 1993) in an accretion flow onto a neutron star. In their case the formation of an essentially flat ($\alpha \simeq 0$) spectrum is due to the fact that photons experience a very large number of energetic scatterings before emerging to infinity, since no advection is present being the star surface a perfect reflector. Our spectrum is softer with respect to Mastichiadis & Kylafis just because a sizable fraction of the more boosted photons are dragged into the hole, but, at the same time, it is harder than PB since in the relativistic regime the mean energy gain per scattering is higher. From the mathematical point of view it is noteworthy that the assumption of a finite optical depth at the inner boundary (i.e. at the horizon in our model or at the reflecting surface in Mastichiadis & Kylafis) produces a fundamental mode which is flatter with respect to PB; in both cases PB result is recovered in the limit $(\tau_{es})_h \rightarrow \infty$. The possibility that scattering of photons in an accretion flow onto a black hole produces a power–law tail with spectral index larger than 2 was also suggested in a very recent paper by Ebisawa, Titarchuk, & Chakrabarti (1996). Using a semi–qualitative analysis they found that the spectral index is close to 3/2 for large values of the optical depth at the horizon and discussed the possible relevance of this result in connection with the observed hard X–ray emission from black hole candidates in the high state.

We note that for $1 < (\tau_{es})_h < 32/9$ the predicted spectral index (see equation [6.35]) is smaller than 1, implying a divergent frequency–integrated luminosity. It should be taken into account, however, that for such low values of the optical depth the diffusion approximation itself becomes questionable. Moreover, when $h\nu \approx m_e c^2$ the electron recoil in the particle rest frame can not be neglected anymore, so for large enough energies our treatment is not valid (see Zampieri 1995 for a more detailed discussion). The decrease of the cross–section in the quantum limit makes the scattering process less efficient, producing a sharp cut–off in the spectral distribution. Effects of the Klein–Nishina corrections in the scattering cross section were recently investigated by Psaltis & Lamb (1997). Finally, as already stressed by Blandford & Payne (1981a) and Colpi (1988), thermal comptonization dominates over dynamical comptonization when $v^2 \lesssim 12kT/m_e$. The spectral distribution depends then on the relative strength of competitive processes such as heating/cooling by thermal comptonization and compressional heating and must be derived solving the radiative transfer equation in its complete form.

7 Static, Plane–Parallel Atmospheres around Neutron Stars

In the following of this thesis we shall deal with a different kind of astrophysical systems, and we will consider situations in which the accreting compact object is a neutron star (NS). Since the late 60's large theoretical efforts have been devoted to investigate the properties of radiation produced by accretion onto neutron stars, in the attempt to model the observed spectra of galactic X–ray sources. The complete analysis of a steady–state, spherically symmetric gas flow onto a compact star is a complex task since the appearance of shocks and/or of a boundary layer at the neutron star surface should be expected. However, some reasonable simplifying assumptions can be introduced. First of all we note that, for a neutron star of mass $M_* \sim 1.5 M_\odot$ and radius $R_* \sim 10$ km, the efficiency of the accretion process is $\epsilon \sim 0.1$. By comparing this value for with the typical efficiency attainable in black hole accretion (see NTZ91), it follows that only a very tiny fraction ($\lesssim 0.01$) of the total energy output can be radiate by the infalling gas, before the impact with the surface of the star. Emission processes in the accreting gas can be therefore safely neglected, and in the standard picture all the emerging radiation is produced in a geometrically thin atmosphere

where protons are decelerated by Coulomb collisions and/or plasma interactions.

Equilibrium solutions for spherical, hydrostatic atmospheres around unmagnetized NSs were first provided by Zel'dovich & Shakura (1969, ZS in the following) in the frequency–integrated case. These results were then corroborated with a more detailed, numerical work by Alme & Wilson (1973, AW), who also presented the first spectral analysis, revealing the fundamental role played by Comptonization of primary bremsstrahlung photons in establishing the thermal balance in the emitting gas and the properties of the emerging radiation. In these investigations the interest mainly focussed on emergent spectra for luminosities in the range $\sim 10^{35} - 10^{38}$ ergs s^{-1}. The main radiative process in the atmosphere is free–free emission/absorption, and the spectral shape can be essentially described as a superposition of planckians plus an high–energy Compton tail. ZS's solutions and AW's spectral models are characterized by two parameters: the accretion luminosity L_∞ (or, equivalently, the accretion rate) and the column density y_0 corresponding to the penetration range of incoming protons in the NS atmosphere.

However, as it was recently shown by Turolla *et al.* (1994, paper I), this picture is not necessarily complete. These authors re–examined the issue of the thermal and radiative properties of static atmospheres around accreting NSs, and pointed out that, beyond a critical value of the accretion luminosity $L_{cr} \approx 10^{36}$ erg/s, a new class of much hotter equilibrium solutions exist, together with the "cold" à la Zel'dovich & Shakura ones (see figure 7.1). The existence of two states has a strict analogy with what has been already found in black hole accretion (see Chapter 5 and references therein), and, also in the NS case,

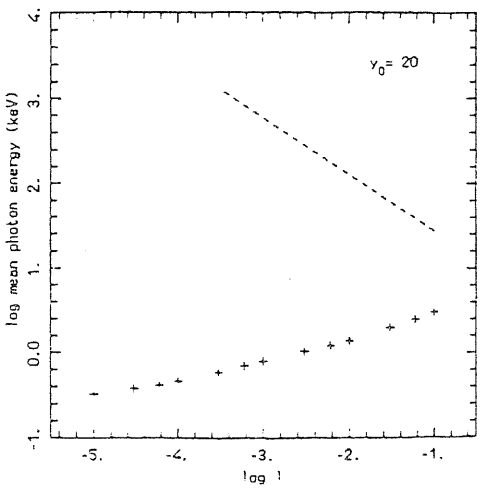

Figure 7.1: *Mean energy of the outgoing photons vs. total emitted luminosity for* $y_0 = 20\,\mathrm{g\,cm^{-2}}$; *crosses refer to "cold" models. Dashed line represents the lower limit for the existence of "hot" solutions. Taken from Turolla et al. (1994).*

is related to the different role thermal and non–thermal processes may play in exchanging energy between photons and electrons in the atmosphere. In the "cold" state (as in ZS) the energy released by accretion is radiated away essentially via bremsstrahlung and the emission is typically peaked in the X–rays. In the "hot" state, where Compton scattering dominates (see also Burger & Katz 1980), owing to the balance between Compton heating and cooling the gas temperature is very close to the radiation temperature and both can be as high as $10^9 - 10^{10}$ K.

From the observational point of view, the coexistence of two branches of solutions for the same values of the parameters is particularly appealing: in fact, the possibility to drive on–off transitions between the two states could give rise to rapid transient phaenomena in

hard X–rays of potential great astrophysical interest.

However, in the simplified analysis presented in paper I, "hot solutions" were found solving the frequency integrated transfer problem. The lack of any information about the angular and frequency dependence of the radiation field made impossible to evaluate the photon–photon pair production, which was nevertheless recognized to be potentially important, and led to introduce rather drastic assumptions in the calculation of the Compton energy exchange rate. In the attempt to overcome some of these limitations and to shed light on the physical relevance of "hot" solutions, we have recently reconsidered this issue (see Zane, Turolla & Treves 1997a,b), using the characteristic code to investigate the spectral properties.

Moreover, as previously stated, the pioneering investigations by ZS and AW are restricted to the high luminosity tail ($L \gtrsim 10^{34}$ ergs s^{-1}) of the "cold" branch. This is because these authors were mainly interested to model the spectral properties of X–ray binaries, and in this case most of the observed sources have $L \gtrsim 10^{34}$ ergs s^{-1}. Much fainter sources may, nevertheless, exist. Most of the $\sim$ 600 known pulsars are single, located in the Galactic disk, and are probably born in the core collapse of massive ($M \gtrsim 8 M_{\odot}$) stars following a supernova explosion (see e.g. Phinney & Kulkarni 1994 for a review). The estimated rate of SN events leading to the formation of a NS is $\approx 10^{-2}$ yr^{-1} at present (see e.g. Narayan & Ostriker 1990), therefore a constant birthrate implies that $\approx 10^{8}$ NSs should be present in the Galaxy, assuming the Galaxy to be $\sim$ 10 Gyr old. This value is, however, very uncertain, and represents a lower limit on the Galactic population of NSs since in the early

phases of the galactic evolution both the star formation rate and the fraction of massive stars may have been higher. Nucleosynthesis constraints on Galactic chemical evolution require a total number as high as 10^9 (Arnett, Schramm & Truran 1989, see also Blaes & Madau 1993 for a discussion). Newly born NSs are expected to have large magnetic fields ($B \sim 10^{12}$ G), short periods ($P \lesssim 0.1$ s) and show up as radio pulsars. The duration of the pulsar phase can be roughly estimated to be of order of $t_{dyn} \sim P/\dot{P} \approx 10^7$ yr, so the present total number of active pulsars is $\approx 10^5$ which is only a very tiny fraction of the estimated number of Galactic NSs. During the NS evolution, neutrino cooling and emission of thermal radiation bring the star temperature from 10^{11} to 10^5 K in about 10^8 yr. In this scenario, old, isolated NSs which have evolved beyond the pulsar phase are expected to be cold objects, dead stars pretty close to be perfectly invisible.

There is however the possibility that *a faint light* may shine *in the graveyard* (Wang 1996). In fact, as it was suggested long ago in a pioneering paper by Ostriker, Rees, & Silk (1970), old, isolated NSs (ONSs) no longer active as pulsars may accrete the interstellar medium and show up as weak, extreme UV/soft X–ray sources. If our present understanding of the NSs birth rate is not grossly wrong, the expected spatial density of ONSs, assuming that they are a disk population, is $\approx 10^{-4} N_8$ pc^{-3}, which implies that, on average, ONSs are ~ 15 pc apart. This figure makes ONSs rather domestic objects, much closer to the Sun than other classes of NSs: the closest pulsar, PSR 0950+08, is about 10 times further away, and the nearest LMXB is at about ~ 100 times that distance. Given the large number of Galactic ONSs and their relative proximity, the observation of isolated accreting NSs

may be already within reach and the capabilities of present instrumentation on board UV and X–ray satellites like ROSAT and EUVE, make now possible the observation of such low luminosity sources (e.g. Treves & Colpi 1991, Blaes & Madau 1993, Zane *et al.* 1995, 1996b, Zane, Turolla & Treves, 1996). This fact motived our interest in reconsider ZS's and AW's solutions, addressing the problem of the emitted spectrum for $L \lesssim 10^{34}$ ergs s^{-1}.

In this thesis we report our results relative to both "cold" and "hot" states. The former regime is discussed in this Chapter, while results relative to the "hot" branch will be presented in Chapter 8. As far as the "cold" regime is concerned, results have been cross–checked using two different approaches for the solution of the transfer problem. First, by using a method based on the solution of the first two PSTF moments equations, we computed a series of models extending ZS's results and performing a systematic investigation of the low luminosities regime ($4 \times 10^{-8} < \ell < 10^{-3}$). These solutions have been published in Zampieri *et al.* (1995), and have been derived using the Eddington approximation. The same results are then reproduced by using a simplified, plane parallel version of the characteristic code (see Chapter 4, Zane *et al.* 1996a), an approach that allows to avoid all assumptions about the closure condition.

Physical units are used throughout, $R = rr_g$ is the radial Schwarzschild coordinate in cgs, and M_* is the NS's mass.

7.1 X–ray Spectra from Neutron Stars Accreting at Low rates

We consider a non–rotating, unmagnetized neutron star which undergoes spherical accretion and is surrounded by a spherical, static atmosphere; the envelope material is assumed to be pure hydrogen. As the accretion flow penetrates into the atmosphere, protons are decelerated by Coulomb collisions and/or plasma interactions, their bulk kinetic energy is transferred to electrons, and is finally converted into electromagnetic radiation via free–free emission. The input physics of our model essentially coincides with that used in previous studies on this subject (see ZS, AW). A detailed modelling of the interactions between the impinging flow and the static envelope is exceedingly complicated (see e.g. Bildsten, Salpeter & Wasserman 1992), also because a collisionless, standing shock can form, as originally suggested by Shapiro & Salpeter (1973). Following both ZS and AW (see also Paper I), we circumvent this problem assuming that the proton stopping length is a free parameter of our model, together with the total luminosity L_∞, measured by an observer at infinity. Denoting by ϱ the gas density, the column density of the atmospheric material is $y = \int_R^\infty \varrho \, dR$; the value y_0 corresponding to the proton stopping length was estimated by ZS to be in the range $5 \lesssim y_0 \lesssim 30\,\mathrm{g\,cm^{-2}}$ when Coulomb collisions are dominant. As it was shown in Paper I, no significant expansion occurs in both "cold" and "hot" envelopes, so in all formulas the radial coordinate R can be assumed to be a constant, equal to the neutron star radius R_*. The heat injected per unit time and mass in the envelope is calculated using the expression for the energy loss rate due to Coulomb collisions of super–thermal protons

(see Bildsten *et al.*),

$$W_h = \begin{cases} \dfrac{L_\infty}{8\pi R_*^2 y_0 y_G} \dfrac{1 + v_{th}^2/v_i^2}{[1 - (1 - v_{th}^4/v_i^4)(y/y_0)]^{1/2}} & \text{if } y \le y_0 \,; \\ \\ 0 & \text{if } y > y_0 \,. \end{cases} \tag{7.1}$$

where $v_i^2 = c^2(1 - L_\infty/L_{Edd})/3$ is the "modified" free–fall velocity, $v_{th}^2 = 3kT/m_p$ is the proton thermal velocity, $y_G = (1 - 2GM_*/c^2R_*)^{1/2}$ is the gravitational redshift factor in the Schwarzschild spacetime. We note that, owing to the gravitational redshift, the total luminosity seen by a distant observer, L_∞, is related to the local luminosity at the top of the atmosphere by $L_\infty = y_G^2 L(0)$.

The run of pressure P, temperature T, monochromatic radiation energy density w_ν^0 and flux cw_ν^1 (both measured by the local observer) are obtained solving the hydrostatic and the energy balance for a completely ionized, perfect hydrogen gas (ZS, Paper I) coupled to the first two frequency–dependent transfer moment equations in the Eddington approximation (AW; Nobili, Turolla & Zampieri 1993, here NTZ93). By treating Compton scattering in the Kompaneets approximation, these equations can be written as

$$\frac{dP}{dy} = \frac{GM_*}{y_G^2 R_*^2}\left(1 - \frac{\kappa_1}{\kappa_{es}}\frac{y_G L}{L_{Edd}}\right) \tag{7.2}$$

$$\frac{W}{c} = \kappa_P\left(aT^4 - \frac{\kappa_0}{\kappa_P}w^0\right) + 4\kappa_{es}w^0\frac{KT}{m_e c^2}\left(1 - \frac{T_\gamma}{T}\right) - \frac{c\kappa_{es}}{8\pi m_e}\int\left(\frac{w_\nu^0}{\nu}\right)^2 d\nu \tag{7.3}$$

$$\frac{w_\nu^1}{w_\nu^0}\left[\frac{\partial \ln w_\nu^1}{\partial y} - \frac{GM_*}{c^2\varrho y_G^2 R_*^2}\left(1 - \frac{\partial \ln w_\nu^1}{\partial \ln \nu}\right) - \frac{2}{\varrho R_*}\right] = -\frac{s_\nu^0}{y_G w_\nu^0 \varrho} \tag{7.4}$$

$$\frac{1}{3}\frac{\partial \ln w_\nu^0}{\partial y} - \frac{GM_*}{c^2\varrho y_G^2 R_*^2}\left(1 - \frac{1}{3}\frac{\partial \ln w_\nu^0}{\partial \ln \nu}\right) = -\frac{s_\nu^1}{y_G w_\nu^0 \varrho}. \tag{7.5}$$

Here $w^0 = \int w_\nu^0\, d\nu$, $L = 4\pi R_*^2 c \int w_\nu^1\, d\nu$, κ_P, κ_0 and κ_1 are the Planck, absorption and

flux mean opacities, and the T_γ is the radiation temperature, introduced in Chapter 5. $W = W_h - W_c$ represents that part of the injected heat, W_h, which is effectively converted into electromagnetic radiation within the atmosphere. W_c mimics the possible presence of other forms of energy transport (like convection and electron conduction) which are not treated in detail here (see AW for comparison); the actual form of W_c is discussed later on. The first two moments of the source function, s^0_ν and s^1_ν, account for the exchange of energy and momentum between electrons and photons and, for the radiative processes we are considering, bremsstrahlung and electron scattering, they can be cast in the form (NTZ93)

$$\begin{aligned} s^0_\nu &= \kappa_{es}\varrho w^0_\nu \left\{ \frac{kT}{m_e c^2}\left[\frac{\partial^2 \ln w^0_\nu}{\partial \ln \nu^2} + \left(\frac{\partial \ln w^0_\nu}{\partial \ln \nu} + \frac{h\nu}{kT} - 3 \right) \frac{\partial \ln w^0_\nu}{\partial \ln \nu} \right.\right. \\ &+ \left.\left. \frac{h\nu}{kT} + \frac{c^3 w^0_\nu}{4\pi kT\nu^2}\left(\frac{\partial \ln w^0_\nu}{\partial \ln \nu} - 1 \right) \right] + \frac{\kappa_{ff}}{\kappa_{es}}\left(\frac{4\pi B_\nu(T)}{w^0_\nu c} - 1 \right) \right\} \end{aligned} \tag{7.6}$$

$$s^1_\nu = -\left(\kappa_{es} + \kappa_{ff}\right)\varrho w^1_\nu \,, \tag{7.7}$$

where $B_\nu(T)$ is the Planck function. The free–free opacity for a completely ionized hydrogen gas is

$$\kappa_{ff} = 1.318 \times 10^{56} \varrho T^{-1/2} \frac{1 - e^{-h\nu/kT}}{\nu^3} \bar{g}(\nu, T)\, \mathrm{cm}^2\, \mathrm{g}^{-1} \,. \tag{7.8}$$

In these solutions electrons are not relativistic, so that we used a functional fit to Karzas & Latter's (1961) tables for the velocity–averaged Gaunt factor, neglecting high–temperature corrections (see section 3.1). Since equations (7.4) and (7.5) define a second order elliptic operator, conditions must be prescribed on the entire boundary of the integration domain

and their form is discussed in NTZ93. In particular, we assume that diffusion holds in the deeper layers where LTE is certainly attained and this automatically fixes the luminosity at the inner boundary, L_{in}. If all the energy is supplied by accretion, the total radiative flux that crosses the inner boundary must equal the heat transported inward by non–radiative processes, that is to say

$$W_c = \frac{L_{in}}{8\pi R_*^2 y_0 y_G} \frac{1 + v_{th}^2/v_i^2}{[1 - (1 - v_{th}^4/v_i^4)(y/y_0)]^{1/2}} \qquad 0 \le y \le y_{in}\,. \tag{7.9}$$

Although the total radiation energy density and luminosity are just the integrals of w_ν^0 and $4\pi R_*^2 c w_\nu^1$ over frequency, we found numerically more convenient to derive them from the first two gray moment equations. In the Eddington approximation they are

$$\frac{dL}{dy} = -\frac{4\pi R_*^2 W}{y_G} \tag{7.10}$$

$$\frac{1}{3}\frac{dw^0}{dy} = \kappa_1 \frac{L}{4\pi R_*^2 c y_G}\,. \tag{7.11}$$

Equation (7.10) gives trivially

$$L = \begin{cases} \dfrac{L_\infty}{y_G^2} - \left(\dfrac{L_\infty}{y_G^2} - L_{in}\right) \dfrac{1 - [1 - (1 - v_{th}^4/v_i^4)(y/y_0)]^{1/2}}{1 - v_{th}^2/v_i^2} & \text{if } y \le y_0\,; \\ \\ L_{in} & \text{if } y > y_0\,. \end{cases} \tag{7.12}$$

with the condition $L(y_{in}) = L_{in}$, while equation (7.11) is integrated numerically along with the system (7.2)–(7.5), imposing $w^0(0) = 2w^1(0)$; pressure vanishes at the top of the atmosphere, $P(0) = 0$.

7.2 Results

Equations (7.2)–(7.5) and (7.11) were solved numerically by means of a finite differences relaxation scheme (NTZ93) on a logarithmic grid of 50 frequency bins × 100 depth zones. The adimensional frequency $x = h\nu/kT_*$ was used, $T_* = T(y_{in})$, and the integration range was typically $-0.7 < \log x < 1.1$, $-7.6 < \log y < \log y_{in}$, with y_{in} marginally smaller than y_0. A typical run required $\sim$ 15 minutes of CPU time on an IBM RISK/6000. Two sets of models were computed, both with $R_* = 12.4$ km, $M_* = 1.4 M_\odot$: $y_0 = 20$ g cm^{-2} and luminosities in the range $4 \times 10^{-8} \leq L_\infty/L_{Edd} \leq 0.2$, $y_0 = 5$ g cm^{-2} and $10^{-7} \leq L_\infty/L_{Edd} \leq 10^{-5}$. Our numerical method should guarantee a fractional accuracy better than 1% on all the variables. As a further check, the total luminosity, given by equation (7.12), was compared with the numerical integral of w_ν^1 over the frequency mesh at each depth: agreement was always better than 10%. We have also verified that our solutions with $L_\infty \gtrsim 10^{-2} L_{Edd}$ reproduce almost exactly those computed by AW. In the low–luminosity range, which we are mainly interested in, particular care must be used to handle properly the absorption and flux mean opacities, since the envelope thermal balance depends entirely on the free–free integrated source term and the radiation spectrum becomes very nearly Planckian in the deeper layers.

Results are summarized in figures 7.2, 7.3 and 7.4, where the emergent spectra and the temperature profiles are plotted for different values of L_∞. In all these models it is $y_0 = 20$ g cm^{-2}; solutions with $y_0 = 5$ g cm^{-2} show the same qualitative behaviour. A quite unexpected feature emerging from figures 7.2 and 7.3 is that the spectral shape deviates more

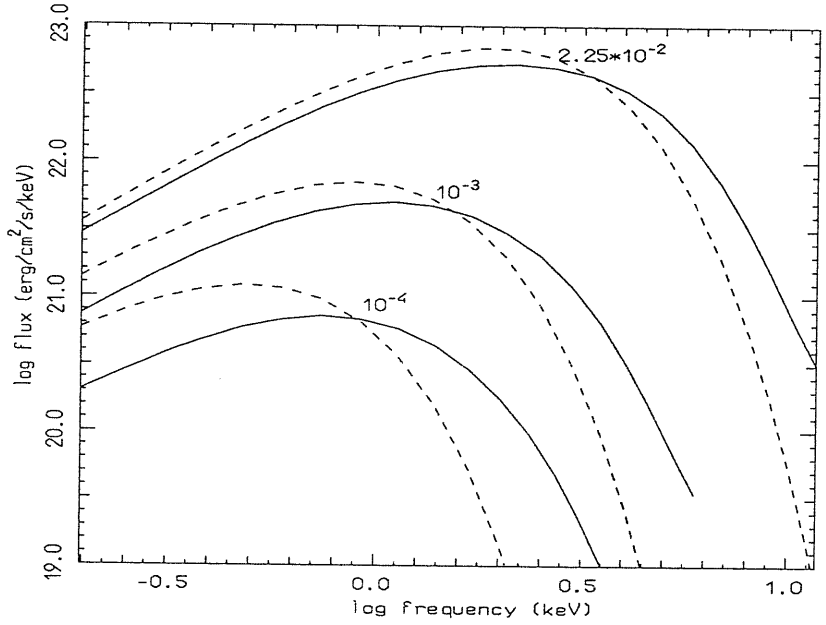

Figure 7.2: *Emergent spectra for* $L_\infty = 2.25 \times 10^{-2}, 10^{-3}, 10^{-4}\, L_{Edd}$ *(full lines), together with the corresponding blackbody spectra at the neutron star effective temperature (dashed lines).*

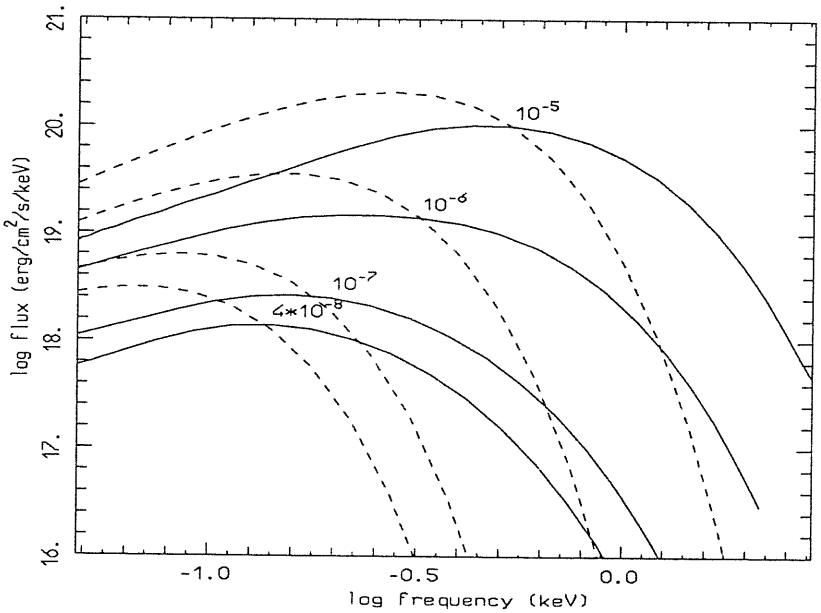

Figure 7.3: *Same as in figure 7.2 for models with* $L_\infty = 10^{-5}, 10^{-6}, 10^{-7}, 4 \times 10^{-8}\, L_{Edd}$.

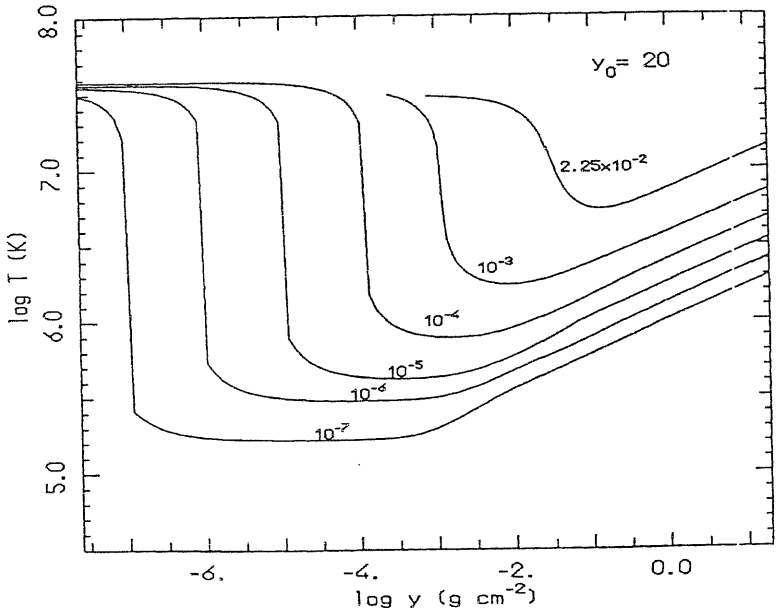

Figure 7.4: *Temperature vs. column density for different values of* L_∞/L_{Edd}.

and more from a blackbody as L_∞ decreases. The model with $L_\infty = 2.25 \times 10^{-2} L_{Edd}$ is, in fact, quite Planckian in shape (see also AW), showing only a moderate hard excess. On the contrary, solutions with $L_\infty < 10^{-4} L_{Edd}$ are characterized by a very broad maximum and by a slow decay at high energies. Comptonization is relatively important for $L \gtrsim 10^{-2} L_{Edd}$, similarly to what happens in X–ray burster atmospheres (see e.g. London, Taam, & Howard 1986). For less luminous models, however, non–conservative scatterings play essentially no role in the formation of the spectrum, as it should be expected since the temperature, and hence the Compton parameter, becomes lower. As can be seen from figure 7.4, the temperature profile is nearly adiabatic in the inner layers where the gas is optically thick to true emission–absorption at all frequencies; for $L \lesssim 10^{-5} L_{Edd}$ an intermediate, isothermal region is present. The sudden increase of T in the external layers is due to the heating

produced by the incoming protons, balanced mainly by Compton cooling at low densities. The temperature "shock" moves at very low values of the column density and is nearly out of our depth mesh for $L_\infty = 10^{-7} L_{Edd}$.

As it will be discussed in Chapter 9, the hard excess present in our low–luminosity spectra has some important consequences as far as predictions on the observability of ONSs are concerned. In this respect, it is very important to compare the actual emerging spectrum with the blackbody at the neutron star effective temperature, $B_\nu(T_{eff})$. $T_{eff} = [L_\infty/(4\pi R_*^2 \sigma)]^{1/4}$, which is usually assumed to be the emitted spectrum (see e.g. Treves & Colpi 1991, Blaes & Madau 1993). It is apparent from figure 7.3 that model spectra with $L \lesssim 10^{-5} L_{Edd}$ are substantially harder than the blackbody at the star effective temperature. The spectral hardening can be quantified introducing a hardening ratio

$$f = \frac{T_\gamma}{T_\gamma[B_\nu(T_{eff})]}, \tag{7.13}$$

where, from the definition of T_γ (see equation 5.6), it is $T_\gamma[B_\nu(T_{eff})] = 0.96 T_{eff}$. This differs from the usual definition, $f = T_{col}/T_{eff}$, where T_{col} is the color temperature, because our spectra are not always well fitted by a blackbody. For $y_0 = 20$ g cm^{-2}, f steadily increases from ~ 1.5 (value typical of X–ray bursters in the static phase), for $L \sim 10^{-2} - 10^{-3} L_{Edd}$, up to ~ 2.5 for $L \sim 10^{-6} - 10^{-7} L_{Edd}$ (see table 7.1).

Table 7.1: **Characteristic Parameters for Selected Models**

$\frac{L_\infty}{L_{Edd}}$	T_γ (keV)	$\frac{F_{>0.1}}{F^{bb}_{>0.1}}$ [a]	γ [b]	γ [c]
2.25×10^{-2}	1.03	1.01	1.40	–
10^{-3}	0.53	1.03	1.56	–
10^{-4}	0.35	1.01	1.88	–
10^{-5}	0.24	1.02	2.21	2.06
10^{-6}	0.15	1.07	2.44	2.31
10^{-7}	0.09	1.34	2.64	2.55

[a] *Ratio of integrated flux to blackbody one above 0.1 keV, for models with* $y_0 = 20\,\mathrm{g\,cm^{-2}}$.

[b] *Hardening ratio, defined in equation (7.13), for models with* $y_0 = 20\,\mathrm{g\,cm^{-2}}$.

[c] *Hardening ratio for models with* $y_0 = 5\,\mathrm{g\,cm^{-2}}$.

7.3 A Different Approach

Results presented in the previous section have been confirmed using the characteristic code: the hydro equations (7.2) and (7.3) have been coupled with the Boltzmann equation and the system solved iteratively, using the same scheme that we introduced to compute the scattering integral. As already discussed, in the "cold" regime the most important radiative process is free–free; Compton cooling plays a role only in increasing the temperature in the outer atmospheric layers. Since typical temperatures are very low, Comptonization is treated by means of the approximated expression (3.25), which is much faster. However, we have already pointed out that in this problem the thermal balance is very delicate and the zone where photons of different energies thermalize strongly depends on integrated quantities, mainly on w^0 and on the absorption mean κ_0. In particular, even using the characteristic code, numerical integration proved more stable if w^0 and L are derived as solution of the first two gray moment equations (7.10) and (7.11). The same approach was used to compute solutions using the PSTF moments equations (section 7.1, Zampieri *et al.* 1995), with the difference that in the present scheme the gray moment equations can be solved exactly, relaxing the Eddington approximation. The original form of equation (7.11) is in fact

$$\frac{dK}{dy} = \kappa_1 \frac{L}{16\pi^2 R_*^2 c y_G}, \tag{7.14}$$

and this equation can be integrated by fixing the luminosity L_∞ of the model, evaluating numerically the ratio K/H, and deriving the correct boundary condition for the radiation pressure at $\tau_{es} = 0$. Strictly speaking, in fact, the free streaming condition $w^0(0) = 2w^1(0)$ that we previously used, only holds for a pure scattering atmosphere (see Chandrasekhar

1960); limb darkening effects were not taken into account by using the PSTF expansion. Once K is known, the quantity $w^0 = J/(4\pi)$, needed in the energy balance equation, can be immediately evaluated by computing the Eddington factor K/J, at each scattering depth, from the specific intensity

Here we present the model with $\ell = 10^{-4}$. The solution has been computed using a spectral window $x_{min} = 0.1$, $x_{max} = 10$ centered around a normalization temperature $\log T_* = 6.6$; $L = 30$ frequency points have been used. As we already pointed out, in these solutions the static atmosphere is geometrically thin; the problem is approached in plane–parallel symmetry by using as independent variable the scattering optical depth $\tau_{es} = 0.4y$ and imposing the standard Sommerfeld radiative boundary condition for a non–illuminated atmosphere, $f = 0$, at $\tau_{es} = 0$. Outgoing trajectories are integrated fixing the boundary condition $f = B_\nu(T)/E^3$ at the inner boundary, where LTE is reached. The angular resolution is provided by $N_1 = N_2 = 15$ trajectories and the transfer equation is solved in the range $-8 < \log(\tau_{es}) < 0.9$ using $M = 100$ grid points. The resulting mean intensity is plotted in figure 7.5. Figures 7.6 and 7.7 show the emergent spectrum and the temperature profile together with the results obtained solving the moments equations (dashed lines). As it can be seen, the agreement both in the spectral shape and the temperature profile is very good, showing that the approximated solution of the transfer equation with two moments is rather accurate. To obtain this model, with a fractional accuracy better than 2×10^{-2}, 14 iterations were required, with a total CPU time of about 3 minutes on an alpha DEC–3000. Agreement between the gray mean intensity, derived as the double integral of f, and the solution of the second gray moment equation is always better than few parts in thousand.

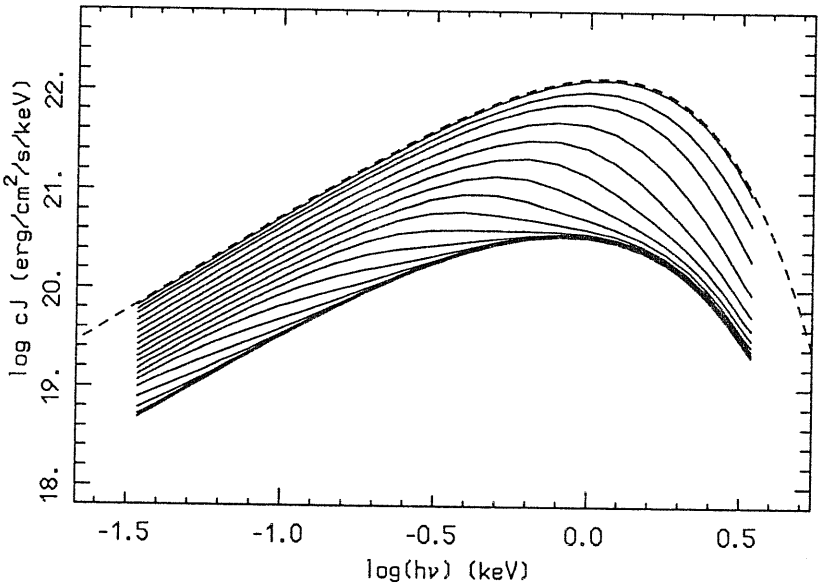

Figure 7.5: *Monochromatic mean intensity at different scattering depths (full lines) for a "cold", static, plane–parallel atmosphere around a neutron star with* $\ell = 10^{-4}$. *The blackbody function at* $T(\tau_{es}^{in})$, τ_{es}^{in} *is the inner boundary in this model, is also drawn for comparison (dashed line).*

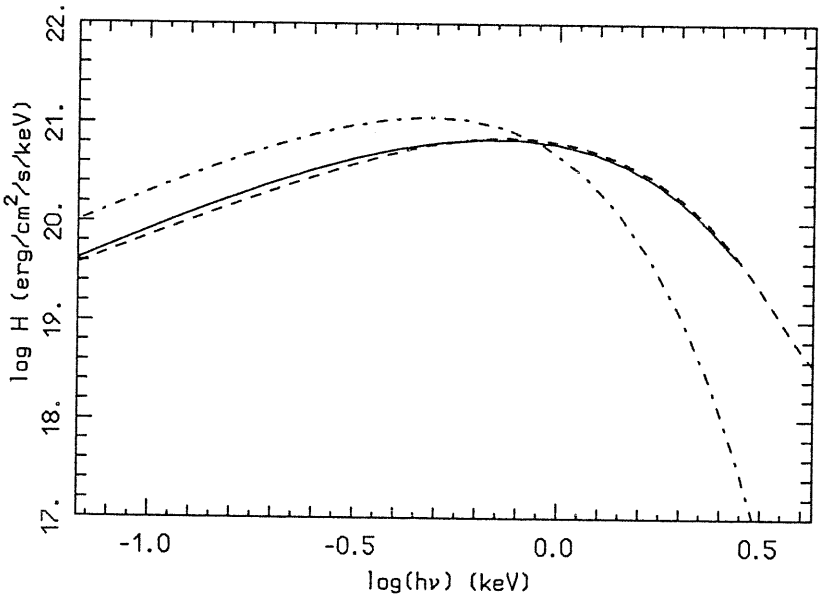

Figure 7.6: *The emergent spectrum for the model in figure 7.5 (full line) compared with the blackbody at the neutron star effective temperature (dash–dotted line) and with the solution obtained by solving the PSTF moments equations (section 7.2; Zampieri et al. 1995, dashed line).*

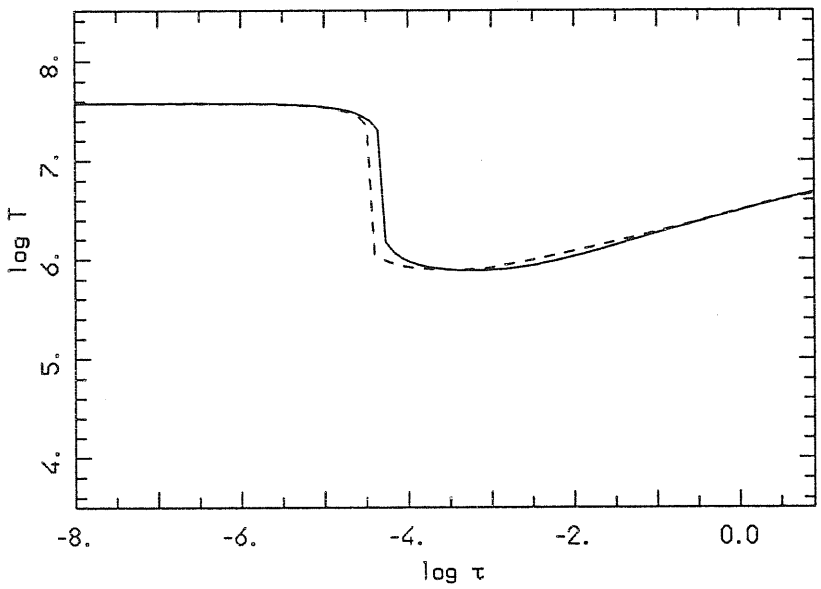

Figure 7.7: *The gas temperature profile for the model in figure 7.5 (full line), compared with that one found by solving the PSTF moments equations (section 7.2; Zampieri et al. 1995, dashed line).*

7.4 Discussion

The significant deviation of low–luminosity spectra from a Planckian equilibrium distribution could appear unexpected, since radiation is in LTE in a medium where the scattering depth is always much less than the absorption one. The source function should be Planckian and the emergent spectrum, formed at the thermal photosphere, should coincide with $B_\nu(T_{eff})$. However, if the atmosphere develops smooth temperature and density gradients in layers where the medium becomes optically thin to free–free, the differential nature of the absorption opacity plays an important role. High–frequency photons decouple in the deeper, hotter layers and then propagate freely to infinity, contributing to the high–energy part of the emergent spectral flux. At large enough frequencies, the observed shape of the spectrum turns out to be a superposition of planckians at different temperatures. This re-

sult resembles closely that of standard accretion disks, where the emergent spectrum shows a broad plateau due to the combined, thermal emission of rings at different temperatures.

Our present result that low–luminosity spectra are harder than a blackbody is consistent with the previous finding by Romani (1987), who computed model atmospheres for cooling neutron stars. Although he considered a quite different physical scenario, an atmosphere in radiative energy equilibrium illuminated from below, the free–free opacity in his cool, He models ($T_{eff} \sim 3 \times 10^5$ K) acts much in the same way as in our low luminosity solutions, producing a hardening of the spectrum.

Both in Romani's and in our analysis the effects of the neutron star magnetic field were ignored. It can be easily shown that, for temperatures and densities in the photospheric region typical of the model presented in section 7.3, the cyclotron emission is lower than the free-free emission if $B \lesssim 10^9$ G (see e.g. Schmid–Burgk, 1978). However, because of the many uncertainties in the physics governing the magnetic field evolution, the determination of a reasonable order of magnitude for the ONSs B–field still remain an open issue. The discovery of a number of weak–field millisecond pulsars, recycled during a phase of intense accretion in a low mass binary system (Alpar et al. 1982), provides some probes for field decay in binaries. Despite that, at present no clear observational evidence exists for a decay over the pulsar phase in the case of solitary objects (see Srinivasan 1997, and references therein, for a recent review). This important topic will be discussed in details in Chapter 9. For the moment, we only outline that *if the field decay occurs* leaving a relic B–field as low as $\approx 10^9$ G, all radiative effects of the magnetic field can be neglected. The only role played by a non–vanishing B–field is to channel the accretion flow along the magnetic lines, concentrating the emission onto two polar caps. If this is the correct scenario, models

presented here can be assumed to describe correctly the emitted spectrum from old neutron stars accreting the interstellar medium (apart a rescaling in the total luminosity due to the different size of the emitting area, see Chapter 9).

Finally we note that the assumption of a pure hydrogen chemical composition used here, is not entirely ad hoc. In fact, contrary to what happens in equilibrium atmospheres, such as those considered by Romani (1987) and Miller (1992) who allowed for different compositions, it is likely that metals are destroyed in the accretion flow (Bildsten, Salpeter & Wasserman 1992), leaving just a hydrogen envelope.

As we already stressed, a motivation for studying the spectral properties of X–ray radiation coming from neutron stars accreting at low rates, stems from the possible detection of isolated objects fed by the interstellar gas. Their expected luminosities, $\sim 10^{31}$ ergs s^{-1}, could be within reach of satellites like Einstein and ROSAT (see Treves & Colpi 1991; Blaes & Madau 1993; Colpi, Campana & Treves 1993; Madau & Blaes 1994) and the knowledge of the emitted spectrum is fundamental in estimating their observability as X–ray sources. This issue will be discussed in detail in Chapter 9. Here we point out that the fact that synthetic spectra are significantly harder than the blackbody at T_{eff}, may indeed increase the chances of detection with respect to previous estimates. In table 7.1 we have listed the ratios of the computed flux above 0.1 keV to the blackbody one for various luminosities; the threshold of 0.1 keV was suggested by the sensitivity of ROSAT. The solutions with $L = 10^{-7}$ and $10^{-5}\, L_{Edd}$ can be taken as representative of the typical luminosities expected from ONSs embedded in the average ISM or in Giant Molecular Clouds (see Colpi, Campana & Treves 1993). As can be seen from the table, the ratio becomes larger than unity and the flux above 0.1 keV is from $\sim$ 10% to $\sim$ 40% larger than the blackbody one for

$10^{32} \gtrsim L \gtrsim 10^{31}$ ergs s^{-1}.

The present models could be relevant also to soft X–ray transients in quiescence, such as Aql X–1 (Verbunt *et al.* 1994), or in connection with low–luminosity globular cluster X–ray sources which emit a luminosity $\sim 10^{-4}\, L_{Edd}$ (see e.g. Hertz, Grindlay, & Bailyn 1993 and references therein). These still mysterious objects could be either accreting white dwarfs (e.g. cataclysmic variables) or neutron stars in binary systems. Their spectrum, which is still poorly known, could be compared with the results of these models, and deviations from a blackbody may be an important clue in discriminating their physical nature.

8 Hot Atmospheres Around Accreting NS: A Possible Source For Hard X–ray Emission

8.1 Introduction

In this Chapter we focus on the "hot" configurations presented in paper I by Turolla *et al.* (1994). These equilibrium states coexist with the "cold" ones at large enough values of the accretion rate, and the presence of two possible regimes has a simple interpretation in terms of the relative efficiency of Compton scattering and free-free emission–absorption. If "hot" states are indeed accessible, the coexistence of the two branches is not important only "per se", but also for applications to rapid transient phaenomena in hard X–rays. The transition between "cold" and "hot" regimes, even at luminosities where the two solutions are rather different, may be expected in a time–dependent scenario and the onset of the "hot" state could provide an efficient mechanism to produce emission from NSs in the MeV range.

However, steaming from the original analysis presented in paper I, a number of issues still

demands to be clarified. First of all, as previously stated, the existence of the second branch of solutions, in addition to the ZS, "cold" one, was found in the framework of a frequency–integrated, stationary analysis and the spectral and stability properties of these states have never been investigated. In particular, the radiation temperature, a key ingredient in evaluating the Compton energy exchange rate, was derived in the gray model from a phaenomenological equation and not from a self–consistent calculation of the radiation field. Second, "hot" solutions were computed within the same physical scenario of "cold" ones, which is basically that one of ZS, and in a more realistic description the input physics needs to be upgraded if relativistic temperatures are reached. In paper I, pair processes were not taken into account. However, since T_γ is typically of order few hundreds keV, we expect a large pair production, mainly via interactions between high and low energy photons. These reasons motivated our interest in readdressing this issue, in the attempt to overcome some of the previous limitations and to shed light on the properties of "hot" solutions.

A complete answer demands the solution of the full time, angle and frequency–dependent radiation hydrodynamical problem in a high–temperature plasma, including pair processes and a correct treatment of Compton scattering in the relativistic regime. From the numerical point of view, this is a challenging and formidable task, at present beyond the scope of our investigation. In order to get some physical insight without resorting to a full time–dependent calculation, we consider the stationary case and approach the problem is a simpler way, analyzing the effects of different processes separately. As first step, we compute the radiation field neglecting pairs, but solving the angle and frequency–dependent transfer equation coupled to the hydrostatic and energy balance and using a detailed treatment of

true emission–absorption and Comptonization in the hot plasma (section 8.1). This is done by using the characteristic code introduced in Chapter 4 (Zane *et al.* 1996a). The resulting specific intensity is then used to solve the detailed balance equation and to estimate the number density of pairs, n_+, produced by photon–photon interactions. The numerical code described in Chapter 4 was generalized to include in the source term pair production–annihilation and, self–consistently, $e^+ - e^+$, $e^- - e^+$, $e^+ - p$ bremsstrahlung.

Although not fully self-consistent, this approach is sufficient to derive some insight on the physical properties of "hot" atmospheres. Although, as we checked a posteriori, pair production does not play an important role as far as the transfer problem is concerned, it can have some important consequences on the stability of these states. In fact, we found that a large $e^+ - e^-$ pair production is expected in the external atmospheric layers, where positron and proton number densities become of the same order. As a consequence, the scattering opacity increases lowering the Eddington limit. This, in turn, suggests that, for large enough values of the accretion luminosity, "hot" solutions can undergo a dynamical instability with respect to the onset of a radiatively–driven wind, ultimately producing a rapid expulsion of the envelope. In the last section of this Chapter we discuss this possibility together with astrophysical applications in the context of hard X–ray transient phenomena.

8.2 The Model

In this section we briefly outline some general properties of "hot" models, referring to previous works (ZS; AW; paper I; Zampieri *et al.* 1995) for all details about the input physics, and introduce our radiative transfer calculations. In particular, the mathematical

structure of the problem is the same as in "cold" models, and it has been reported in Chapter 7. Here we only discuss the differences in the basic equations that arise to properly account for radiative processes in high energy regimes. As discussed in paper I, even in the "hot" case solutions show no significant envelope expansion, so the radial coordinate can be safely assumed equal to the star radius and the atmospheric structure is solved in plane–parallel geometry. The pressure and luminosity profiles are still obtained from equations (7.2), (7.12), and the temperature by the solution of the energy balance equation. Neglecting pair production, this equation can be schematically written as (see 7.3)

$$\frac{W}{c} = \kappa_P \left(aT^4 - \frac{\kappa_0}{\kappa_P} w^0 \right) + (\Gamma - \Lambda)_C \,, \tag{8.1}$$

where $(\Gamma - \Lambda)_C$ is the Compton energy exchange rate. As discussed in Chapter 7, the effective heating W represents the fraction of W_h (expression 7.1) which is converted into electromagnetic radiation within the atmosphere; W coincides with W_h if no energy is injected at the inner boundary, that is if $L_{in} = 0$. Since at large depths the radiation field becomes more and more isotropic, L_{in} is indeed small, although in a realistic situation it is not exactly zero. On the other hand, the thermal structure of both the "cold" and "hot" solutions presented in paper I proved not sensitive to the assumed value of the luminosity at the bottom of the atmosphere, provided it is not too large compared with L_∞. In particular, "hot" atmospheres exhibit a rather sharp drop in the gas temperature which separates two distinct regions characterized by different thermal properties (see figure 8.1). In the external layers, where the bulk of the luminosity is produced, the energy released by accretion is radiated away via Compton cooling, while in the deeper, denser layers LTE is attained and the temperature profile is mainly determined by bremsstrahlung equilibrium. For these solutions L_{in} also coincides with the value of the radiative flux at the top of the

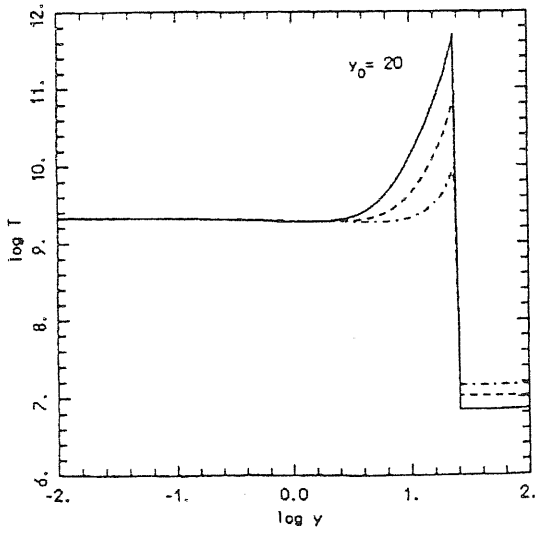

Figure 8.1: *Temperature vs. column density of "hot" solutions for* $\ell_\infty = 10^{-3}$ *(solid line),* $\ell_\infty = 2 \times 10^{-2}$ *(dashed line), and* $\ell_\infty = 7 \times 10^{-2}$ *(dashed-dotted line); here* $y_0 = 20\ g\ cm^{-2}$. *Taken from Turolla et al. (1994).*

cold region.

There are two important points concerning the "hot" models that were not thoroughly discussed in paper I and deserves further analysis. Both of them concern the possibility of establishing and maintaining a rather steep temperature gradient between the hot to the cold part of the atmosphere, so that a "hot" solution can indeed set in. First of all we note that the position of the temperature drop is practically unrelated the value of the proton stopping length. Although for $y_0 = 20$ g cm^{-2} (the value we will use here) they practically coincide, we stress that, in general, the value of the scattering depth at which the transition occurs depends only on the relative efficiency of Compton and bremsstrahlung heating–cooling and, as numerical tests show, it is always close to $\tau_{es}^{tr} = 10$ ($y^{tr} = 25$). The presence of a sudden decrease in T can be understood comparing the free–free and Compton thermal times

$$\frac{t_C}{t_{ff}} = \frac{\epsilon_{ff}\,(1 - w^0/aT^4)}{4k|T - T_\gamma|\kappa_{es} w^0/m_e c^2}\,, \tag{8.2}$$

where ϵ_{ff} is the free–free emission. As the scattering depth increases T and T_γ become closer, because non–conservative scatterings tend to establish thermal equilibrium, and w^0 either increases or stays constant. In the hot, effectively thin layers $w^0 \ll aT^4$ and at large enough τ_{es}, where $T \simeq T_\gamma$, the time scale for free–free cooling becomes shorter than the Compton time. The plasma temperature drops until $aT^4 \simeq w^0$ in order for the energy balance to be satisfied and the radiation temperature follows.

The second important point concerns the efficiency of electron conduction at the interface between the hot and cold regions. This effect was not considered in paper I. In order to get a quantitative estimate of the relevance of thermoconduction we compare the energy flux due to conduction, $F_c = \nu_c \varrho dT/dy$, with the radiative flux, $F_r = L/4\pi R^2$. Using the

expression for ν_c given in Zel'dovich, & Raizer (1967) it is

$$\frac{F_c}{F_r} \sim 2.5 \times 10^{-3} \left(\frac{T}{10^9}\right)^{5/2} \left(\frac{L}{L_{Edd}}\right)^{-1} \frac{y^{tr}}{\Delta y} \tag{8.3}$$

where Δy is the width of the transition layer and T is the temperature in the hot region. As the previous equation shows, electron conduction is indeed efficient in transferring heat from the hot to the cold region. However, if a fraction of the luminosity is produced below y^{tr}, $L_{in}/L_{\infty} \sim 0.2 - 0.3$ for $L_{\infty} \sim 0.1 L_{Edd}$, conduction will limit the temperature of the hot region to $\sim 10^9$ K, smear the jump over $\Delta y \sim 2 - 3$ and then cease to be important. The stationary temperature profile will then look quite similar to that discussed by Zel'dovich, & Raizer (1967) in the context of shock waves in a plasma. Although the real profile will deviate from that of paper I (mainly in the absence of the peak at $T \sim 10^{10}$ K, see curve b in figure 8.3, which will be leveled if conduction is taken into account), the emerging picture seems to be substantially unaltered by the inclusion of thermal conduction. This conclusion is reinforced by the result of the frequency–dependent calculation presented here which shows that the temperature profile is nearly isothermal at $T \sim 10^9$ K (see curve a in figure 8.3). It is interesting to point out that the existence of a "hot" equilibrium state can be recovered analytically by solving the energy balance equation in the limit in which Compton cooling dominates and using an approximated expression for the Comptonized radiation spectrum (see Titarchuk 1997, Titarchuk, Lapidus & Muslimov 1997). In the case in which Comptonization is effective and produces a rather flat spectrum with $\alpha \ll 1$ and the scattering depth at the stopping radius exceeds unity it is $T \sim 10^9$ K quite independently on the value of y_0 (Titarchuk, private communication).

Let us now to focus in more detail on "hot" atmospheres. As we discussed, in this picture only a small fraction of the total luminosity ($L_{in}/L_{\infty} \lesssim 0.2 - 0.3$) is produced below

y^{tr}, where the scattering depth is already larger than $\sim$ 10. Bearing this in mind, we can compute the radiation field only for $y < y^{tr}$ with a suitable boundary condition at y^{tr}. The consistency of the computed flux at the boundary with the assumed value of L_{in} will be checked a posteriori. By solving the radiation field by means of the characteristics approach, we are able to derive the full spatial, angular and frequency dependence of the photon occupation number f. We used as boundary conditions $f = 0$ at the top of the atmosphere for incoming rays and a regularity condition ($df/d\tau_{es} = 0$) at the inner boundary for outgoing rays. We refer again to Chapters 3, 4 of this thesis for all computational details about the source term which includes, at this level of description, relativistic $e^- - p$, $e^- - e^-$ bremsstrahlung and Compton scattering. In particular, Compton scattering is treated in its more general form by direct evaluation of the integrals of the Compton scattering kernel. To avoid numerical instabilities which arise when more accurate formulae are used (see e.g. Shestakov, Kershaw, & Prasad 1988), the Kompaneets approximation was retained in the calculation of the Compton energy exchange rate. The resulting monochromatic energy density is shown in figure 8.2 for $L_\infty/L_{Edd} = 7 \times 10^{-2}$, $L_{in} = 0.2L_\infty$ and $y_0 = 20$ g cm^{-2} at different optical depths. The dashed line represents the spectrum observed at infinity, i.e. corrected for the gravitational redshift. This model has been computed solving the transfer equation for 20 values of μ, 25 energies in the range 0.017 MeV $\leq E \leq$ 5 MeV and $10^{-3} \leq \tau_{es} \leq 8$. The considered luminosity is close to the lower limit for the existence of "hot" solutions with $y_0 = 20$ g cm^{-2}, and it can be thought to be well representative of situations where photon energies are large enough to produce pairs, since T_γ is anticorrelated with L_∞ (see paper I). The emergent flux, in fact, is peaked at $\sim$ 500 keV and is characterized by a high–energy tail. The gas and radiation temperatures, together with the correspondent

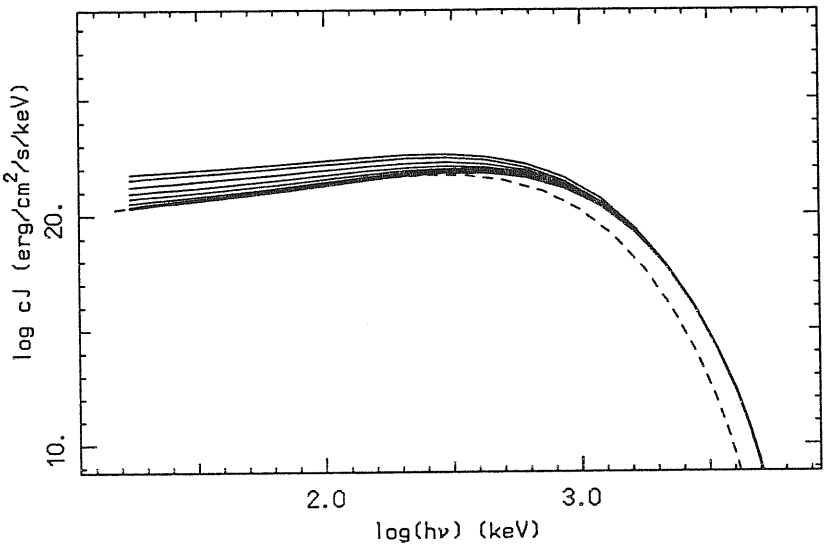

Figure 8.2: *Monochromatic mean intensity for the model* $L_\infty = 7 \times 10^{-2} L_{Edd}$, $y_0 = 20\ g\ cm^{-2}$; *different lines correspond to equally spaced values of* $\log \tau_{es}$ *in the interval* $[-3, 0.9]$. *The emerging redshifted spectrum is also shown (dashed line).*

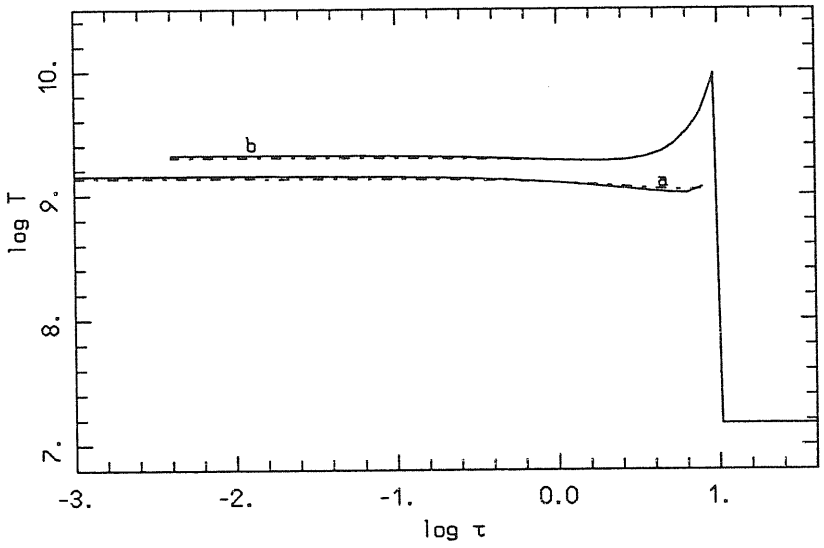

Figure 8.3: *a) The gas temperature (full line) and the radiation temperature (dashed line) for the model of figure 8.2. b) Same results from the frequency-integrated analysis of paper I.*

profiles derived in paper I, are shown in figure 8.3. The lower values of T (about a factor 3) are mainly due to the different calculation of T_γ which enters in the energy equation. Now the radiation temperature is directly evaluated from the mean intensity and not obtained from a phenomenological equation, as in paper I. In the present calculation, the atmosphere appears to be nearly isothermal. In both cases the energy balance is practically obtained equating Compton heating and cooling, which gives $T \sim T_\gamma$. Now T is always close to 10^9 K and the computed luminosity at the inner boundary is $\sim 0.02 L_{Edd} \sim 30\% L_\infty$ (quite close to the input value), so conduction is not expected to be much effective.

8.3 Pairs Production–Annihilation in Radiative Transfer

In "hot" regimes the emitting gas may achieve semirelativistic or relativistic temperatures. Results presented in section 8.2 has been computed by tacking into account only for free–free and Compton scattering, but at semirelativistic temperatures a number of threshold processes appear, associated with creation of electron–positron pairs. Pairs are produced through photon–photon, photon–particle and particle–particle interactions, and the created pairs either annihilate into photons or participate in other photon and pair creation processes. The possible interactions are summarized in table 8.1 (Svensson 1982). In a steady state model the radiation field and the pair density must be computed simultaneously by solving the radiative transfer equation coupled with the pair equilibrium equation for the positron number density n_+. The latter one is derived balancing the total pair production and annihilation rates, and using the charge neutrality condition. In order to include these processes in our treatment, we extended the previous version of the characteristic code,

Table 8.1: **Physical Processes in Relativistic Plasmas**[a]

Basic Two Body Interaction	Radiative Variant	Pair Producing Variant
Moller & Bhaba scattering $ee \rightarrow ee$	Bremsstrahlung $ee \rightleftharpoons ee\gamma$	$ee \rightleftharpoons eee^+e^-$
Compton scattering $\gamma e \rightarrow \gamma e$	Double Compton scattering $\gamma e \rightleftharpoons \gamma e\gamma$	$\gamma e \rightleftharpoons ee^+e^-$
Pair annihilation $e^+e^- \rightarrow \gamma\gamma$	Three Quantum annihilation $e^+e^- \rightleftharpoons \gamma\gamma\gamma$	
Photon–Photon pair production $\gamma\gamma \rightarrow e^+e^-$	Radiative pair production $\gamma\gamma \rightleftharpoons e^+e^-\gamma$	
	Processes Involving Protons	
Coulomb scattering $ep \rightarrow ep$	Bremsstrahlung $ep \rightleftharpoons ep\gamma$	$ep \rightleftharpoons epe^+e^-$ $\gamma p \rightleftharpoons pe^+e^-$

[a] *Taken from Svensson (1982)*

including the solution of the detailed balance equation for n_+ and constructing numerical routines for the evaluation of the pair source term. In addition, the expressions of the free–free and Compton source terms previously presented were generalized to account for the presence of positrons.

In a plasma consisting of electrons, positrons and protons there are, in fact, four different types of free–free interactions: $e^- - p$, $e^+ - p$, $e^\pm - e^\pm$ and $e^+ - e^-$. In the Bohr approximation the $e^- - p$ and $e^+ - p$ cases are identical (see Jauch & Rohrlich 1976, Svensson 1982) and the former has been already discussed in Chapter 3. The photon spectrum for $e^+ - p$ bremsstrahlung is given by expression (3.4), provided that in the electron number density n_e is substituted by n_+. Referring again to Chapter 3, we recall that the electron–electron emissivity was reduced to a triple integral exploiting results by Dermer (1984, 1986). The final expression is

$$\eta_{e^--e^-}(\gamma,\tau) = \frac{n_e^2 c}{4\tau K_2^2(1/\tau)} \int_1^\infty d\gamma_r \frac{(\gamma_r^2-1)}{[2(\gamma_r+1)]^{1/2}} \int_0^{\zeta(\gamma_r)} \frac{d\gamma^*}{\gamma^*} \frac{d\sigma^*_{e^--e^-}(\gamma^*,\gamma_r)}{d\gamma^*} \quad (8.4)$$

$$\times \quad \exp\left\{-\frac{[2\,(\gamma_r+1)]^{1/2}}{\tau}\left(\frac{\gamma^2+\gamma^{*2}}{2\gamma\gamma^*}\right)\right\}$$

where $\tau \equiv KT/m_ec^2$, $\gamma \equiv h\nu/m_ec^2$, and $d\sigma^*_{e^-e^-}(\gamma^*,\gamma_r)/d\gamma^*$ is the differential cross section, given as a single quadrature by Dermer (1986, see also Haug 1975). The same expression holds for $e^+ - e^+$ emission, apart the substitution of n_+^2 in lieu of n_e^2. In a similar way it is straightforward to account for $e^+ - e^-$ interactions: the only differences are that expression (8.4) must be multiplied by 2 (since in this form it contains a factor 2 that corrects for double counting if particles are identical), n_e^2 must be substitute with $n_e n_+$ and the appropriate differential cross section is given by Haug (1985, see again Dermer 1986). The numerical evaluation of these additional contributions has been done exactly in the same way discussed in Chapter 3: $\eta_{e^+e^+}$ and $\eta_{e^+e^-}$ have been computed in the ranges $2\times10^{-2} \leq \tau \leq 10$, $2\times10^{-2} \leq h\nu/KT \leq 25.12$. The total Gaunt factor was then fitted with the analytical function suggested by Stepney & Guilbert (1983), and these results were used in the radiative transfer code. In the non–relativistic ($\tau \lesssim 10^{-2}$) and extreme–relativistic ($\tau > 10$) regimes the asymptotic limits by Gould (1980), Quigg (1968) and Alexanian (1968) have been used.

Finally, the positron contribution to photon scattering can be simply accounted for by multiplying, in the expression of the source term (see Chapter 3), the scattering opacity κ_{es} by a factor $(1+2z)$, where $z = n_+/n$, n is the proton number density and the charge neutrality condition $n_e = n_+ + n$ has been used.

As far as pairs producing mechanisms, we restrict our discussion to photon–photon pairs production, that dominates over photon–particle and particle–particle collisions for $\tau < 10$ (Svensson 1982). Moreover, for the sake of simplicity, we assume that pairs thermalize with

electrons and protons in the atmosphere. Clearly this is just an *ad hoc* assumption that needs to be checked a posteriori (see the discussion later in this section).

Let us therefore to consider the process

$$\gamma + \gamma \rightleftharpoons e^+ + e^- ; \tag{8.5}$$

quantities relative to the two photons will be denoted with indices 1, 2. In order to avoid confusion, in the rest of this section we use a more standard notation for expressions related to pairs processes: the symbol γ indicates photons, while $x \equiv h\nu/m_e c^2$ is the dimensionless energy. We also specify the discussion to the plane–parallel case, using as spatial independent variable the scattering optical depth. However, all expressions can be re-written in other 1-D geometries with obvious substitutions.

The absorption coefficient for a photon of energy x_1 propagating in direction μ_1 through a radiation field of intensity $I_2 = I(\tau_{es}, x_2, \mu_2)$ is given by

$$a_{\gamma\gamma}(x_1) = \frac{1}{hc} \int \frac{I_2}{x_2} \sigma(x) (1 - \mu) \, dx_2 d\mu_2 d\phi_2 , \tag{8.6}$$

where $x^2 = x_1 x_2 (1 - \mu)/2$ is the square of the photon energy in the center–of–momentum frame, μ is the cosine of the angle between the two photon directions, ϕ_2 is the azimuthal angle and $\sigma(x)$ is the photon–photon pair production cross–section (see e.g. Jauch, & Rohrlich 1976). Replacing ϕ_2 with $\phi = \phi_2 - \phi_1$ and introducing $x_\pm^2 = x_1 x_2 [1 - \cos(\theta_1 \pm \theta_2)]/2$ (see Stepney, & Guilbert 1983), expression (8.5) becomes

$$a_{\gamma\gamma} = \frac{4}{hc} \int dx_2 d\mu_2 \frac{I_2}{x_1 x_2^2} F(x_+, x_-) . \tag{8.7}$$

The function

$$F(x_+, x_-) = \int_{x_-}^{x_+} \frac{\sigma(x) x^3 dx}{\sqrt{(x_+^2 - x^2)(x^2 - x_-^2)}} \tag{8.8}$$

does not depend on the specific intensity so it was calculated once for all on a fixed grid of values of $x_{\pm}$ and stored in a matrix. The outer double integral was then computed using a spline interpolation.

A simple expression for the spectral emissivity of annihilating Maxwellian electrons and positrons was derived by Svensson (1983, see also Stepney & Guilbert 1983) by using a detailed balance approach. The resulting expression is

$$\frac{dN}{dVdtdx} = n_+ n_e \sigma_T c \frac{2\exp(-x/\tau)}{\tau K_2^2(1/\tau)} I(x\tau) \tag{8.9}$$

where the quantity $I(x\tau)$ involves a single integral over the pair production cross–section. Polynomial fits for I were also provided by Svensson (1983), with a maximum error of 0.3 per cent; in our numerical evaluation these analytical expressions were used.

Using these results, we finally obtain the expression of source term for photon–photon pair production–annihilation appearing in the transfer equation

$$\frac{g_P}{E} = \frac{1}{4\pi m_e c^3 E^2} \frac{dN}{dVdtdx} - \alpha_{\gamma\gamma} f \,. \tag{8.10}$$

The last ingredient we need is the additional equation for n_+, i.e. the detailed balance equation. This is obtained by equating the two total rates of production and annihilation. Once the absorption coefficient is known from expression (8.6), the pair production rate $R_{\gamma\gamma}$ is obtained performing two further integrations over angles and energies

$$R_{\gamma\gamma} = \frac{\pi}{h} \int dx_1 d\mu_1 \frac{I_1}{x_1} a_{\gamma\gamma} \,, \tag{8.11}$$

while the pair annihilation rate can be expressed in terms of a dimensionless function of the gas temperature, $A(\tau)$, as (Svensson 1982)

$$\dot{n}_+ = n_+ n_e c r_e^2 A(\tau) \,, \tag{8.12}$$

where

$$A(\tau) = \frac{\pi}{1 + 2\tau^2 / \ln(2\eta\tau + 1.3)}, \tag{8.13}$$

$\eta \simeq 0.56146$ and r_e is the classical electron radius. Combining the previous expressions and using again the charge neutrality condition, the pair balance equation becomes, in the stationary case

$$R_{\gamma\gamma} - z(1+z)n^2 c r_e^2 A(\tau) = 0\,. \tag{8.14}$$

Finally, the positive root of equation (8.14) is

$$z(\tau_{es}) = \frac{1}{4}\left(\sqrt{1 + \frac{16R_{\gamma\gamma}}{n^2 A(\tau) r_e^2 c^2}} - 1\right). \tag{8.15}$$

With the inclusion of photon–photon pairs production–annihilation, our numerical scheme is now general enough to deal with the transfer problem for unmagnetized plasmas in the semirelativistic and relativistic regime. At this level it can be used to investigate the radiation hydrodynamical problem in the 1–D case, provided that the gas temperature does not exceed $\tau \approx 10$. Under this condition, all the main radiative processes (free–free, Compton scattering and photon–photon pairs production) are accounted for in their most general form. At $\tau \gtrsim 10$ other pairs production mechanisms as photon–particle and particle–particle interactions start to be important, but we stress again the fact that the inclusion of additional radiative processes is straightforward, provided that the corresponding cross–sections are available.

8.4 Evaluation of the Pairs Density in "Hot" Atmospheres

As far as the model presented in section 8.2 is concerned, pairs processes do not play an important role in the transfer problem, and the extended version of the numerical code has

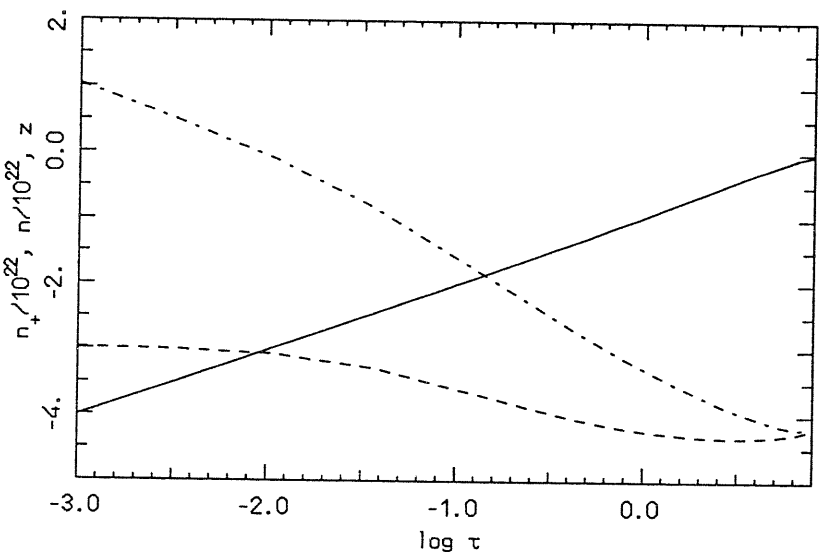

Figure 8.4: *Proton (full line), positron (dashed line) number densities (in units of* 10^{22} cm^{-3}*) and* $z = n_+/n$ *(dash–dotted line) versus the scattering optical depth for the model of figure 8.2.*

been used to check "a posteriori" the validity of the numerical results already reported. First, using the specific intensity and the run of thermodynamical variables derived in section 8.2 and solving the detailed balance equation (8.14), we calculated the positron number density. The resulting profile is shown in figure 8.4, together with n and z. As it can be seen, while in the inner atmospheric regions no relevant pair production is expected, the value of z becomes ~ 10 for $\tau_{es} \approx 10^{-3}$ and tends to increase in the external regions. Then, we solved again the radiative transfer equation and the energy balance equation, the latter modified to account for pairs production, by means of a relaxation scheme and using the numerical profiles computed in absence of pairs as trial solutions. We found that, since in this model z reaches its larger values in optically thin regions, pair production does not play an important role in shaping the emergent spectrum and the previous results are not significantly affected when this additional radiative process is accounted for. On the other

hand, as it will be discussed in the next section, a significant pair production in the external atmospheric layers could be important as far as the stability of these regimes is concerned.

We stress that the treatment of pair processes presented here is based on the assumption that pairs thermalize with protons and electrons in the atmosphere. However, since the Eddington limit in a pair plasma is lowered by a factor m_e/m_p, there is in principle the possibility that large values of z are never reached, because pairs are accelerated outwards by the radiative force as soon as they are created. The characteristic timescale for radiative acceleration $t_{acc} \sim (2h/a)^{1/2} \sim 5 \times 10^{-9}(h/10)^{1/2}(L_\infty/L_{Edd})^{-1/2}$ s, $h \sim 10$ cm is the scale height of the envelope and $a \sim (GM/R_*)(L/L_{Edd})$ is the radiative acceleration, should be compared with the timescales for particle collisions and for the development of plasma instabilities. Coulomb collisions establish thermal equilibrium in a time $t_{coll} \sim 6 \times 10^{-7}(T/10^9)^{3/2}(n/10^{18})^{-1}$ s, while the growth time for the counter–streaming instability is $t_{ins} \sim 2 \times 10^{-11}(n/10^{18})^{-1/2}$ s (see e.g. Melrose 1986). Plasma instabilities have therefore enough time to produce microturbulence which, in turn, will efficiently couple $e^\pm$ to the ambient plasma. Enhanced particle scattering prevents pairs from escaping and also allows them to thermalize with atmospheric electrons. Our initial assumption that pair production/annihilation is in equilibrium seems indeed justified.

8.5 Discussion and Conclusions

The existence of "hot" solutions, first proposed in paper I, has been confirmed by means of a more detailed calculation of the radiation field. Our frequency– and angle–dependent approach allowed us to compute the specific intensity and hence to evaluate the photon–

photon pair production. The temperature and density profiles are close to those presented in paper I and the spectrum peaks at about 500 keV.

First of all, we wish to comment about the possibility of getting a "hot" solution started. Of course, the thermal energy stored in a "hot" atmosphere is much larger than in a "cold" one, and it is roughly

$$U_{th} \sim 4\pi R_*^2 y^{tr} \left(\frac{KT}{m_p}\right) , \tag{8.16}$$

where T is the average temperature. Assuming $KT \sim 100$ keV, $U_{th} \sim 10^{31}$ erg, a factor ~ 100 above the "cold" case. The transfer of energy from protons to electrons in our model is described by equation (7.1). Obviously, this is a rather crude estimate which does not enter into the details of the physical processes responsible for the energy exchange. Heating associated with the proton stopping might produce temperatures only in the keV range, so the transition between "cold" and "hot" states could require some more efficient heating process, like dissipation of shock waves or magnetic field reconnection. We note, however, that the proton bulk kinetic energy at the neutron star surface is ~ 100 MeV, which is much higher than the temperature of "hot" solutions. In any case, the smallness of the energy content of the atmosphere compared to the value of the luminosity, $L_\infty \sim 10^{37}$ erg/s, strongly indicates that there should be no severe physical hindrance to drive the transition on time scales of microseconds.

On the other hand, one can argue that the "hot" state should be short–lived. In fact, as shown is section 8.4, pair production is expected to become important, at least in the outer layers where the pair density reaches its equilibrium value at $z \sim 1 - 10$. Due to the extra opacity produced by $e^{\pm}$, the critical luminosity in the atmosphere becomes a factor $1 + 2z$ lower than the Eddington limit. In "hot" models with $L_\infty \sim 0.1 L_{Edd}$, where pairs appear

to be coupled with the plasma, part of the envelope will become necessary dynamically unstable when $z \sim 5$. One should expect the outer layers to be expelled very quickly at the onset of the "hot" state: as a consequence accretion may be inhibited with the possible production of a relativistic shock wave. This suggestion is corroborated by the consideration that the momentum fluxes of the two flows are within an order of magnitude, as can be seen comparing $\dot{M}_{acc}v_{acc}$ and $\dot{M}_{out}v_{out} \approx M_{out}a$, where $M_{out} \sim 4\pi R_*^2 y$ is the mass in the unstable part of the atmosphere and $a \sim GM[(1+2z)L/L_{Edd} - 1]/R_*^2$ is the acceleration. Using the numerical results of section 8.4 and assuming $\dot{M}_{acc} \sim L(R_*/GM)$, $v_{acc} = c(r_g/R_*)^{1/2}$, which gives an upper limit for the momentum flux of the ingoing material, it turns out that $\dot{M}_{acc}v_{acc} \lesssim 10\dot{M}_{out}v_{out}$. The decrease of the accretion rate and of the luminosity may push the system in a regime where only the "cold" solution exists, giving rise to an on–off behaviour.

The "hot" state should be characterized by a spectrum close to that shown in figure 8.2, with typical emission at ≈ 100 keV. Moreover, pair bursts are expected, each consisting of $\sim 4\pi R_*^2 yz/m_p \sim 6 \times 10^{35}$ particles; an upper limit for the integrated luminosity in the annihilation line will be of order of 10^{29} erg. These hot, optically thin and Comptonized envelopes bear some resemblance with hot coronae above accretion disks, although the geometry, the heating process, and the triggering of the pair instability may be different. The onset of the "hot" state represents a possible physical mechanism for producing efficiently high energy radiation from weakly magnetized, accreting neutron stars and may be of interest in connection with hard X–ray transients, although we are aware that some simplifying assumptions, like spherical symmetry and absence of magnetic fields, may limit the applicability of our results.

At present hard emission ($E \gtrsim 30$ keV) has been observed from a number of sources, believed to contain NSs, with SIGMA and BATSE (see e.g. Tavani, & Liang 1996; Vargas et al. 1996). At least seven X–ray bursters, including Aql X–1, and other LMXBs show transient emission in the range 30–200 keV, with intensity anticorrelated with that in the soft band. These observations are of the utmost importance, since hard X–rays emission were previously associated only with X–ray pulsators and black hole candidates. Tavani, & Liang have proposed a possible explanation for the transient, hard state of these sources in terms of magnetic reconnection in the inner regions of an accretion disc around the NS, but the nature of the primary emission mechanism is still an open issue. The total X–ray luminosity of these sources is $\sim 10^{36} - 10^{37}$ erg/s, close to that considered in our model, although the duration of the hard state is several days. In our picture, this would imply that the appearance of $e^{\pm}$ pairs, even if it affects the accretion process, does not induce the transition to the "cold" state. Hard states of shorter duration would be impossible to detect with BATSE and SIGMA, but they may be observed by the instrumentation on board of XTE or SAX.

Results reported in this Chapter have been recently published in Zane, Turolla & Treves (1997a,b)[1].

---

[1] As far as the paper Zane, Turolla & Treves 1997a is concerned, we are indebted both to an anonymous referee for drawing our attention on the importance of thermal conduction in "hot" models and to the second referee, Lev Titarchuk, for his clarifying comments. The revised version of this paper greatly benefited from discussions with Fred Lamb, Luciano Nobili and Luca Zampieri. We are also grateful to Marco Tavani for useful discussions about hard X–ray transients.

9 X–Ray Emission from Old, Isolated, Accreting Neutron Stars

The last chapter of this thesis contains a short review about the issue of observing old, isolated neutron stars accreting the Interstellar Medium (ISM). This possibility is particularly interesting since Galactic ONSs represent a well populated class of stars, with a total number as high as $10^8 - 10^9$. The idea that such objects, when fed by the interstellar gas, may show up as very weak, soft X–ray sources, was originally suggested more than twenty years ago by Ostriker, Rees & Silk (1970). Using the Bondi–Hoyle accretion theory, they have shown that ONSs bolometric luminosities should be $\approx 10^{31}$ erg s^{-1} for typical ISM densities and star velocities; assuming spherical symmetry and a black body spectrum, the characteristic temperature is 10–100 eV. These two typical values summarize the two basic reasons that make the detection of these sources extremely difficult: their intrinsic weakness, and the fact that the emitted radiation falls in an energy band which is not easily accessible even to spaceborne instrumentation. Moreover, due to the combined differential effects introduced by the response of the detector and the absorption of the ISM, any theoretical estimate of observability crucially relies on both assumptions of the spectral shape and evaluation of the mean photon energy.

The detection of ONSs was included as a possible target for the *Einstein* mission (Helfand *et al.* 1980), but it was only a decade later, with the launch of the satellites EUVE and ROSAT especially committed to the study of the extreme ultraviolet and soft X–ray bands, that this issue came to life again. During the 90's, the subject became of rather broad interest and a number of investigations were presented (see e.g. Treves & Colpi 1991, hereafter TC; Blaes & Madau 1993, hereafter BM; Colpi, Campana, & Treves 1993; Madau & Blaes 1994; Treves *et al.* 1995; Zane *et al.* 1995, 1996b and reference therein). It has become increasingly clear that a realistic estimate of the observability of ONSs relies on a thorough understanding of a number of issues. Just to give some examples, it requires informations about

a) the density and velocity distribution of ONSs: a subject of interest in itself, strongly related to the investigations of the pulsars birth rate and of their velocity distribution and evolution;

b) the magnetic field and spin evolution of isolated pulsars: one of the major unresolved issues in compact object astrophysics. The knowledge of these parameters for old neutron stars is crucial, since the accretion process itself may be severely hindered by the rotating magnetosphere;

c) the interstellar medium and Giant Molecular Clouds distributions;

d) the spectral properties of radiation emitted by neutron stars accreting at modest rates, and their dependence on the magnetic field.

In all these fields there has been substantial progress. The detectability of ONSs in favorable spatial regions, like giant molecular clouds and the Solar proximity, has been investigated

(BM, Colpi, Campana, & Treves 1993; Zane, Zampieri, Turolla & Treves 1996b) together with the expected overall emission, its contribution to the soft X–ray background (Zane *et al.* 1995) and to the diffuse X–ray source in the Galactic Center (Zane, Turolla, & Treves 1996). Simultaneously, a considerable effort aimed at discovering ONSs was started (Danner 1996; Motch *et al.* 1997; Belloni, Zampieri, & Campana 1997; Maoz, Ofek & Shemi 1997). Despite at least three promising candidates have been proposed (Stocke *et al.* 1995; Walter, Wolk, & Neuhäuser 1996, Haberl *et al.* 1996, 1997), at present it is becoming clear that the number of detectable ONSs is less than that expected by the standard theoretical models. The observational campaigns are in an advanced stage, but the preliminary observational results suggest that the paucity of detected ONSs may already be used in placing very important constraints on some properties of the population.

A detailed discussion about all topics related to the problem is beyond the scope of this thesis, and references themselves will be necessarily uncomplete, due to the large amount of work presented in literature. The main purposes of this Chapter are both to present our contribution and to briefly review the problem of the observability, describing the current theoretical and observational scenarios and summarizing the open issues. The structure of the Chapter is as follow. In section 9.1 we review the basic conditions under which accretion is possible. Section 9.2 contains a short discussion about the spectral properties (see also Chapter 7), while theoretical investigations about the observability of single sources are summarized in section 9.3. A report of the present status of observations is given in section 9.4. In section 9.5 we present our results for the X–ray diffuse source in the Galactic Center. Finally, we conclude with a critical discussion and some preliminary results of works in progress (section 9.6).

9.1 Accretion onto Isolated Neutron Stars

Let us to consider a star moving with velocity v relative to an ambient medium of number density n. If the star is moving supersonically through the ISM, the main contribution to the accretion rate comes from the material swept by its motion. In this case, the accretion rate is given by

$$\dot{M} = \pi r_{acc}^2 m_p n v \sim 10^{11} n v_{10}^{-3} M_*^2 \,\mathrm{g\,s^{-1}}\,, \tag{9.1}$$

where $r_{acc} = 2GM_*/v^2$ is the accretion radius, M_* is the star mass in solar masses, and $v_{10} \equiv v/(10\,\mathrm{km\,s^{-1}})$. On the other hand, when dealing with the problem of the observability, we are mainly interested in the low–velocity tail of the ONSs distribution, because these are the stars which radiate the higher luminosities. Their velocity may become lower than the ISM sound speed, and the accretion rate is then fixed by the thermal velocity; in this case in the previous formula v is replaced by the local sound speed of the interstellar gas, c_s (see e.g. Novikov & Thorne 1973). Since the accretion radius turns out to be always smaller than the Strömgren radius by a factor 10^3, c_s is the sound speed in a fully ionized medium at the equilibrium ionization temperature ($T \sim 10^4$ K)

$$c_s \sim 10\sqrt{(T/10^4\,\mathrm{K})}\,\mathrm{km\,s^{-1}} \sim 10\,\mathrm{km\,s^{-1}}\,. \tag{9.2}$$

In the case of NSs, however, strong magnetic fields and fast rotation may inhibit accretion because of the momentum outflow, produced by the spinning dipole, and of the propeller effect, induced by the corotating magnetosphere (Ostriker, Rees & Silk 1970; Illarionov & Sunyaev 1975; Davies & Pringle 1981; Blaes *et al.* 1992). Following BM and Treves, Colpi & Lipunov (1993), two basic conditions must be verified in order to make accretion possible. Consider a NS with dipolar field B at the surface and a rotational period

P; the rotating B–field produces, in vacuo, a relativistic outflow with an energy density

$$U_B = \left(\frac{B^2}{8\pi}\right)\left(\frac{R_*^6}{r_c^6}\right)\left(\frac{r_c^2}{r^2}\right) \sim 7.5\times 10^{-9} B_{12}^2 P^{-4} R_6 r_{14}^{-2}\,\mathrm{erg\,cm^{-3}}\,, \tag{9.3}$$

where $R_6 \equiv R_*/\,(10^6\,\mathrm{cm})$, $B_{12} \equiv B/\,(10^{12}\,\mathrm{G})$, $r_{14} \equiv r/\,(10^{14}\,\mathrm{cm})$, R_* and $r_c = cP/2\pi$ are the star and light radius, respectively. Accretion can proceed if the gravitational energy density of the incoming gas

$$U_G = \frac{GM_* m_p n}{r} \sim 6.5\times 10^{-13}\dot{M}_{11} r_{14}^{-5/2}\,\mathrm{erg\,cm^{-3}}\,, \tag{9.4}$$

$\dot{M}_{11} \equiv \dot{M}/\,(10^{11}\,\mathrm{g\,s^{-1}})$, exceeds U_B at the accretion radius. This condition is met only when the NS has spun down to a period

$$P \gtrsim P_1 \sim 10 B_{12}^{1/2}\dot{M}_{11}^{-1/4}(r_{acc})_{14} R_6^{3/2} M_*^{-1/8}\ \mathrm{s}\,, \tag{9.5}$$

$(r_{acc})_{14} \equiv r_{acc}/(10^{14}\mathrm{cm})$. Since the star is slowing down at the magnetic dipole rate, this barrier is overcome in a time $t_1 \sim 4 B_{12}^{-1}\dot{M}_{11}^{-1/2}$ Gyr. As discussed by BM, as order of magnitude, this value is uncomfortably close to the age of the Galaxy. However, if the value is taken literally, it implies that a large fraction of ONSs can have spun down sufficiently, at least if the majority of them are born early in the Galactic history. Actually, depending on the ONSs velocity distribution, this fraction can be as high as half of the total number (see BM).

After P has increased above P_1, the infalling material proceeds undisturbed until the NS magnetic energy density balances the matter bulk kinetic energy density at the Alfven radius

$$r_A = \left(\frac{B^2 R_*^6}{\sqrt{2GM_*}\dot{M}}\right)^{2/7} \sim 2\times 10^{10} B_{12}^{4/7}\dot{M}_{11}^{-2/7} R_6^{12/7} M_*^{-1/7}\mathrm{cm}\,, \tag{9.6}$$

which lies inside the light cylinder for typical parameter values. The corotating magnetosphere will then prevent the accreting material to go any further, unless the gravitational acceleration at the Alfven radius is larger than the centrifugal acceleration

$$\frac{GM_*}{r_A^2} \gtrsim \left(\frac{2\pi}{P}\right)^2 r_A \,. \tag{9.7}$$

This condition translates in another, stronger constraint in the value of the period, since it must be

$$P \gtrsim P_2 \sim 10^3 B_{12}^{6/7} \dot{M}_{11}^{-1/2} M_*^{-1/2} \text{ s} \,. \tag{9.8}$$

If even the second barrier is overcome, matter can slide along the open field lines and finally reach the NS surface on the polar caps of radius

$$r_{cap} \sim \frac{R_*^{3/2}}{r_A^{1/2}} \sim 7 \times 10^3 B_{12}^{-2/7} \dot{M}_{11}^{1/7} R_6^{9/14} M_*^{1/14} \text{ cm} \,. \tag{9.9}$$

The centrifugal barrier at the Alfven radius poses a severe problem, since P_2 is so large that it can not be reached by magnetic dipole braking. However, other effects are indeed important. First, we must take into account the so–called propeller mechanism: the accreted matter will be spun up by the magnetosphere, and it will exert a torque on the NS (see e.g. BM). The interaction between magnetosphere and plasma is poorly understood and requires a full three dimensional simulation, but approximated expressions for the torque were presented by BM. Basing on that treatment, the corresponding spin–down time to P_2 turns out to be $\sim 0.04 B_{12}^{-11/14} n^{-17/28} v_{10}^{29/14}$ Gyr, a value adeguate to allow interstellar accretion. Numerical simulations indicate that more rapid spin down occurs if the material builds up, compressing the magnetosphere and becoming unstable to large scale mixing with the B–field (Wang & Robertson 1985).

Moreover, there is another effect that may play an important role in making accretion possible, i.e. the decay of the B–field. As already stated in Chapter 7, the time evolution of NSs magnetic field is still a very controversial issue. While for NSs in binaries there are some observational evidences that the magnetic field may decay on a timescale $\approx 10^7$ yr, leaving possibly a relic component of $\approx 10^8 - 10^9$ G, no firm conclusions have been reached in the case of isolated objects (see e.g. Srinivasan 1997; Wang 1997). Theoretical studies lead, on the one hand, to exponential or power law forms of field decay (Ostriker & Gunn 1969; Sang & Chanmugam 1987; Goldreich & Reisenegger 1992; Urpin, Chanmugam & Sang 1994), on the other to little or no decay at all within the age of the Galaxy (Romani 1990; Srinivasan *et al.* 1990; Goldreich & Reisenegger 1992). Statistical analysis based on observations of isolated radio pulsars give equally equivocal results (Narayan & Ostriker 1990; Sang & Chanmugam 1990; Bhattacharya *et al.* 1992), owing in part to the difficulty in treating selection effects (Lamb 1992). From observations, the present status of art merely states that there is no evidence of field decay during the pulsar phase, but this fact does not preclude the possibility of field decay over much longer timescales. On the other hand, different approaches to pulsar statistics led, independently, to the conclusion that, if the magnetic field decays, then it probably does over a timescale ~ 100 Myr, that is well above the characteristic pulsar lifetime (Srinivasan 1997, Hartman *et al.* 1997).

Keeping in mind these uncertainties, it follows that values of B between 10^9 and 10^{12} G should be considered as equally probable. However, as far as the observability of accreting ONSs is concerned, at the present the most investigated scenario is that one in which the magnetic field decays, leaving a relic component $B \sim 10^8 - 10^9$ G. In this case, a large fraction of the entire NS population may have spun down to a period larger than both

P_1 and P_2 in a time lower than the age of the Galaxy. Actually, standard models rely on the stronger assumption that all old local NSs do in fact accrete steadily (see again BM). For this reason, in the following discussion we will maintain this assumption, and we shall present the standard scenario. We will come back to the important issue of the magnetic field evolution in section 9.6.

The luminosity produced by the accretion process is

$$L \sim \sqrt{1 - \frac{2GM_*}{c^2 R_*}} \dot{M} c^2 \sim 2 \times 10^{31} \dot{M}_{11} \,\mathrm{erg\,s^{-1}} \tag{9.10}$$

which is orders of magnitude below the Eddington limit. This implies that matter is very nearly in free–fall until it reaches the NS surface. The dynamical time is then much shorter than the radiative cooling times and no energy is released before the flow hits the outermost stellar layers. Here accreting protons are decelerated by Coulomb collisions with atmospheric electrons and/or by plasma interactions and the flow stops after penetrating a few ($\lesssim 10$) Thomson depths in the NS atmosphere. The bulk kinetic energy of the infalling protons is transformed into thermal energy and finally converted into electromagnetic radiation (see Chapter 7).

9.2 The Emitted Spectrum

The choice of the most favorable energy bands for detecting accreting ONSs is crucially related to the spectral properties of the emitted radiation and in particular on the mean photon energy. In order to estimate this parameter, the first question that should be addressed is the relative efficiency of thermal and non–thermal radiative processes. Let us start assuming that thermal bremsstrahlung is the dominant emission/absorption mecha-

nism (see Chapter 7 of this thesis and references therein). In this case, the gas temperature in the inner, thermalized atmospheric layers should be close to the effective temperature

$$T_{eff} = \left(\frac{L}{4\pi R_*^2 \sigma}\right)^{1/4} \sim 3.4 \times 10^5 L_{31}^{1/4} R_6^{-1/2} \text{ K}, \tag{9.11}$$

where $L_{31} \equiv L/(10^{31} \text{ erg s}^{-1})$. Since the atmosphere is geometrically thin (see again Chapter 7), the hydrostatic balance equation

$$\frac{dP}{d\tau_{es}} \propto -\frac{M_*}{R_*^2} \tag{9.12}$$

can be immediately integrated to get the pressure as a function of the scattering depth. If $T \approx T_{eff}$, this yields an estimate for the gas density

$$\varrho \approx \frac{GM_* m_p \tau_{es}}{R_*^2 k T_{eff}} \sim 16 \tau_{es} M_* R_6^{-2} (T_{eff})_5^{-1} \text{ g cm}^{-3} \tag{9.13}$$

where $(T_{eff})_5 \equiv T_{eff}/(10^5 \text{ K})$. For typical values of density and temperature, the free–free optical depth $\tau_{ff} \sim (\kappa_{ff}/\kappa_{es})\tau_{es}$ is much larger than unity up to $h\nu \gg kT_{eff}$, so that thermal equilibrium is established in the dense inner layers. On the other hand, Compton scattering is not expected to modify the spectrum because of the relatively low Thomson depth and electron temperature. Cold atmospheric electrons emit cyclotron radiation. However, for $B \sim 10^9$ G the cyclotron line contribution to the total luminosity is vanishingly small and it never exceeds a few percent even for $B \sim 10^{12}$ G (Nelson *et al.* 1995). These considerations lead to the conclusion that, at least in the first approximation, some informations about the typical energies can be obtained assuming that the spectrum emitted by accreting ONSs is a blackbody at T_{eff}. In these assumptions, emission turns out to be peaked at an energy

$$E \sim 3kT_{eff} \sim 100 L_{31}^{1/4} R_6^{-1/2} \text{ eV} \tag{9.14}$$

which falls in the extreme UV/soft X–ray range.

Although a low magnetic field ($B < 10^{10}$ G) is not going to produce any major effect on emission/absorption processes, its presence has an important consequence on the emitted spectrum. Let us consider two ONSs, with the same mass and radius, accreting matter at the same rate, one with a relic field $B = 10^9$ G, the other unmagnetized. The only effect of a low B–field is to channel the accretion flow onto two polar caps, and the total emitting area is now $2A_c$, where $A_c = \pi r_{cap}^2$. The limited size of the radiating region produces a hardening of the spectrum with respect to the unmagnetized case with the same luminosity. In terms of effective temperature, it is

$$\frac{(T_{eff})_{mag}}{(T_{eff})_{unmag}} = \left(\frac{4\pi R_*^2}{2\pi r_{cap}^2}\right)^{1/4} \sim 5 B_9^{1/7} \dot{M}_{11}^{-1/14} R_6^{5/28} M_*^{-1/28} \tag{9.15}$$

where $B_9 \equiv B/(10^9\,\mathrm{G})$.

Moreover, detailed radiative transfer calculations (see Chapter 7 of this thesis; Zampieri *et al.* 1995) which we have already mentioned, have shown that the actual spectrum sensibly deviates from a Planckian: it is harder than a blackbody at T_{eff} and the hardening becomes more pronounced as the luminosity decreases. Although model spectra were computed for a NS accreting on the entire surface, this result is independent of the emitting area. It is due to the fact that higher frequencies decouple at larger scattering depths in the NS atmosphere, where temperature is higher: the emerging spectrum is a superposition of blackbody spectra at different temperatures, which is broader than a Planckian at T_{eff}. At energies larger than 0.5 keV, where the blackbody emission becomes vanishingly small, the computed spectrum shows a persistent tail and a fraction of 10%–20% of the total flux is emitted above this threshold; the typical hardening factor is ~ 2 at $L \sim 10^{31}\,\mathrm{erg\,cm^{-3}}$. Taking into account both the hardening of the spectrum due to the differential character

Table 9.1: **Bandpasses and thresholds for the EUVE and ROSAT instruments**

detector	filter	bandpass (keV)	threshold[a] (ct/s)
EUVE ASS	Lex	0.071–0.214	0.01
EUVE DE	Lex	0.069–0.183	0.015
ROSAT WFC	S1	0.09–0.206	0.02
ROSAT WFC	S2	0.062–0.11	0.025
ROSAT PSPC	T	0.2–2.4	0.015

[a] *All-Sky Survey*

of the free–free opacity and that one induced by the presence of B, it turns out the ONSs are, mainly, soft X–ray emitters with a spectrum peaked at $\sim$ 1 keV for typical parameter values. This makes these sources possible targets for detectors on board ROSAT and EUVE (see table 9.1 for details).

It is worth noting that spectra presented by Zampieri *et al.* (1995) are quite similar to those emitted by cooling NSs for $B \lesssim 10^9$ G (Romani 1987; Rajagopal & Romani 1996; Zavlin, Pavlov & Shibanov 1996). This is not surprising, since, roughly speaking, when dealing with accreting or cooling NSs, the only difference in the model is that the additional input of energy comes from the top or from the bottom of the atmosphere. In both situations

the atmosphere is in near radiative energy equilibrium, and opacity is dominated by free-free. Numerical results show that the resulting temperature profiles are quite similar in the two cases, so that the emergent spectrum also presents the same characteristics, with an overall hardening with respect to a Planckian at T_{eff}.

No detailed spectral models of accreting NSs with high magnetic fields ($B \sim 10^{12}$ G) have been presented up to now. Nelson *et al.* (1995) evaluated the contribution of the cyclotron line, in the assumption that the thermal part of the emission is blackbody. For very high fields, however, the atmosphere is no more in LTE and a detailed analysis of radiative transfer including magnetic effects is required. Spectra from cooling NSs with $B \sim 10^{11} - 10^{12}$ G have been presented by Miller (1992), Shibanov *et al.* (1992). As they found, the main effect of a high magnetic field is to increase the opacity; as a consequence the hard X–ray tails are partially suppressed and the spectrum is much closer to a blackbody. On the other hand, under these circumstances ONSs might appear as unsteady intermittent X–ray sources. In fact, as pointed out by Treves, Colpi & Lipunov (1994), for $B \sim 10^{12}$ G magnetic pressure could temporarily stop the incoming flow, and the accretion process may be cyclic with recurrence time $\sim 10^6$ s.

9.3 Observability of ONSs

The first estimates about the observability of accreting ONSs with ROSAT were presented by TC, and their results have been later corroborated by a more complete analysis by BM, Zane *et al.* (1995). Both TC and BM restricted their discussion to the case in which the spectrum is a blackbody at T_{eff}, emitted either from the entire star surface or from the

polar caps, while in Zane *et al.* (1995) we relaxed this hypothesis using calculated spectra by Zampieri *et al.* (1995). As it was shown in section 9.1, the ONSs accretion luminosity strongly depends on the star velocity with respect to the ISM and on the local density of the surrounding material. As a consequence, once the emitted spectrum is known, this kind of analysis relies on the knowledge of two key ingredients: the present ONSs distribution function in phase space and the morphology and physical state of the ISM.

Recent observations with the ROSAT Wide Field Camera during survey phases (Pounds *et al.* 1993) and with EUVE have provided evidence for the presence of a relatively small number ($\sim$ 23) of unidentified bright sources: this led Madau & Blaes (1994) to rule out there being as many as 10^9 isolated ONS in the Galaxy, if accretion is spherical. Uncertainties on the statistical properties of the old neutron star population and on the physics of the accretion process make nonetheless the issue of the total number of Galactic ONSs still controversial (see e.g. Treves *et al.* 1995). The search for favorable sites where accretion can make a lone neutron star shining is therefore of importance. Here we first review the basic picture, and then we focus on the discussion of these particular, most favorable sites, which are correlated with the denser phases of the ISM.

9.3.1 The Basic Picture

The spatial distribution of the ISM in the Galaxy is highly inhomogeneous. This introduces two main difficulties, since, for a given source, the interstellar density determines both the intrinsic luminosity and the amount of absorption along the line of sight. The situation is more complicated when dealing with the solar proximity, since here the ISM is highly anisotropic and its geography is complex (see the later discussion), while the gas structure

is smoother on larger scales and numerical fits for the distribution have been published in literature (see e.g. Dickey & Lockman 1990 for a review). In particular, observational data from Lyα and 21 cm absorption measures show that the ISM distribution of both cold and warm HI is nearly constant in radius while its z–dependence can be fitted by

$$n_{HI} = n_1 \exp\left(-\frac{z^2}{2\sigma_1^2}\right) + n_2 \exp\left(-\frac{z^2}{2\sigma_2^2}\right) + n_3 \exp\left(-\frac{z}{h}\right) \qquad (9.16)$$

with $n_1 = 0.395$, $n_2 = 0.107$, $n_3 = 0.064$; $\sigma_1 = 212$, $\sigma_2 = 530$ and $h = 403$ pc; n_i and σ_i are in cm^{-3} and pc, respectively. The applicability of the previous expression is restricted to the range $0.4 \leq R/R_0 \leq 1$, where R is the galactocentric radius and $R_0 = 8.5$ kpc is the distance of the Sun from the Galactic center. The gas layer has a scale height of about 230 pc in the vicinity of the Sun, while for $R \leq 0.4R_0$ it shrinks to ≈ 100 pc and in the outer Galaxy it expands linearly up to ≈ 2 kpc. The other important contribution to the total ISM density comes from molecular hydrogen. The best tracer of H_2 is the CO molecule, and observational data suggest a local gaussian distribution with a scale height of $\sim 60 - 75$ pc. Observations, however, are much less conclusive as far as the midplane density is concerned (Bloemen 1987), also because it may significantly depend on R (De Boer 1991). As a first approximation, the H_2 distribution can be described with a gaussian with central density $0.6\ \mathrm{cm}^{-3}$ and FWHM 70 pc (De Boer 1991). The ionized component gives only a very small contribution to the total density, and it can be neglected.

As it can be seen from equation (9.16), typical values for n_H are about $0.2 - 0.5\,\mathrm{cm}^{-3}$; higher values seem to occur in the Sco–Cen and Per directions, where $n_H \sim 1 - 10\,\mathrm{cm}^{-3}$. Although a detailed map of the gas was used in Zane *et al.* (1995) to evaluate the ONSs collective emission, as far as the observability of individual sources is concerned, in all analysis previously quoted some simplifying assumptions have been introduced. Typically,

the ISM density n is treated as a free parameter, either assuming an homogeneous medium or, as in BM, mimicing different directions toward the Galactic plane and the poles.

The second ingredient is the present distribution function f of Galactic ONSs. Estimates by TC were derived using analytical expressions of the speed distribution obtained by Paczyński (1990) fitting results of a Monte Carlo calculation. In principle, the present shape of f can be obtained evolving spatial and velocity distributions at birth in the Galactic potential, and a detailed calculation was presented by BM (see also Hartmann, Epstein & Woosley 1990; Blaes & Rajagopal 1991; Frei, Huang & Paczyński 1992). Unfortunately, the velocity distribution of pulsars at birth is still poorly known, and any evolutionary scenario remains affected by this indetermination (and by assumptions about the overall Galactic gravitational potential as well, but, as discussed by BM, this is a much less important point). In a detailed study, Narayan & Ostriker (1990) found that observational data of periods and magnetic fields for a sample of about 300 pulsars are well fitted by invoking the presence of two populations of neutron stars at birth, slow (S) and fast (F) rotators. These two populations differ in their kinematical properties, and the F rotators are characterized by a mean velocity and by a scale height lower than the S ones. Basing on this picture, the evolved distribution function has been obtained by Blaes & Rajagopal 1991, BM, Zane *et al.* 1995; in the latter two papers estimates of the observability were based on these numerical results. Only the F population of Narayan and Ostriker (1990), which represents ~ 55 % of the total number N_{tot} of NSs, was taken into account; although the S population has a comparable birth–rate, it accretes much less matter on average than the F one and its contribution to the number of detected sources is negligible (BM). Results from our numerical calculation show that, after the evolution, in the local region 7.5 kpc $\leq R \leq$ 9.5 kpc ONSs are characterized

Table 9.2: **Predicted Number of Sources and Sampling Distances ($B = 0$)**

		All-Sky Survey		Deep-Exposure	
$n_H\,(cm^{-3})$	$\overline{v}\,(km\,s^{-1})$	$d_{max}\,(pc)$	$N_{ons}\,(\leq d_{max}, \leq \overline{v})$	$d_{max}\,(pc)$	$N_{ons}\,(\leq d_{max}, \leq \overline{v})$
			$L/L_{Edd} = 10^{-7}$		
0.2	9.9	525 (375)	260 (132)	1170 (725)	1293 (497)
0.5	13.	360 (240)	333 (148)	845 (425)	1837 (465)
1.	17.	275 (165)	253 (55)	675 (275)	2495 (414)
			$L/L_{Edd} = 4 \times 10^{-8}$		
0.2	14.	380 (220)	402 (135)	840 (445)	1965 (552)
0.5	19.	265 (145)	312 (51)	555 (275)	2324 (570)
1.	23.	195 (105)	262 (41)	415 (185)	2737 (544)

$z_{\rm ISM} = 300$ pc; *Taken from Zane et al. (1995).*

by a mean height scale $\langle z \rangle \sim 250$ pc and by a mean velocity, averaged over $|z| \leq 200$ pc, $\langle v \rangle \sim 78 \mathrm{km\,s^{-1}}$. The number density of stars, within 2 kpc from the Sun, turns out to be $n_0 = 3 \times 10^{-4} (N_{tot}/10^9)\,\mathrm{pc^{-3}}$. All these values are in close agreement with the results of BM. Once n and the spectrum are fixed, the observability of a source depends on its distance d, velocity and on the response of the detector. The count rate measured at earth, corrected for the absorption of the interstellar gas, is:

$$CR = \frac{1}{4\pi d^2} \int_{\Delta E} \frac{L_\nu}{h\nu} \exp\left(-\sigma_\nu N_H\right) A_\nu d\nu \tag{9.17}$$

where A_ν and ΔE are the detector effective area and bandpass, L_ν is the monochromatic luminosity at the source, N_H is the column density and σ_ν is the absorption cross section (Morrison & McCammon 1983). The effective areas can be found in Malina *et al.* (1994, Lex ASS), Edelstein, Foster & Bowyer (1995, Lex DE), Pounds *et al.* (1993, WFC) and in

the ROSAT guide for observers (PSPC). A star of luminosity $\overline{L}$ (i.e. moving at $v = \overline{v}$) can be observed up to a maximum distance d_{max} at which the count rate becomes lower than the sensitivity limit of the detector (in the case of the ROSAT PSPC: 1.5×10^{-2} counts/s for the all sky survey, ASS, and 10^{-3} counts/s for Deep Exposure, DE). As a consequence, the expected number of observable objects can be calculated by integrating within d_{max}:

$$N_{ons}(\leq d_{max}, \leq \overline{v}) = \int_{\Omega}\int_{0}^{d_{max}}\int_{0}^{\overline{v}} f r^2 dr d\Omega dv \qquad (9.18)$$

where r is the radial distance from the Sun. Results by Zane *et al.* (1995) are summarized in Tables 9.2, 9.3; for comparison the corresponding quantities, as derived for a blackbody spectrum are listed in parenthesis. Here $N_{tot} = 10^9$ was assumed, so numbers in the tables are normalized to $N_F = 5.5 \times 10^8$ (F population). As it can be seen from Table 9.2, ONSs are detectable up to typical distances $\approx 200 - 300$ pc for ASS, even if they emit from the entire surface. This scenario is in agreement with previous estimates by TC and BM; in particular, a comparison with TC results shows that these values are of the order of their estimates for polar cap accretion. The only difference is that, in our case, the spectral hardening is only due to radiative processes; when a non zero magnetic field is taken into account, objects with the same luminosity become visible at larger distances. As it is apparent from Table 9.3, if the magnetic field is 10^9 G about 10 sources deg^{-2} are expected to be above the DE ROSAT threshold; this figure is a factor ~ 10 greater than the estimates of TC. Apart of these differences related to the different hypothesis on the spectrum, the main conclusion from this kind of analysis is that a large number (thousands) of ONSs should appear in the ROSAT all sky survey, and in deep fields.

We have already mentioned that the issue of the present shape of f is still controversial. In particular, a different scenario was proposed by Lyne & Lorimer (1994), who suggested

Table 9.3: **Predicted Number of Sources and Sampling Distances (for Polar Cap Accretion)**

		All–Sky Survey		Deep–Exposure	
$n_H\,(cm^{-3})$	$\overline{v}\,(km\,s^{-1})$	$d_{max}\,(pc)$	$N_{ons}\,(\leq d_{max}, \leq \overline{v})$	$d_{max}\,(pc)$	$N_{ons}\,(\leq d_{max}, \leq \overline{v})$
		$L/L_{Edd} = 10^{-7}$			
0.2	9.5	760 (705)	480 (413)	2480 (2110)	5112 (3700)
0.5	13.	685 (595)	1069 (802)	2055 (1675)	9563 (6353)
1.	16.	615 (515)	1823 (1279)	1690 (1330)	13769 (8528)
		$L/L_{Edd} = 3 \times 10^{-8}$			
0.2	15.	410 (385)	611 (539)	1350 (1060)	6630 (4088)
0.5	20.	370 (305)	1345 (914)	1160 (845)	13224 (7017)
1.	25.	340 (260)	2382 (1393)	990 (695)	20128 (9954)

$B = 10^9$ G; $z_{\rm ISM} = 300$ pc; *Taken from Zane et al. (1995).*

the possibility that neutron stars are born with typical velocities significantly higher than both the F and S populations of Narayan & Ostriker. The resulting distribution peaks at about 250 km/s, and extends to velocities above 1000 km/s. Their analysis, however, is based on proper motion measures of a sample of 29 young radio pulsars and, consequently, may be not complete in the low–velocity tail (see also Hartman 1997; Hartman *et al.* 1997). Moreover, this result would *prima facie* imply that most pulsars evaporate from globular clusters and the Galactic plane. On the other hand, it must be stressed that the predicted number of detected sources does not strongly depend on the overall shape of the velocity distribution of ONSs, but only on the number of low velocity neutron stars, which are those accreting at the highest rate. A number of effects can affect the evolution of the low–velocity tail of f: for instance, dynamical heating was considered by Madau & Blaes (1994). This process, observed in the local disk star population, causes the velocity dispersion to increase with age as a consequence of scattering by molecular clouds and spiral arms (Wielen 1977). If ONSs participate the same process, dynamical heating over the lifetime of the Galaxy may scatter a fraction of low velocity stars to higher speeds and this, in turn, could decrease the source number counts up to a factor 10.

On the other hand, if we consider the f distributions at birth, it must be noted that, for a high velocity distribution such as that one by Lyne & Lorimer (1994), the extrapolation to low velocities seems to indicate that the number of stars with velocity less than $\sim$ 30 km/s, turns out to be of the same order as the correspondent fraction in the Narayan & Ostriker model. In addition, more recent results by Hansen & Phinney (1996), Hartman (1997) support a content of slow ONSs even larger than that of Narayan & Ostriker. As pointed out by Hansen & Phinney, the 3D velocity distribution of radio pulsars is not

strongly constrained at low velocities, and could peak at small v. Distributions with a larger component at low velocities (with respect to the Lyne & Lorimer one) are also supported by the results of a detailed model of population synthesis, recently presented by Hartman *et al.* (1997). This analysis is based on a sample of 129 pulsars, taken from the last version of the Princeton pulsar catalogue (Taylor, Manchester & Lyne 1993); all objects whose distance projected on the Galactic plane is less than 4 kpc have been included. As they found, models based on both the Hansen & Phinney and the Lyne & Lorimer distributions successfully reproduce the observed pulse period, magnetic field and luminosity distributions, with the former also giving a somewhat better description of the correlation between characteristic age and distance to the Galactic plane.

Modulo these caveats and keeping in mind of all the underlying uncertainties, we can therefore conclude that, at the present status of knowledge, as far as the observability of ONSs is regarded results are quite independent on the actual, overall shape of f and only the number of low velocity objects may strongly affect the picture. The proposed v distributions at birth, however, do not suggest that such fraction may be significantly lower with respect that one derived by Narayan & Ostriker.

9.3.2 The Most Favorable Sites

Assuming that accreting ONSs should indeed be detectable with ROSAT, and possibly EUVE, the obvious question is:

"how to pick them up in the sea of still unidentified, weak sources present in the surveys?"

Possible criteria for sorting out good ONS candidates are: the lack of any optical counterpart down to $m_v \sim 24$, soft X–ray spectra, extreme X to optical flux ratio and correlation

with the denser phases of the ISM. A promising strategy consists in identifying the conditions under which ONSs would produce the higher count rates. The number of non optically identified sources (NOIDs) is reduced as the cut off count rate is increased, leaving a manageable number of possible candidates, worthy of pointed observations.

Relatively high count rates are expected from ONSs accreting in the denser regions closer to the Sun. Of course, these regions must be large enough to contain a statistically significant number of slow NSs, which are the most luminous. In this respect, dense molecular clouds, where the ambient density is ~ 100 times higher than the average, seem to provide a very favorable environment for observing ONSs. This issue was investigated by BM; Colpi, Campana & Treves (1993) and Zane *et al.* (1995), using different assumptions about the emitted spectrum. Table 9.4 summarizes our results for a sample of 18 nearby clouds, studied by Dame *et al.* (1987). For a typical velocity v, which corresponds to a luminosity $l = 10^{-7}$ in Eddington units, the expected count rate is reported in column 6; the blackbody count rate is also listed for comparison (CR_{BB}). The last column contains the number of detectable sources, with luminosities higher than 10^{-7}; the interested reader is referred to Colpi, Campana & Treves (1993) and Zane *et al.* (1995) for all details. As it can be seen from the Table, in the case of polar cap accretion, the count rate turns out to be above the threshold of Rosat (in DE) for all clouds. Clouds 15–16 and 18 appear promising because of their high expected count rates; we note, however, that, since the number of neutron stars in the clouds is small, large statistical fluctuations are possible. Clouds 5–7, 9–13 represent the most favorable sites for observability and this agrees with the previous estimate presented by Colpi, Campana & Treves (1993).

In a recent paper, we suggested that the closest overdense regions of the solar neigh-

Table 9.4: **Estimated Observational Parameters of ONSs in Molecular Clouds (for Polar Cap Accretion)**

	Cloud	d_c	R_c	n_c	CR	CR^{a}_{BB}	v^{b}	$N^{b}_{ons}(\leq v)$
		pc	pc	cm^{-3}	s^{-1}	s^{-1}	$km\,s^{-1}$	
1	Cloud A	500	20	50	2.05×10^{-2}	1.24×10^{-2}	54	3
2	Cloud B	300	20	51	5.64×10^{-2}	3.39×10^{-2}	54	3
3	Cloud C	500	16	67	1.97×10^{-2}	1.17×10^{-2}	59	2
4	Vul Rft	400	23	61	2.62×10^{-2}	1.44×10^{-2}	58	5
5	Cyg Rft	700	67	29	6.70×10^{-3}	3.32×10^{-3}	45	78
6	Cyg OB7	800	64	29	5.32×10^{-3}	2.68×10^{-3}	45	68
7	Cepheus	450	45	20	2.67×10^{-2}	1.66×10^{-2}	40	18
8	Taurus	140	13	134	0.18	9.41×10^{-2}	75	1
9	Mon OB1	800	34	40	6.68×10^{-3}	3.72×10^{-3}	50	12
10	Orion A	500	27	84	1.15×10^{-2}	5.35×10^{-3}	64	10
11	Orion B	500	31	56	1.44×10^{-2}	7.41×10^{-3}	56	13
12	Mon R2	830	32	36	6.88×10^{-3}	4.02×10^{-3}	48	10
13	Vela Sheet	425	26	46	2.57×10^{-2}	1.48×10^{-2}	52	7
14	Cham	215	13	44	0.14	9.6×10^{-2}	52	1
15	Coalsack	175	8.5	65	0.22	0.15	59	0
16	G317–4	170	5	203	0.18	0.11	86	0
17	Lupus	170	18	53	0.18	0.11	55	2
18	Rcr A	150	7.6	68	0.3	0.21	60	0

[a] $T_{eff} = 1.6 \times 10^{-2}$ keV;

[b] $B = 10^{9}$ G; $l_{polar\,cap} = 10^{-7}$; *Taken from Zane et al. (1995).*

bourhood may represent another favorable direction for the detection of ONSs (Zane *et al.* 1996b). If we assume an ONSs spatial density of $\sim 3 \times 10^{-4}$ pc^{-3} (BM, Zane *et al.* 1995), about 140 ONSs are in fact present in a sphere of radius 50 pc centered on the Sun: their proximity makes these objects particularly promising, since a relatively high count rate is expected. Unfortunately, the local interstellar medium (LISM) is, on average, underdense and relatively hot so the advantage expected from the vicinity of the source may be deceptive because the bolometric luminosity is a factor $n_{\rm LISM}/n_{\rm ISM} \sim 0.07$ smaller (see next subsection). For a typical value of the ISM density in the Local Bubble, $n = 0.07$ cm^{-3}, and assuming $v = 40$ Km s^{-1}, the total luminosity is $\sim 7 \times 10^{28}$ erg s^{-1} and these sources would be within the EUVE and ROSAT WFC bandpasses, regardless of the details about the emitted spectrum. However, even if they are located at a distance of 20 pc, in the case of emission from the entire star surface, they are too faint to be above the sensitivity threshold of both detectors. In the case of polar cap accretion, a non–negligible fraction of the total luminosity is emitted in the 0.2–0.4 keV energy interval (S bandpass of ROSAT PSPC), producing a count rate ($\sim$ 0.1–0.6 counts/s) well above the sensitivity limit. However, the expected number of these relatively bright nearby sources (with $d \leq 20$ pc) is so small to be subject to large statistical fluctuations and, in addition, it could be strongly affected by the physical state of the gas in the Local Bubble which is poorly known: if the temperature is as large as 10^6 K, the accretion luminosity drops below $\sim 5 \times 10^{27}$ erg s^{-1} (corresponding to $v \simeq c_s \simeq 100$ km/s) and these sources would become too faint.

On the other hand, since the LISM is highly inhomogeneous and the contour of the Local Bubble is highly anisotropic, some particular directions may still be promising. As it will be discussed later on, there is at least one region in the second galactic quadrant, the Wall,

where the gas density approaches the average ISM density, $n \sim 1$ cm^{-3} (see Paresce 1984; Diamond, Jewell & Ponman 1995). Focussing on this region, we suggested the intriguing possibility that the nearest neutron stars may account for a non–negligible fraction of the relatively bright (> 0.1 counts/s) unidentified R–ASS sources in the Wall direction.

9.3.2.1 The Solar Proximity

As discussed, although a relatively high number of ONSs, $\gtrsim 100$, are expected within ~ 50 pc from the Sun, their observability as accretion powered sources is severely hindered by the shortage of fuel. In fact, in the presently accepted picture, the Sun is surrounded by a region, the Local Bubble, where the plasma has both very low density ($n \sim 0.05-0.07$ cm^{-3}) and high temperature ($T \gtrsim 10^5$ K). In the scenario proposed by McKee & Ostriker (1977), see also Cox & Anderson (1982), Cox (1983), the hot gas would fill $\sim 70 - 80\%$ of the interstellar space and a large number ($\sim 2 \times 10^4$) of cool ($T \sim 80$ K), roughly spherical clouds are expected to be present. Observational data support this model for the region beyond $\sim 50 - 100$ pc from the Sun (Knude 1979), but, as discussed by Paresce (1984), soft X–ray, radio and color excess surveys seem to indicate that no clouds are present at smaller distances and that the denser material is more probably organized into large, elongated, moving fronts within ~ 50 pc. The Sun itself is embedded in a medium, the Local Fluff, which is warm ($T \approx 10^3 - 10^4$ K) and slightly overdense ($n \sim 0.1$ cm^{-3}) with respect to the Local Bubble on scales $\lesssim 20$ pc (Diamond, Jewell & Ponman 1995).

Because both the underdensity and the high temperature in the Local Bubble work against the accretion process, we focus our attention on the location of the overdense, warm fronts in the local neighbourhood. The present picture indicates that the contour of the

Local Bubble in the Galactic plane is highly asymmetric, with four major discontinuities in four different Galactic sectors (Paresce 1984). In particular, a wall of neutral hydrogen is located very close to the Sun in the second quadrant, $15° < l < 120°$. According to Paresce (1984), the wall is roughly parallel to the $l = 330° - 150°$ axis and is located at $d \leq 16$ pc, with an estimated depth of about 35 pc. The N_{HI} contours presented by Frisch & York (1983) are generally farther away, with the denser material ($n \sim 1$ cm^{-3}) at ~ 90 pc from the Sun. Welsh *et al.* (1994) have derived a highly asymmetric contour of the Local Bubble that in the second quadrant is roughly intermediate between those presented by Paresce and Frisch & York. The minimum radius of the local cavity has been estimated to be $\sim 25 - 30$ pc, but, as stressed by the same authors, their indirect method could produce an underestimate of N_{HI} at distances smaller than 50 pc. A very recent analysis of ROSAT EUV data (Diamond, Jewell & Ponman 1995) has shown that n reaches ~ 1 cm^{-3} at $\sim 25 - 30$ pc and this result seems to be in agreement with the asymmetric contour found by Welsh *et al.* more than with those of Paresce, Frisch & York (see also Pounds *et al.* 1993). Despite this, the shrink of the local cavity to less than $25 - 30$ pc from the Sun cannot be ruled out on the basis of present observations.

Being very close, the overdense region in the second Galactic quadrant (the Wall) provides one of the most favorable environments for the detection of accreting ONSs. In order to shed light on its importance as far as the detectability of ONSs is concerned, we used two limiting models for the LISM in the Wall: in model I the overdense region is located between 16 and 50 pc, in model II between 30 and 50 pc; in both cases the angular range is $15° < l < 120°$, $|b| < 30°$. If the total number of ONSs in the Galaxy and their local density are taken to be $N = 10^9$ and $n_0 = 3 \times 10^{-4}$ pc^{-3} respectively, we expect 22 (model I) and

18 (model II) objects to be present in the Wall. In order to account for the interstellar absorption, we assume in model I a typical HI density of $n = 0.1\,\mathrm{cm}^{-3}$ in the Local Fluff and $n = 1\,\mathrm{cm}^{-3}$ between 16 and 50 pc (the Wall). In model II we use $n = 0.1\,\mathrm{cm}^{-3}$ within 20 pc, $n = 0.07\,\mathrm{cm}^{-3}$ for $20 < d < 30$ pc and $n = 1\,\mathrm{cm}^{-3}$ for $30 < d < 50$ pc. However, due to the high gas temperature in the Local Bubble, interstellar absorption between 20 and 30 pc can be safely neglected.

Although X–ray surveys toward the Galactic plane detect a very large number of sources, the extreme vicinity of the ONSs in the Wall could make them relatively bright and, as a consequence, detectable at larger flux limits. For $n \sim 1\,\mathrm{cm}^{-3}$ and $v = 40\ \mathrm{Km\,s}^{-1}$, the luminosity is $\sim 10^{30}\ \mathrm{erg\,s}^{-1}$ and the mean photon energy ranges from 40 eV in the case of accretion on the entire NS surface to 400 eV for polar cap accretion with a magnetic field of 10^9 G. As a consequence, a number of sources accreting in this locally overdense region turns out to be detectable at least by some of detectors on board ROSAT and EUVE.

Using our numerical results for the present ONSs distribution f (mentioned in subsection 9.3.1), we derived the fitting formula

$$G(v) = \frac{(v/v_0)^m}{1 + (v/v_0)^n} \tag{9.19}$$

to the computed cumulative velocity distribution. The use of this fit is to be preferred whenever an estimate of the number of ONSs in a limited volume of phase space is needed; in the previous expression $v_0 = 69\,\mathrm{km\,s}^{-1}$ and $n \simeq m = 3.3$. We assume that the star distribution is spatially homogeneous and use our derived value for the local density, $n_0 = 3 \times 10^{-4}\,\mathrm{pc}^{-3}$.

Three different spectral shapes have been considered: *a*) blackbody emission from the entire surface, *b*) blackbody emission from the polar caps and *c*) polar caps emission using

in this case the spectra calculated by Zampieri *et al.* (1995). Once the shape of the emitted spectrum has been fixed, we have calculated the maximum value of v, $v_{\max}$, at which a star at the inner boundary of the Wall, d_1, produces a count rate above each chosen threshold. For each value of v, the star distance was varied between d_1 and 50 pc (the assumed outer boundary of the Wall for both models) in order to calculate the maximum distance, $d_2(v)$, at which such an object can be detected in the Wall. The star will be observable within a volume $V(v)$:

$$V(v) = 2\int_{l_1}^{l_2} dl \int_{\pi/3}^{\pi/2} \sin\theta d\theta \int_{d_1}^{d_2} r^2 dr = \frac{\alpha}{3}\left(d_2^3 - d_1^3\right) \tag{9.20}$$

where $d_1 = 16$ pc (model I) and $d_1 = 30$ pc (model II), $l_1 = 15°$, $l_2 = 120°$ and $\alpha = 1.83$ ster $\simeq 6000\,\mathrm{deg}^2$ is the angular size of the Wall. If $v_{\max}$ is larger then the sound speed, the predicted number of sources is found integrating dN/dv in the range $0 < v < v_{\max}$

$$N = n_0 V(c_s) G(c_s) + n_0 \int_{c_s}^{v_{\max}} V(v) \frac{dG}{dv} dv\,; \tag{9.21}$$

the integral was evaluated numerically, and $c_s = 10$ km/s was used.

Two distinct surveys, the All–Sky Survey (E–ASS) and the Deep Survey (E–DE) were conducted with the EUVE telescopes. Moreover observations with longer exposure times, the Right Angle Program (RAP, McDonald *et al.* 1994), allow the detection of sources with count rates down to 0.001 counts/s, so we repeated our calculations using also this limiting threshold. We have considered the two filters centered at higher frequencies, covering the wavelength range 58–364 A. However, in the following we will report only results for the Lex filter since our calculations in the AlC bandpass indicate that no sources are expected to be observable in this band. As for the observability with ROSAT, we focussed on the total band T of PSPC and WFC (see Table 9.1).

Table 9.5: **Expected number of detectable sources**

detector	bandpass	threshold (ct/s)	N[a]	N[b]	N[c]
EUVE ASS	Lex	0.01	2	7	1
EUVE DE	Lex	0.015	3	7	1
EUVE RAP	Lex	0.001	8	19	11
ROSAT WFC	S1	0.02	1	3	0
ROSAT WFC	S2	0.025	1	0	0
ROSAT PSPC	T	0.015	2	21	18
ROSAT PSPC	T	0.1	1	16	10
ROSAT PSPC	T	1.	0	5	2

[a] *Blackbody emission from the entire star surface.*

[b] *Blackbody emission from the polar caps,* $B = 10^9$.

[c] *Zampieri et al. (1995) spectra,* $B = 10^9$ *G.*

Taken from Zane et al. (1996b); Model I.

Above a sensitivity limit of 1.5×10^{-2} counts/s the R–ASS detected a very large number of sources toward the Galactic plane. However, if some ONSs are really present in the solar proximity, we expect that their emission persists at larger flux limits where the number of unidentified sources in the ROSAT survey is lower. For this reason we have repeated our calculations considering three different values for the threshold count rate: 1.5×10^{-2}, 0.1 and 1 counts/s. Results of model I are summarized in Table 9.5; model II gives a substantially similar picture. The optical counterparts of ONSs are very faint (TC, BM), so the relatively high count rate and the lack of optical identification of the X–ray sources will be a distinguishing criterion.

The numbers in the Table suggest that, in the assumption of blackbody emission, accreting ONSs could produce a non–negligible count rate in the UV band. Because the hardening of the spectra computed by Zampieri *et al.* is comparable to that induced by the presence of a magnetic field, we expect that, accounting for more realistic spectral properties, UV radiation could be detected even in the assumption of emission from the entire NS surface. In this case the number of detectable sources should be similar to the values of N^b in the Table. The highest number of detectable objects corresponds to the intermediate model in which only one source of hardening acts, either the reduced emitting area or the differential free–free absorption effect. Since in this case the spectrum is peaked in the EUV–soft X–ray bands and the LISM does not produce significant absorption at these energies, the count rates turn out to be larger than those produced by the Zampieri *et al.* spectra emitted from the polar caps, which are too hard to give a comparable contribution in the S band (0.2–0.4 keV) of ROSAT PSPC. However, we think that in a more plausible physical scenario both a non zero magnetic field and the effects of bremsstrahlung opacity should be accounted for.

Then, it follows that ONSs are, mainly, soft X–ray emitters (see the last columns in Table 9.5), although the EUV counterpart of very bright sources could be detected by EUVE in the Lex band at the limiting sensitivity thresholds, 0.01 counts/s; at the slightly higher sensitivity limit of 2×10^{-2} counts/s, the predicted number of sources is already zero. In this respect the RAP, improving the EUV sensitivity in pointed mode, seems to be the most profitable way to search for the EUV counterparts of ONSs. A detailed analysis of ROSAT PSPC ASS appears nevertheless the best approach for detecting ONSs in the Wall. In particular, being such sources very close, about 10 objects are expected to be observable with ROSAT PSPC above a sensitivity limit of 0.1 counts/s.

9.3.2.2 Comparison with Observational Data and Conclusions

In order to compare our predicted number of sources with the actual number of NOIDs observed so far in the direction of the Wall, we have performed a systematic analysis of the ROSAT WFC ASS Bright Source Catalogue (Pounds *et al.* 1993), the First EUVE Source Catalog (Bowyer *et al.* 1994), the EUVE Bright Source List (Malina *et al.* 1994), the EUVE RAP source list (McDonald *et al.* 1994) and the on–line catalogue of the ROSAT PSPC ASS public pointings (White, Giommi & Angelini 1994, WGA).

The WFC Bright Source Catalogue collects the observations of the ROSAT WFC telescope, which carried out the first almost complete survey of the UV sky (96%) in the 60–200 A wavelength band. In addition, the EUVE Bright Source List, the First EUVE Source Catalogue and the EUVE RAP source list contain the positive detections of sources in the E–ASS and E–DE. About 97 % of the sky has been covered in E–ASS, while the deep survey spanned only a small strip along the ecliptic plane. As discussed, relatively

soft spectra could produce a non–negligible EUV emission and it is therefore interesting to analyze the present available data in this band. Searching in the direction of the Wall, we found 5 sources without any counterpart within a circle of $3'$ above 0.02 counts/s in the EUVE Lex filter and 5 unidentified sources in both the S1 and S2 WFC filters; the EUVE RAP source list contain 4 new unidentified sources. WFC sources are not seen by EUVE. They are probably too soft to be ONSs, because their S2 count rate always exceeds the S1 one, at variance with what is expected for the majority of ONSs. We stress, however, that it cannot be ruled out that some of the faintest unidentified sources in E–ASS could be ONSs, if their emitted spectrum is soft enough (see Maoz, Ofek & Shemi 1997). In the case of blackbody emission from the polar caps, we have calculated that 4 sources can be detected in the Lex band above 0.02 counts/s which corresponds to 80 % of EUVE NOIDs. However, the E–ASS is far from being complete at a threshold of 0.02 counts/s ($\sim$ 3.5 % of the sky in the Lex band, Bowyer *et al.* 1994) and the five detected sources are an absolute lower limit for the total number of unidentified objects in the Wall. As a consequence, the number of NOIDs in the Wall is consistent with the expected number of ONSs in the EUV band.

The comparison with soft X–ray ROSAT observations has been performed on the basis of the WGA catalogue. We found that pointings in the WGA catalogue cover about 7% (414 $\deg^{-2}$) of the Wall, with a total number of $\sim$ 7000 detected sources. The number of objects observed within an offset angle $\leq 20'$ from the image center (where the sensitivity of the detector is maximum) is given in table 9.6 as a function of threshold. We note that, quite independently of the assumptions on the emitted spectrum, the total number of NOIDs is substantially larger than our estimated number of observable ONSs in the Wall.

Table 9.6: **WGA sources in the Wall direction as a function of threshold**

threshold (ct/s)	sources	source density (deg^{-2})	expected sources[a]	expected NOIDs[a]
0.015	469	3.25	19500	1500
0.1	132	0.91	5500	170
1.0	48	0.33	2000	30

[a] *density* × *total area of the Wall.*
Taken from Zane et al. (1996b).

It is particularly promising that, at a threshold of 0.1 counts/s, about 5% of NOIDs could be ONSs, when the emitted spectrum falls mainly within the ROSAT band. The search for relatively bright R–ASS sources in the Wall direction could be, therefore, a promising strategy for selecting ONSs candidates. Clearly, the number of NOIDs decreases with increasing flux limit. Although a slightly larger ONSs/NOIDs ratio is expected at higher flux limits ($\sim$ 1 count/s), the search for accreting NSs among such bright sources could be fruitless because the estimated number is so close to unity to be seriously biased by the uncertainties of the model. On the other hand, the choice of a lower sensitivity limit, $\sim$ 0.01 counts/s, does not provide a larger ONSs/NOIDs ratio, suggesting that 0.1 counts/s is indeed the most favorable threshold for identifying nearby accreting ONSs.

In the case of polar cap accretion with the spectrum calculated by Zampieri *et al.* , which seems the more realistic assumption, the emitted radiation is hard enough to give no detectable flux in the visual band, $m_V \gtrsim 29$. The absence of an optical counterpart would be, therefore, a primary identification criterion. The R–ASS candidates could be then searched for by E–DE in individual pointings. Finally, if these objects have some radio emission, as suggested by Treves, Colpi & Lipunov (1993), another distinguishing feature would be the high proper motion, $\sim$ 0.2 arcsec/yr assuming a velocity of 35 km/s and a distance of 30 pc. [1].

9.4 The Present Status of Observations

As we have seen in section 9.3, theoretical predictions about the detectability of single ONSs are rather optimistic. However, despite the intense observational efforts, the search for ONSs produced, up to now, just a handful of candidates. These cases concern serendipitous discoveries of ONS candidates in ROSAT PSPC observations and Einstein Extended Medium Sensitivity Survey (the first one): MS 0317.7-6647 (Stocke *et al.* 1995), RXJ 185635-3754 (Walter, Wolk & Neuhäuser 1996) and RX J0720.4-3125 (Haberl *et al.* 1996, 1997). Actually, out of them only the latter two seem indeed promising while the first identification is slightly ambiguous.

MS 0317.7-6647 is a very soft, weak ($\sim$ 0.03 counts/s) source in the field of the nearby galaxy NGC 1313, and it has been first discovered by Stocke *et al.* (1995). The only possible optical counterpart has $m_v = 20.8$, which brings the X to optical ratio to $f_x/f_v \gtrsim 60$. The

[1] We thank Stuart Bowyer for helpful discussions and the referee of the paper Zane *et al.* (1996b), Roger Malina, for bringing to our attention some recent EUVE data.

simultaneous lack of radio emission seems to rule out the possibility of an extreme BL Lac object leaving only a compact object as a reasonable option. The identification of the source with a HMXB in NGC 1313 leads to a luminosity $L \sim 10^{40}$ erg s^{-1} with an estimated mass of the compact object $\sim 50 M_{\odot}$. Although not impossible, the existence of such a massive stellar BH seems unplausible. The high Galactic latitude makes also the source unlikely to be an X–ray binary in our own Galaxy, so the accreting ONS hypothesis is the only left standing. This option is corroborated by the PSPC spectrum, which is well fitted by a blackbody at $T \sim 0.2$ keV, by the derived luminosity, which $L \sim 1.7 \times 10^{30}$ erg cm^{-3} placing the object at 100 pc and by the presence of a cirrus cloud at same position and at about the same distance.

RXJ 185635-3754 is a much brighter (3.62 ± 0.03 counts/s) source already detected by the EINSTEIN survey; it was first proposed as ONSs candidate by Walter, Wolk & Neuhäuser (1996). The observed spectrum is well fitted by a blackbody with $kT = 57 \pm 1$ eV and column density $N_H = 1.4 \pm 0.1 \times 10^{20}$ cm^{-2}; no emission was detected in other spectral bands. In the former analysis of the ROSAT data by Walter, Wolk & Neuhäuser, no obvious optical counterpart down to $m_v \sim 23$ was found, yielding a very large value of $f_x/f_v \gtrsim 7000$. Moreover, the source appears projected on the molecular cloud RCrA, that is estimated to be ~ 130 pc away (Dame *et al.* 1987), and the extinction derived from the X–ray data is less than the column density in the cloud itself. Basing only on absorption considerations, Walter, Wolk, & Neuhäuser concluded that the source is likely to be closer than RCrA and derived a luminosity $L \sim 5 \times 10^{31} (d/100\,\mathrm{pc})^2$ erg cm^{-3}. Later on, a more critical interpretation of the ROSAT data by Campana, Mereghetti & Sidoli (1996) pointed out that RXJ 185635-3754 does not coincide with the dense core of the cloud, but it lies

on a boundary, in a direction of much lower extinction. The optical absorption is $A_V \sim 0.7$ mag in the X–ray source direction, while $A_V \sim 3$ mag at the cloud core (Rossano 1978). As a consequence, it is not obvious that the source lies in front of RCrA; the new estimated distance was 170 pc, which places the source beyond the cloud. Rederiving the error box of RXJ 185635-3754, Campana *et al.* found that, even if several optical counterparts are positionally compatible with the X–ray source, they are limited to objects fainter than $g \sim 18$ (g is the g Gunn filter of the Danish 1.54 m telecope of the ESO, La Silla). This gives $f_x/f_v \gtrsim 20$, a value still high enough to rule out most classes of known X–ray emitters. The emerging picture is consistent with a slow ONS accreting in a region where $n \sim 1\,\mathrm{cm}^{-3}$.

RX J0720.4-3125, discovered by Haberl *et al.* (1996, 1997), is probably the best ONS candidate proposed up to now. It was first discovered in the ROSAT all–sky survey, during the Galactic Plane Survey, and then re–observed in a dedicated PSPC pointing. The count rate is 1.64 ± 0.04 counts/s, the best fit spectral model is a blackbody at $kT = 79 \pm 4$ eV, $N_H = 1.3 \times 10^{20}\,\mathrm{cm}^{-2}$ and the limit for f_x/f_v is more than 500. The similarities in the X–ray properties of RX J0720.4-3125, compared to RXJ 185635-3754 and the high value of f_x/f_v suggest it as a very likely candidate for ONS accreting the ISM. The low absorption rules out an extragalactic origin; the distance was estimated to be around 100 pc, with an upper limit $\sim$ 300 pc. This, in turn, limits the X–ray luminosity to about 10^{32} erg/s. In principle, the value of the f_x/f_v ratio may be consistent with a LMXB interpretation, since these systems are characterized by typical ratios of 100 – 1000 (White, Nagase & Parmar 1993). However, this is discarted by both the absence of large changes in the X–ray luminosity on time scales of years, and the fact that the inferred X–ray luminosity is order of magnitudes too low. Moreover, the NS interpretation is strengthened by the fact that

RX J0720.4-3125 is *pulsating*, with a periodic modulation at 8.3914 s. If interpreted as spin period, this pulsation is unlikely to come from a white dwarf (WD). In principle, in fact, a massive WD with this period could be stable (Chanmugam, Rao & Tohline 1987), but it should be in a binary system, spun up by accretion and, more important, visible in the optical as a cataclismic variable. An isolated WD accreting the ISM needs to be ~ 30 times closer than a NS to account for the X–ray flux, and also in this case it should be detected as an optical source. Moreover, there is another issue that makes RX J0720.4-3125 particularly interesting: it may represent the first detection that makes possible to improve the present understanding of the magnetic field and spin evolution of isolated NS (Wang 1997). In fact, the estimated X–ray luminosity and the pulse period allow to derive the value of the NS magnetic field, if the X–ray emission comes from accretion. Haberl *et al.* obtained $B \lesssim 10^{10}$ G. According to the idea that the field decay is strongly related with accretion, Haberl *et al.* proposed a scenario in which RX J0720.4-3125 comes from the evolution of a Thorne–Zytkow object, similar to that one proposed by Lorimer, Lyne & Anderson (1995) for low–velocity radio pulsars with low magnetic field. However, an old isolated NS evolved from a single star can not be ruled out from the magnetic field arguments (Haberl *et al.* 1997; Wang 1997). As pointed out by Wang (1997), an initial field of 10^{12} G and a decay timescale $\gtrsim 10^7$ yrs (power law decay) or $\gtrsim 10^8$ yrs (exponential decay) are consistent with the observed parameters and these times may be sufficient to spin down a fast rotating object to the period of RX J0720.4-3125.

Despite these sources, the low number of isolated neutron stars candidates from the ROSAT all–sky surveys remains to be explained. The discrepancy between the estimates for the number of ONSs potentially detectable and the observations is further strengthened

by upper limits derived from nearly complete identifications of area–selected survey sources. Recent analyses of ROSAT fields in the Galactic plane (Danner 1996) and in the direction of GMCs (Belloni, Zampieri, & Campana 1997; Motch *et al.* 1997; Danner 1996), placed rather stringent constraints on the number of ONSs in ROSAT images. Belloni, Zampieri & Campana (1997) have performed a systematic search for ONSs in two molecular clouds in Cygnus, Rift and OB7, analyzing archive ROSAT PSPC pointings. Observations cover only a small fraction of the clouds, $\sim 5\%$, and the expected number of ONSs detectable above threshold is ~ 10 in both Rift and OB7, the actual number depending on threshold. ROSAT pointings contain 109 sources. For 105 of them an optical counterpart was identified either on the GSC or DSS, leaving 4 NOIDs, with no counterpart above $m_r \sim 20$. Although presently inferred values of $f_x/f_v \sim 1$ are not large enough to quality these sources as strong ONSs candidates, their positional coincidence with dense clouds together with their hardness ratio $\gtrsim 0.3$ make them worth of future investigations.

A larger sample region in Cygnus, $\sim 64.5\,\mathrm{deg}^2$, comprising a large part of the cloud OB7, has been investigated in detail by Motch *et al.* (1997). using R–ASS data. The survey is complete at about 0.02 counts/s and, at this flux level, 68 sources are detected. Catalogue searches and optical follow–up observations have shown that the vast majority of these sources are associated with active coronae (F–K and M stars). There are 8 NOIDs and they do not seem to be correlated with the denser phases of the ISM.

It should be stressed that, in both cases, the observed number of NOIDs is $\lesssim$ the predicted number of ONSs ($\gtrsim 10$ above 0.02 counts/s in the Motch field, according to Zane *et al.* 1995). However, these fields represent sites where accretion should be most effective and the resulting numbers seem to suggest an excess in the current theoretical predictions

of a factor $\sim 5 - 10$. On the other hand, it was already pointed out by Zane *et al.* (1995) that the most favorable models produce a source density of ~ 10 deg^{-2} which is too close to the average density of NOIDs in ROSAT PSPC pointings, ~ 30 deg^{-2}.

9.5 The Diffuse X–Ray Emission

The observational impact of the X–ray emission from isolated ONSs is not restricted to the detection of individual sources. Despite their intrinsic weakness, in fact, they could provide a contribution to the diffuse X–ray background (XRB), being their total number very large. This point, originally suggested by Ostriker, Rees & Silk (1970), was addressed by BM who concluded that the integrated flux form ONSs above 0.5 keV is negligible in the hypothesis of blackbody emission. Further interest in the collective ONSs emission was aroused by the paper of Hasinger *et al.* (1993). By carrying out a detailed analysis of 27 fields at high galactic latitude, $|b| \geq 30°$, these authors found that, at the faintest flux limit of ROSAT, about 60 % of the background is resolved into extragalactic discrete sources (see also Comastri *et al.* 1995). Their flux is 1.48×10^{-8}erg cm^{-2}s^{-1}sr^{-1} in the 0.5–2 keV band over a total flux $F_{XRB} = 2.47 \times 10^{-8}$erg cm^{-2}s^{-1}sr^{-1} in the same energy band. The projected number density of resolved sources turns out to be 413 deg^{-2}, which exceeds by about 60 % the density of QSOs predicted by standard evolutionary models. Even assuming that at the same flux limit the contribution of stars is $\sim$ 10 %, about 120 sources deg^{-2} remain to be explained, together with $\sim$ 40% of the XRB (soft excess). As noted by Hasinger *et al.* , these results can be interpreted either by a more complicated model for the evolution of the QSOs X–ray luminosity function or invoking the presence

of a new population of sources. An important point emerging from ROSAT observations that sets constraints on the nature of the new population is that the average spectrum of resolved sources becomes harder at lower flux limits.

Although such a population may be extragalactic in origin, Maoz & Grindlay (1995) showed that its properties are compatible with those of Galactic objects and tentatively identified them with Cataclysmic Variables (CVs). As they pointed out, objects with a typical X–ray luminosity $\sim 10^{30}$ erg/s, and with a local density of $\sim 10^{-4} - 10^{-5}$ pc^{-3} could explain a substantial fraction, 20–40 %, of the XRB, giving, at the same time, the required source density and soothing the problem of the observed number sources excess. Assuming a blackbody spectrum at the star effective temperature, and assuming that the population is composed of standard candles of fixed luminosity, accreting ONSs were ruled out as possible candidates by Maoz & Grindlay on the basis of their too soft emission. The role of the magnetic field which drastically diminishes the emitting area, and the harder spectra obtained from our calculations, together with their hardening with decreasing luminosity, lead us to recompute the ONSs contribution. A thorough model has been presented in Zane *et al.* (1995), using the numerical results for the star distribution f, a detailed map of the ISM and synthetic spectra. We showed that the ONSs contribution to the XRB, averaged over all latitudes, can be as high as 10%, and 5–6 % at the high latitudes considered by Hasinger *et al.* and Maoz & Grindlay. This corresponds to 12–25% of the observed soft excess. At the sensitivity limit of the deep survey of Hasinger *et al.* (2×10^{-4} counts s^{-1}) the number density of resolved sources, averaged over all latitudes, is $\sim$ 20 deg^{-2}, which amounts to $\sim$ 17 % of the unexplained non–QSOs, non–stellar component. Actually, the strongest constraint on this scenario follows from the expected number of sources above the

higher threshold of 10^{-3} counts s^{-1}. From a direct analysis of the on line catalogue of the ROSAT PSPC pointings (ROSATSRC), we found that the mean number of sources detected with flux larger than 10^{-3} counts s^{-1} ($\sim 10^{-14}$ erg $cm^{-2}s^{-1}$), is $\sim 30\,deg^{-2}$ ($b < 30°$) and $\sim 40\,deg^{-2}$ ($b > 30°$). Despite this result is formally in agreement with the mean number of unidentified sources predicted by our model at the same flux limit, $\sim 10\,deg^{-2}$, it is apparent that the two numbers turns out to be too close.[2]

Clearly, the diffuse emissivity of accreting ONSs depends on their spatial concentration and on the density of the interstellar medium. For this reason it is of particular interest to consider accretion onto NS remnants in the Galactic Center, that is a site where both the stellar and gas densities exceed by orders of magnitude those of other regions of the Galaxy. At the same time the Galactic Center is a well known source of diffuse X–ray emission, first detected by *Uhuru* (Kellogg *et al.* 1971) and then studied by virtually all X–ray missions. In the light of this, we have recently analized the possible association of the Galactic Center diffuse X–ray source with accreting ONSs (Zane, Turolla, & Treves 1996; see also Maraschi, Treves, & Tarenghi 1973). The next subsections are devoted to the presentation of these results. Because of the peculiarity of the Galactic Center region (see e.g. Morris & Serabyn 1996; Genzel, Hollenbach & Townes 1994 for extended reviews), the discussion will be slightly more detailed with respect to that one presented in the rest of this Chapter. First, we review the X–ray observations of the Galactic Center. We then discuss the interstellar medium, the stellar and the expected neutron star distributions.

[2]We thank the referee of the paper Zane *et al.* (1995), Piero Madau, for some useful and constructive comments on the manuscript, Michiel van der Klis for stimulating discussions and Tomaso Belloni for his help in extracting data from ROSATSRC.

The calculation of the emission due to accreting ONSs is finally presented and our results are compared with observational data. Discussion follows.

9.5.1 The Diffuse X–Ray Source at The Galactic Center

The Galactic Center is one of the most widely explored regions of the sky in the X–rays and observational efforts appear indeed motivated in the light of the complexity of the source. The inner 100 pc of the Galaxy exhibit, in fact, a region of diffuse emission together with a number of point–like sources. The strong absorption in the direction of the Galactic Center makes its appearance substantially dependent on the energy band (soft or medium X–rays) in which the source is observed. Here we briefly outline the current status of X–ray observations of the Galactic Center, focussing our attention on the diffuse component.

The presence of a weak, diffuse emission from about $\sim$ 1 deg^2 was already suspected in the *Uhuru* 2–10 keV data (Kellogg *et al.* 1971) and first confirmed by *Einstein* in the 0.5–4 keV band (Watson *et al.* 1981). Observations with 10′ resolution in the 2–15 keV range, performed with *Spartan 1* (Kawai *et al.* 1988) and *Spacelab 2* (Skinner *et al.* 1987; Skinner 1989), confirmed the diffuse emission at higher energies. Spectral measurements by *Ginga*, with an angular resolution of $\sim 1°$, have shown the presence of a strong emission line at 6.7 keV, which was identified with the Kα line of He–like iron (Koyama *et al.* 1989; Yamauchi *et al.* 1990). The continuum appears rather flat and is well fitted by a thermal bremsstrahlung. A temperature of 12.7 ± 0.4 keV was calculated on the basis of TTM observations by Nottingham *et al.* (1993). Such temperature, however, is more than one order of magnitude too high for a plasma to be confined in the Galactic Centre potential well.

The ART–P telescope on board *Granat* observed the Galactic Center region with 5′ resolution in the 2.5–30 keV band with rather long exposure times (Sunyaev, Markevitch, & Pavlinsky 1993; Markevitch, Sunyaev, & Pavlinsky 1993). The intensity profiles obtained in 4 energy bands, after subtracting point–like sources, show the presence of an elliptical, extended source, as first suggested by Kawai *et al.* Spectra from the total $1° \times 1.5°$ ellipse and from a central region 30′ wide were produced, confirming a flat bremsstrahlung–like continuum; a strong absorption feature at 8–11 keV was also detected. Sunyaev, Markevitch, & Pavlinsky (1993) noted that the structure of the diffuse emission differs substantially below and above $\sim$ 8 keV. While the lower energy component is thermal and roughly elliptical, the hard emission comes from an elongated region, parallel to the Galactic plane, that resembles the distribution of Giant Molecular Clouds. This led Sunyaev, Markevitch, & Pavlinsky to the conclusion that the diffuse emission consists of two components and that the high energy portion of the spectrum may be due to Thomson scattering of hard photons on the dense material of the clouds. In this picture the bremsstrahlung temperature could be lower than the previous estimate (Markevitch, Sunyaev, & Pavlinsky give $T_{brems} \sim 3$ keV), easing the problem of confining the hot gas in the Galactic Center.

The best resolution X–ray map of the Galactic Center was obtained with *ROSAT* in the 0.8–2 keV range (Predehl & Trümper 1994). In order to explain the lack of X–ray sources at the position of Sgr A*, an interstellar absorption higher than 2×10^{23} cm^{-2} was invoked by Predehl & Trümper. Preliminary reports of ASCA observations (Koyama *et al.* 1996) indicate the presence of several metal lines besides iron. In particular, a 6.4 keV fluorescent Kα component appears superposed to the 6.7 keV emission feature.

9.5.2 The Gas Distribution

The structure of the interstellar medium (ISM) in the central 10^2 parsecs of the Galaxy has been extensively investigated and a detailed review can be found in Genzel, Hollenbach & Townes (1994). Informations about the dust distribution are obtained from the re-radiation of UV and visible photons into the infrared continuum, atomic and ionized components are observed directly in the 21-cm line while the more abundant molecular gas is sampled by the millimetre, submillimetre and infrared lines of trace molecules (CO, OH, HCN, ...). The resulting picture shows that the Galactic Center is a region characterized by a strong concentration of dense interstellar material, with an average density of gas and dust 10^2-10^5 times higher than in the rest of the Galaxy. The central 5 parsecs contain a circum-nuclear disk (CND) of orbiting filaments and streamers with its inner edge at $\sim$ 1.5 pc from the center. This disk is probably fed by the infalling gas from denser molecular clouds at $r \gtrsim$ 10 pc and drops streamers in the central region. The inner region ($r \lesssim$ 1.5 parsecs: the central cavity and the mini-spiral) are comparatively devoid of material and the average gas density is, at least, one order of magnitude lower than in the CND. On larger scales, surveys of 2.6 mm CO and far-infrared dust emission with *IRAS* (Dame *et al.* 1987, Deul & Burton 1988) show that $\sim 10^8\, M_\odot$ of gas ($\sim$ 10% of the total Galactic ISM) are contained in the inner few hundred parsecs. Using a new CO-to-H_2 conversion factor, Sofue (1995a) estimated a value for the gas mass of $\sim 4.6 \times 10^7\, M_\odot$ within $\varpi \sim 150$ pc, where ϖ is the distance from the center in the plane of the sky. The corresponding average gas density turns out to be ~ 100 cm^{-3}, in agreement with the value reported by Genzel, Hollenbach & Townes (1994) for the inner 100 pc. The total mass of gas and dust is only 1-10% of the stellar mass and does not contribute significantly to the Galactic gravitational potential. The dust

comprises only about 1% of the ISM mass which is mainly in the form of molecular, atomic and ionized gas. A fraction of the interstellar material is organized in dense molecular clouds and macro–structures: within $\sim$ 500 pc the filling factor is $\sim$ 10% for clouds with $n \sim 10^3$ cm^{-3} and $\sim$ 0.05% for clouds with $n \sim 10^5$ cm^{-3} (see, e.g., Campana & Mereghetti 1993 for a discussion). As recently discussed by Sofue (1995a), the gas distribution in the central $\sim$ 1 kpc region is dominated by a rotating ring with $n \approx 10^3$ cm^{-3} located at $\sim$ 120 pc while the gas density drops by one order of magnitude outside. An expanding, roughly spheroidal, molecular shell is also observed at $r \sim 180$ pc, $|z| \lesssim 50$ pc, with the gas mainly concentrated at intermediate latitudes (Sofue 1995b).

Using *IRAS* observations of the $3^\circ \times 2^\circ$ region around Sgr A, Cox & Laureijs (1989) proposed that the dependence of the gas mass on the projected distance from the Galactic Center is

$$m_{gas}(< \varpi) \sim 2 \times 10^3 \varpi^{1.8} M_\odot \,. \tag{9.22}$$

Such distribution holds approximately up to 300 pc from the center and implies, on such scales, a nearly constant surface density. As discussed by Cox & Laureijs, this result is very sensitive to the assumed dust temperature and the value of the total gas mass is correct to about 30 % within 300 pc (50 % at larger distances). Clearly, the averaged volume density profile can be derived only by de–projection and any distribution matching the constraint of constant surface density is a priori acceptable. In particular, if the extension of the gas along the line of sight is roughly constant when ϖ varies, it is not unreasonable to assume an homogeneous gas distribution with an averaged, constant value for n. Within 225 pc, the averaged value of n derived from *IRAS* data is $\sim$ 60 cm^{-3}, assuming an elliptical gas distribution with an axial ratio 0.7 and using a value of $3.6 \times 10^7 M_\odot$ for the total mass (Cox

& Laureijs). However, in the inner $\sim$ 100 pc this value is probably an underestimate (see the previous discussion) and $n = 10^2$ cm^{-3} seems to be closer to observations. For these reasons, in our calculation of the contribution of accreting ONSs to the diffuse emission from the Galactic Center, the accretion rate will be estimated assuming an homogeneous distribution of the ISM with

$$n = 100\,\mathrm{cm}^{-3} \qquad \varpi < 100\,\mathrm{pc}\,. \tag{9.23}$$

Outside this region, in order to correct the X–ray emission for interstellar absorption, we need an estimate of the gas density in the Galaxy. This is known to be of order unit and is a parameter in our model, adjusted in such a way to give a total column density, integrated over 8.5 kpc at $z = 0$, always greater that $N_H = 2 \times 10^{23}$ cm^{-2}. As discussed by Predehl & Trümper (1994), such a large value of N_H appears compelling if the deficit of X–rays sources observed by *ROSAT* toward Sgr A* has to be accounted for.

9.5.3 The Star Distribution

Both observations and theory (see e.g. Bailey 1980; Allen, Hyland, & Hillier 1983; Sanders 1989; Morris 1993) provide convincing evidence that in a very large range of Galactocentric distances, from few arcseconds to few degrees from the center, the star volume density scales approximately as r^{-2} (r is the galactocentric spherical radius) in agreement with the prediction of the isothermal cluster model for the region outside the core radius a. The value of the core radius derived from observations ranges between $\sim$ 0.04 and $\sim$ 0.8 pc (see e.g. Morris 1993; Genzel, Hollenbach & Townes 1994 and references therein). Within the core radius, data derived from the dynamics of both the stellar and gas components agree quite well in suggesting that an additional dark mass of $\sim 3 \times 10^6\, M_\odot$ is present in the

central region. This mass could be in the form of either a single, massive black hole or, if the central density is not in excess of $10^8 M_\odot$ pc^{-3}, a cluster of many compact remnants (Morris 1993; Genzel, Hollenbach & Townes 1994). According to this picture, the mass volume density of the stellar component is given by

$$\varrho(r) = \varrho_c r^{-1.8} M_\odot \mathrm{pc}^{-3}, \tag{9.24}$$

where ϱ_c is the central density which can be inferred from the estimated mass inside the core radius; typical values for ϱ_c are a few $10^5 M_\odot$ pc^{-3} (Sanders 1989; Morris 1993). In the following we assume that this profile adequately describes the stellar distribution in the region beyond 1 pc from the Galactic Center and we take $\varrho_c = 4 \times 10^5 M_\odot$ pc^{-3}.

The fraction f_{NS} of the total mass comprised in neutron star is a free parameter of our model and we assume that all neutron stars have the same mass, $M_* = 1.4 M_\odot$. For a Salpeter initial mass function (IMF)

$$N(M) \propto M^{-\alpha} \tag{9.25}$$

with $\alpha = 2.35$ and assuming that all stars with initial masses between $\sim 10 M_\odot$ and $\sim 50 M_\odot$ have left neutron stars, f_{NS} turns out to be ~ 1 %. With a fixed α, the previous formula can be assumed to describe the IMF of an already formed galaxy for masses in a given range, so possible differences due to the evolution of the bulge in the early Galactic history are ignored. However, as suggested by Morris (1993), the initial mass function for stars formed in the Galactic Center may be quite different from that averaged over the disk of the Galaxy, due to the different physical conditions in the star–forming clouds. In particular, throughout most of the central region, strong tidal forces increase the value of the limiting density for a cloud to become self–gravitating and this, in turn, acts toward inhibiting star

formation. This implies also that close to the center self-gravitating clouds are more and more unlikely to be present and that those in which the density is above the tidal limit are presumably supported by the strong magnetic pressure. Large internal velocity dispersions and higher temperatures within the clouds tend to increase the Jeans mass up to an order of magnitude with respect to the typical value in the rest of the Galaxy. In the inner few parsecs the most effective way of forming stars seems to be external cloud compression due to collisions with other clouds and/or with shock fronts produced by supernova explosions and other forms of nuclear activity. During the compression the gas temperature and the value of the Jeans mass are increased. Basing on these arguments Loose, Krügel, & Tutukov (1982) argued that the mass spectrum in the Galactic Center is probably skewed toward higher masses, with a lower cutoff at $M_{min} \sim 1 - 3M_{\odot}$ ($M_{min} = 0.08M_{\odot}$ is often assumed in the disk). In addition, the value of α itself turns out to be smaller than in the disk. so $f_{NS} = 0.01$ should be regarded as a lower limit. Corrections due to the effects of dynamical friction over the lifetime of the Galaxy have been considered by Morris (1993), but they have not been included here since they are more relevant for black holes due to their larger masses. Black hole remnants are expected to dominate the central cluster and their total mass is a large fraction of the dynamically inferred one. On the other hand, since mass segregation is not expected to modify strongly the distribution of neutron stars remnants. in the following we will use a number density of neutron stars given, outside the core radius. by

$$n(r) = f_{NS}\frac{\varrho_c}{M_*}r^{-1.8}\,\mathrm{pc}^{-3}\,. \tag{9.26}$$

The last ingredient we need in order to estimate the cumulative emission associated with the NS population is their velocity distribution $f(v)$. The approach previously discussed. in

which $f(v)$ is obtained assuming a suitable distribution of NSs at birth in phase–space and following the evolution of a large number of orbits in the Galactic gravitational potential, proved very useful in calculating $f(v)$ on large scales. However, due to the particular conditions of the Galactic Center, results obtained from a detailed analysis are not necessarily more correct than a simpler estimate. As discussed by Sellgren *et al.* (1990, see also Genzel, Hollenbach & Townes 1994), the velocity dispersion σ_v for low–mass stars in the central region is nearly constant between 0.6 pc and 100 pc, with $\sigma_v \sim 75$ km/s. At very small r observational data indicate that σ_v increases up to ~ 125 km/s. Here we assume that NS remnants were able to reach energy equipartition with the field stars, establishing a Maxwellian distribution

$$f(v) = \frac{x^2}{v_0} \exp\left(-3x^2/2\right) , \tag{9.27}$$

where $x = v/v_0$, $v_0 = \sigma_v$ and typical values for σ_v are in the range $75 - 125$ km/s. For a typical mass of $\sim 1 M_\odot$, it can be easily shown that the relaxation time t_{relax} (see e.g. Binney & Tremaine 1987) is $\lesssim 10^{10}$ yr in the inner ~ 10 pc. Since t_{relax} is a measure of the time required for deviations from a Maxwellian distribution to be significantly decreased, in the innermost region our hypothesis is justified. Energy equipartition between populations of different mass is reached in about the same time. In addition, the evaporation time turns out to be $\gtrsim 10^{10}$ yr for $r \lesssim 10$ pc, so the irreversible leakage of stars from the system due to stellar encounters is negligible over the Galaxy lifetime. A similar approach was used by Morris (1993) for the velocity distribution of the central cluster of black hole remnants. Extending the Maxwellian assumption up to ~ 100 pc is motivated on the basis of observational data. The total mass scales approximately as r here and, as previously discussed, this is just what is expected in an isothermal cluster model. Actually, a lowered

Maxwellian distribution is probably more reasonable, but the correction in the high energy tail (above $\sim v_{esc} \sim 2\sigma_v$) is not very important as far as the fraction of accreting ONSs is concerned, and will be not included in our calculations.

9.5.4 Results

Using the NS and gas distributions considered in the previous subsections, we can estimate the contribution of the neutron star population to the diffuse emission near the Galactic Center. We assume that the emitted spectrum is that calculated by Zampieri *et al.* (1995) and that ONSs have a relic magnetic field $B = 10^9 - 10^{10}$ G. Under these assumptions, the emission of medium X–rays ($\sim 4 - 5$ keV) is possible in the dense region of the Galactic Center.

The monochromatic flux emitted by ONSs in a region of volume V centered at $r = 0$ can be calculated from the expression

$$F_\nu = \int_V n(r)\,\varpi d\varpi dz d\phi \int_0^\infty f(v)\,\frac{\tilde{L}_\nu}{4\pi R^2} dv \quad \mathrm{erg\,cm^{-2}\,s^{-1}}\,, \tag{9.28}$$

where $\tilde{L}_\nu$ is the monochromatic luminosity at the source corrected for the interstellar absorption. In the previous expression the volume element is expressed in terms of the cylindrical coordinates (ϖ, z, ϕ): z is along the line of sight and ϖ has been defined in subsection 9.5.2. $R_0 = 8.5$ kpc and $R = (R_0^2 + \varpi^2 - 2R_0 z + z^2)^{1/2}$ are the distance of the Galactic Center and of the star from the Sun. The integral in equation (9.28) has been evaluated for $|z| \leq z_{max}$ and for different values of ϖ_{max}. *IRAS* data discussed in section 9.5.2 show that the dense material extends for a few hundred parsecs around the center, so we assume $z_{max} = 300$ pc. The unabsorbed monochromatic flux at the source depends on the accretion rate which, in turn, is a function of v and n. To avoid the direct calculation of the spectrum for each

value of the parameters within the multiple integral, we have computed a set of models for different values of $\dot{M}$. The spectral distribution corresponding to any given pair of values of v and n is then obtained by spline interpolation. The total emitted flux and the total flux for square degree in a fixed energy band are calculated integrating equation (9.28) over frequencies. All multiple integrals have been evaluated numerically and the cross sections for the interstellar absorption has been taken from Morrison & McCammon (1983).

The region within $\sim$ 1 pc from the center (central cavity), where our assumed star and gas distributions cease to be valid, has been excluded from the integration domain in all models. The X–ray emission from accretion onto collapsed objects in the cavity under hypotheses similar to our has been recently estimated by Haller *et al.* (1996) and turns out to be completely negligible.

Results of model calculations are compared with *Granat* ART–P observations. As discussed in subsection 9.5.1, the diffuse emission detected by *Granat* in the 2.5–8.5 keV band comes from a roughly elliptical region of $\sim$ 1.18 deg^2 around Sgr A*. The values of the observed total flux reported by Sunyaev, Markevitch, & Pavlinsky (1993) are $4.8 \pm 1 \times 10^{-10}$ ergs cm^{-2} s^{-1} and $4.6 \pm 1.3 \times 10^{-10}$ ergs cm^{-2} s^{-1} in the two energy bands 2.5–8.5 keV and 8.5–22 keV. For the sake of simplicity, we approximate the total ellipse with a circle of the same area, centered at $r = 0$. We then calculate the expected X–ray flux in the two spectral bands, varying B, v_0 and N_H. The fraction f_{NS} of neutron stars is always taken equal to 0.01; obviously fluxes scale linearly with f_{NS}. Results are reported in table 9.7.

As can be seen, the flux emitted above 8.5 keV never exceeds a few percent of the observed one, so accreting ONSs can not be directly responsible for the detected hard X–ray emission. On the contrary, the contribution of ONSs in the lower energy band can be

Table 9.7: **Computed fluxes for different parameter values**

v_0	N_H	B	$F_{[2.5-8.5]}$	$F_{[8.5-22]}$
km s^{-1}	10^{23} cm^{-2}	G	10^{-10} erg cm^{-2} s^{-1}	10^{-10} erg cm^{-2} s^{-1}
75	2	10^9	7.11	0.071
75	3	10^9	3.90	0.064
75	4	10^9	2.44	0.057
100	2	10^9	3.18	0.031
100	2.5	10^9	2.30	0.030
100	3	10^9	1.74	0.028
100	3.5	10^9	1.36	0.027
100	4	10^9	1.09	0.025
125	2	10^9	1.68	0.017
125	3	10^9	0.92	0.015
125	4	10^9	0.57	0.013
150	2	10^9	0.99	0.010
100	2	10^{10}	7.80	0.151
100	3	10^{10}	4.61	0.135
100	4	10^{10}	3.03	0.121
200	2	10^{10}	1.05	0.020
300	2	10^{10}	0.32	0.006

$f_{NS} = 10^{-2}$, $a = 1$ pc, $z_{max} = 300$ pc.
Taken from Zane, Turolla, & Treves (1996).

substantial. For the two values of B we have considered, the expected emission ranges from a minimum of 0.07 up to $\sim$ 1.6 the *Granat* flux in the 2.5–8.5 keV band. Clearly, this kind of calculation is necessarily influenced by the uncertainties in the assumed ISM and ONSs distributions. However, allowing for different values of the ONSs mean velocity and of the total column density, computed values are always comparable with observational data. In addition, while it could be not unreasonable to assume higher mean velocities for the NSs population (see e.g. Lyne & Lorimer 1994; Haller *et al.* 1996), the range of column densities we have explored corresponds to the higher values for the interstellar absorption toward the Galactic Center reported in the literature (see e.g. Thomas *et al.* 1996). Moreover the fraction f_{NS} of neutron star has been fixed to a rather conservative (low) value. All these considerations suggest that the ONSs contribution to the diffuse X–ray emission from the Galactic Center can be substantial in the low energy component.

We note that the ONSs integrated luminosity is typically $\gtrsim 10^{38}$ erg s^{-1} and that most of the radiation is in soft X–rays. This may prove of importance in the discussion of the heating and dynamics of the ISM in the central region of the Galaxy.

The spectrum of the diffuse emission from both the total $1^\circ \times 1.5^\circ$ ellipse and a smaller circle $30'$ in diameter has been obtained by Markevitch, Sunyaev, & Pavlinsky (1993). For the sake of comparison, we have calculated the monochromatic flux from these two regions using equation (9.28). Results are presented in figures 9.1 and 9.2 for three sets of parameter values. Crosses in figures 9.1 and 9.2 are the *Granat* data with their error bars. As can be seen, the observed spectral distribution is flatter than the predicted one, but the spectral shape is reasonably reproduced up to 6–7 keV. Other physical processes should be invoked to explain the harder emission.

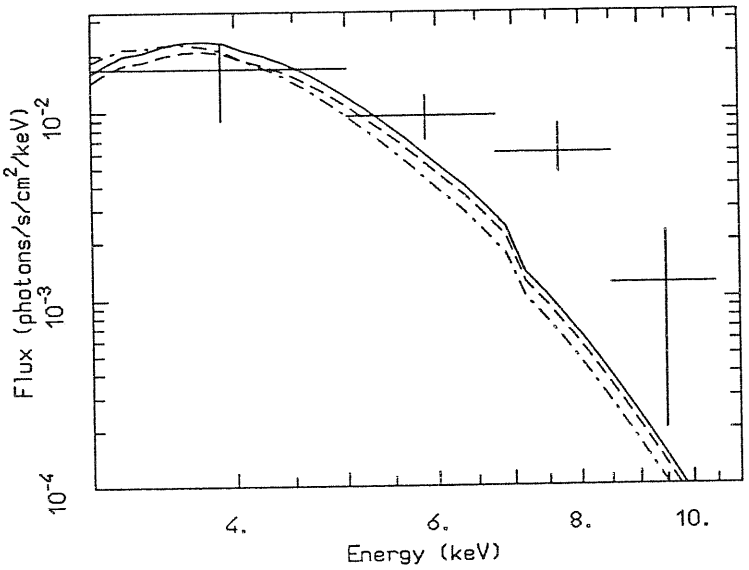

Figure 9.1: *Granat ART-P data (Markevitch, Sunyaev, & Pavlinski 1995, crosses) and calculated X-ray spectra from a region of 1.18 deg² for: a) $f_{NS} = 0.01$, $v_0 = 75$ km/s and $N_H = 3 \times 10^{23}$ cm^{-2} (solid line); b) $f_{NS} = 0.02$, $v_0 = 100$ km/s and $N_H = 3 \times 10^{23}$ cm^{-2} (dashed line); c) $f_{NS} = 0.015$, $v_0 = 100$ km/s and $N_H = 2.5 \times 10^{23}$ cm^{-2} (dash-dotted line). For all models $B = 10^9$ G. Taken from Zane, Turolla, & Treves (1996).*

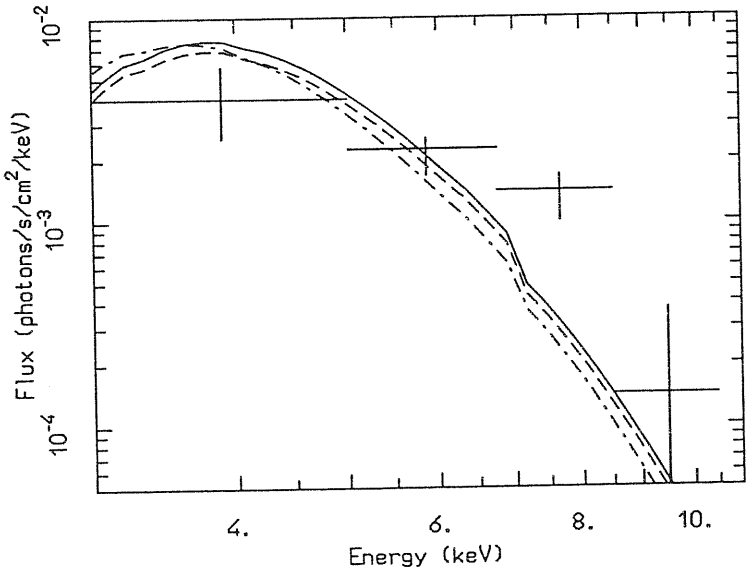

Figure 9.2: *Same as in figure 9.1 for the central region 30′ in diameter. Taken from Zane, Turolla, & Treves (1996).*

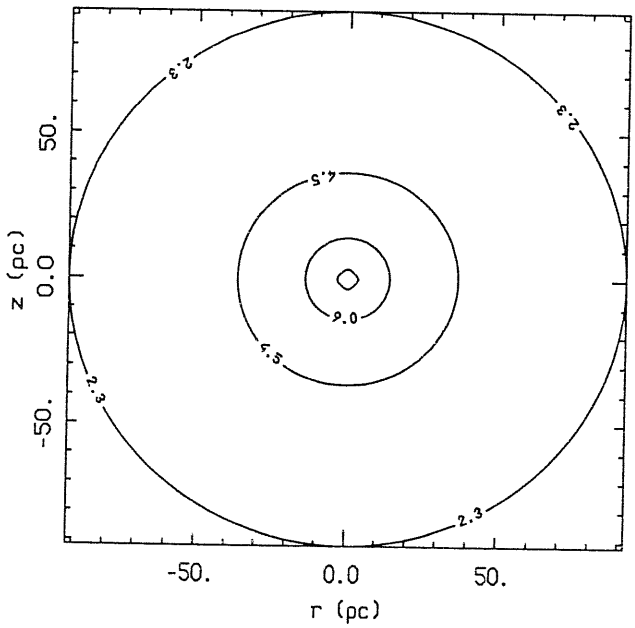

Figure 9.3: *Contour levels of the X–ray flux/deg^2 in the 2.5–5 keV band. Parameters values are* $B = 10^9$ *G,* $f_{NS} = 0.01$, $v_0 = 75$ *km/s and* $N_H = 3 \times 10^{23}$ cm^{-2}. *Taken from Zane, Turolla, & Treves (1996).*

We have compared the radial distribution of the emitted flux with available observational data. From the central 30′ region we expect approximately 34% of the total flux. This fraction should be compared with the $\sim$ 25% deduced from *Granat* data. The two values are in rough agreement although the radial distribution of the diffuse emission predicted by our simplified model appears more concentrated toward the center than the observed one. Figure 9.3 shows the contour levels of the X–ray flux per square degree, normalized to the total, in the 2.5–5 keV band. As a final point, we note that accretion onto ONSs produces an extremely smooth X–ray source in our model. In fact, the neutron star with the highest accretion rate contributes only to 3×10^{-4} of the total X–ray luminosity.

9.5.5 Discussion

As we shown, the 2.5–7 keV component of the diffuse X–ray source observed in the direction of the Galactic Center may be due to the unresolved emission from old neutron stars accreting the interstellar medium near the Galactic Center. Due to the large gas and stellar densities, the central region of the Galaxy appears, in fact, a very promising site to detect the overall emission from accreting ONSs. We have shown that a sizable fraction, possibly most, of the 2.5–7 keV emission may be explained in terms of an old neutron star population accreting the dense ISM. Because of the intrinsic uncertainties in our assumptions, mainly in the value of the neutron star relic magnetic field and in the star velocity distribution, it is not possible to assess firmly that ONSs are responsible for the extended X–ray emission in this band. Moreover, as we discussed in detail in this Chapter, accretion itself onto magnetized neutron stars could be questionable. Modulo these caveats, our calculations show that the observed intensity, spectral shape and flux radial dependence are substantially well reproduced for different values of the free parameters of the model. Above $\sim 6-7$ keV the integrated ONSs spectrum gives only a marginal contribution to the observed flux.

The calculated continuum is rather flat and then drops sharply above ~ 6 keV, so we do not expect that ONSs emission could provide an important photoionization source to produce ultimately iron lines. However, our synthetic spectra were computed considering only pure hydrogen atmospheres around accreting neutron stars. A definite assessment about the presence of Kα lines in the emerging spectrum would require the extension of our model to include line processes and a more realistic chemical composition for the accreting gas. If accretion onto neutron stars with a magnetic field as high as $\sim 10^{12}$ G is possible (which is dubious, see, e.g., Treves, Colpi, & Lipunov 1993), at high luminosities about 10

% of the flux is emitted in the cyclotron line at $E_B = 11.6 B_{12}$ keV (Nelson *et al.* 1995) and the excitation of the Fe lines could be substantial.

Sunyaev, Markevitch, & Pavlinsky (1993) noticed some correlation between the distribution of giant molecular clouds and the X–ray brightness and interpreted it as a signature of the reprocessing of medium energy photons by the clouds themselves. Such a correlation is naturally explained in our scenario, since GMCs provide regions of very high density in which the accretion rate can be substantially higher than our present estimate, based on $n = 100$ cm^{-3}. This implies also harder spectra, so that the emission of hard photons, ~ 10 keV, is possible for ONSs accreting in clouds with $n \sim 10^4$ cm^{-3}. On this regard, see the discussion of Campana & Mereghetti (1993) on the source 1740.7-2942.

Finally, we outline that the correlation between X–ray emission and the ISM distribution may become the basic probe to test the real relevance of ONSs accretion in explaining the diffuse X–ray source in the Galactic Center; AXAF and JET–X will have the required sensitivity and space resolution in medium energy X–rays to shed light on this important issue.

9.6 Concluding Remarks

In the standard models, the estimated number of detectable ONSs turns out to be large enough to expect that these sources have already appeared as unidentified sources in the current EUV, X–ray surveys and pointed observations, and a series of selection criteria should be enable to guide their identification. Their discovery would be of unprecedented importance, since it would provide some insights on the magnetic field and spin evolution,

and set constraints on the statistical and collective properties of ONSs. However, although intense observational champaigns are still in progress, at present the low number of isolated neutron star candidates in the ROSAT All–sky survey remains to be explained. If the preliminary upper limits derived from optical identifications of ROSAT survey sources (e.g. Motch *et al.* 1997) will be confirmed, some hypothesis underlying the standard estimates of the observability of accreting ONSs should be critically reviewed.

As discussed at the beginning of this Chapter, all published estimates on the observability of ONSs relies on several physical hypotheses and a series of uncertainties may alter the theoretical predictions: we shall conclude this discussion pointing out some of them, that seem to be more crucial.

a) The total number of ONSs is one of the most obvious parameters that affects the picture. All results scale linearly with N_{tot}, and models that predict rather lower birth rates may explain the discrepancy (see e.g. Hartman *et al.* 1997).

b) We stress again that standard models rely on the strong assumption that all old local NSs do in fact accrete at the Bondi rate (BM). At the low rates which are typical for ONSs accreting the ISM, the conditions under which accretion is possible are rather critical, and the answer strongly depends on the star velocity, spin period and magnetic field. Allowing for a distribution of these parameters may influence the results, since the two barriers at the accretion radius and at the Alfven radius (see 9.1) may be overcome only for a fraction of the total number of ONSs.

c) The equilibrium velocity distribution of ONSs has been calculated on the basis of rather conservative assumptions about the distributions at birth (see Paczyński 1990, TC, BM,

Zane *et al.* 1995). On the other hand, as a consequence of higher velocities at birth (e.g. Lyne & Lorimer 1994), old neutron stars may spread out over a larger volume in the Galaxy. At present, fewer slowly moving ONSs (that contribute mostly to the local counts) would therefore populate the local region around the Sun (see Hartman *et al.* 1997).

d) The controversy on the magnetic field and spin evolution is even more fierce. The problem is whether the field decay is necessary related to accretion, or it can occur also in isolated NSs. Since the decay times are supposedly comparable or larger than the pulsar lifetime, little evidence derives from pulsar statistics, and one should rely on highly speculative models for the neutron star interior. Very recently, however, Wang (1997) found some evidence for a substantial decay of the magnetic field, $B \sim 10^9$ G, precisely in the ONS candidate RX J0720.4-3125, but there is the possibility that this object is the outcome of the common envelope evolution of a binary system. On the other hand, the neutron star in the X–ray binary 4U1626-67 may be a counter–example: it may have accreted a considerable amount of mass and yet its magnetic field is $\sim 10^{12}$ G (Srinivasan 1997). If the magnetic field does not decay, a totally different picture must be expected. Large fields, $B \sim 10^{12}$ G, can either affect the spin evolution of a ONS (i.e. affect the possibility that accretion actually occurs) and modify the emitted radiation, shifting the spectrum and possibly excluding the ROSAT band. Moreover, accretion may be unsteady and ONSs might appear as transient X–ray sources (Treves, Colpi & Lipunov 1993, see also section 9.2)

Recently, points b) and d) were reconsidered by Treves, Colpi, Turolla (1997), who

presented some preliminary results about the consequences of relaxing the assumption of a constant, low value of the magnetic field in ONSs. Since the time evolution of the B–field is related to the rotational period of the NS, it is possible to construct a simple model, considering the spin evolution due to both dipole losses and the propeller mechanism (Illarionov, & Sunyaev 1975). The latter starts to be active when the incoming material penetrates below the accretion radius. In order to bracket uncertainties on the still poorly understood physics of the field decay, they assumed an exponential decay law for the crustal field and treated the decay timescale, τ_c as a free parameter (see also Ding, Chen & Chau 1993); the no decay case can be recovered for $\tau_c \gg 10^{10}$ yr. Fixing the ISM number density, $n = 1\,\mathrm{g\,cm^{-3}}$, and varying the values of τ_c, it is now possible to derive the maximum velocity v_{cr} (i.e. minimum accretion rate) for which steady accretion sets in. The main results are summarized in Table 9.8; B_f and P_f are the value of the surface magnetic field at the end of the propeller phase and the final period, both corresponding to a star with velocity v_{cr}. The initial values are $B = 2 \times 10^{12}$ G and $P = 0.01$ s. It is interesting to note that the limiting velocity for accretion is higher if no field decay occurs and progressively decreases for smaller τ_c. This can be understood taking into account that, for $\tau_c = \infty$, spin–down by magnetic braking is more effective ($dP/dt \propto B^{1/2}$) and the ONS enters the propeller phase earlier in the evolution. In addition, the value of the critical period at the end of the dipole radiation phase increases with both increasing B and v, thus promoting effective spin–down in the propeller phase.

We can see that the scenario previously discussed can be, broadly speaking, recovered for $\tau_c = 10^9$ yr. In this case, in fact, stars with $v \sim 70$ km/s can accrete, and they are characterized by a low magnetic field ($B \sim 6 \times 10^9$ G). All stars with $v \leq v_{cr}$ are at present

Table 9.8:

τ_c	B_f	P_f	v_{cr}	$\dot{M}_{cr}$
10^8 yr	10^9 G	s	km/s	10^{11} g/s
1	1.1	8.67	26	0.1
3.2	0.8	11.7	38	0.03
10	0.6	18.9	69	5×10^{-3}
32	85	1.7×10^3	85	3×10^{-3}
100	734	1.2×10^4	91	2.4×10^{-3}
316	1.4×10^3	2.1×10^4	90	2.5×10^{-3}
1000	1.8×10^3	2.5×10^4	90	2.5×10^{-3}
∞	2×10^3	2.7×10^4	90	2.5×10^{-3}

Taken from Treves, Colpi & Turolla 1997.

in the accretion phase, and, using equation (9.19), for $\tau_c = 10^9$ yr this corresponds to $\sim 0.5 N_{tot}$. However, it must be noted that B_f represents the present value of the magnetic field for stars with $v = v_{cr}$; NSs with lower velocity will enter the accretion phase earlier, with an higher magnetic field. Since in this case the spectral properties will be different, a more detailed estimate of the number of expected sources in the Rosat surveys should be performed. On the other hand, a scenario with $\tau_c = 10^8$ yr gives a stronger reduction in the number of resolved sources, since in this case only a small fraction of ONSs (with $v < 26$ km/s) are expected to be in the accretion phase.

While it is certainly true that other factors may play an important role, affecting the theoretical picture, these results seem to be particularly promising, since a range of models

parameter soothing the discrepancy between observed, unidentified X–ray sources and expected ONSs may be naturally provided. A detailed investigation of this issue is in progress, and it will be presented in the near future (Treves *et al.* 1997).

Bibliography

[1] Abramowitz, M., & Stegun, I.A. 1972, Handbook of Mathematical Functions, eds. Abramowitz, M., & Stegun, I.A., (New York: Dover) (AS)

[2] Alexanian, M. 1968, *Phys. Rev. D*, 165, 253

[3] Allen, D.A., Hyland, A.R., & Hillier, D.J. 1983, *MNRAS*, 204, 1145

[4] Alme, M.L., & Wilson, J.R. 1973, *ApJ* , 186, 1015 (AW)

[5] Alpar, M.A., et al. 1982, *Nature*, 300, 728

[6] Anderson, J.L., & Spiegel, E.A. 1972, *ApJ* , 171, 127

[7] Anile, A.M., & Sammartino, M. 1989, *Ann. Phys.*, 14, 325

[8] Anile, A.M., & Romano, V. 1992, *ApJ* , 386, 325

[9] Arnett, W.D., Schramm, D.N., & Truran, J.W. 1989, *ApJ* , 339, L25

[10] Bailey, M.E. 1980, *MNRAS*, 190, 217

[11] Begelman, M.C. 1978, *A&A*, 70, 583

[12] Begelman, M.C. 1979, *MNRAS*, 187, 237

[13] Belloni, T., Zampieri, L., & Campana, S. 1997, *A&A*, 319, 525

[14] Bhattacharya, D., Wijers, R.A.M.J., Hartman, J.W., & Verbunt, F. 1992 *A&A*, 254, 198

[15] Bildsten, L., Salpeter, E.E. & Wasserman, I. 1992, *ApJ* , 384, 143

[16] Binney, J., & Tremaine, S. 1987, Galactic Dynamics, (Princeton: Princeton University Press)

[17] Blaes, O., & Rajagopal, M. 1991, *ApJ* , 381, 210

[18] Blaes, O., Blandford, R.D., Madau, P., & Yan, L. 1992, *ApJ* , 399, 634

[19] Blaes, O., & Madau, P. 1993, *ApJ* , 403, 690 (BM)

[20] Blandford, R.D., & Payne, D.G. 1981a, *MNRAS*, 194, 1033

[21] Blandford, R.D., & Payne, D.G. 1981b, *MNRAS*, 194, 1041

[22] Bloemen, J.B.G.M. 1987, *ApJ* , 322, 694

[23] Blondin, J.M. 1986, *ApJ* , 308, 755

[24] Bowyer, S., *et al.* 1994, *ApJS*, 93, 569

[25] Burger, H.L., & Katz, J.I. 1980, *ApJ* , 236, 921

[26] Campana, S., & Mereghetti, S. 1993, *ApJ*, 413, L89

[27] Campana, S., Mereghetti, S., & Sidoli, L. 1996, *A&A*, in the press

[28] Castor, J.I. 1972, *ApJ* , 178, 779

[29] Chandrasekhar, S. 1960, Radiative Transfer, (New York: Dover)

[30] Chanmugam, G., Rao, M., & Tohline, J.R. 1987, *ApJ* , 319, 188

[31] Colpi, M. 1988, *ApJ* , 326, 233

[32] Colpi, M., Campana, S., & Treves, A. 1993, *A&A*, 278, 161

[33] Comastri, A., Setti, G., Zamorani, G., & Hasinger, G. 1995, *A&A*, 296, 1

[34] Cooper, G. 1971, *Phys. Rev. D*, 3, 2312

[35] Cowsik, R., & Lee, M.A. 1982, Proc. Roy. Soc. London A, 383, 409

[36] Cox, D.P., & Anderson, P.R. 1982, *ApJ* , 253, 268

[37] Cox, D.P. 1983, Supernova Remnants and Their X–ray Emission, IAU Symp. 101, eds. Danziger, J., & Gorenstein, P., Reidel, Dordrecht

[38] Cox, P., & Laureijs, R. 1989, in IAU Symp. 136, The Center of the Galaxy, ed. M. Morris, (Dordrecht: Kluwer)

[39] Dame, T.M. *et al.* 1987, *ApJ* , 322, 706

[40] Danner, R. 1996, unpublished PhD Thesis, Max–Planck Institut Für Extraterrestrische Physik, München

[41] Davies, R.E., & Pringle, J.E. 1981, *MNRAS*, 196, 209

[42] De Boer, H., 1991, in Proc. of the 144th IAU Symposium, ed. H. Bloemen, (Kluwer: Dordrecht)

[43] Dermer, C.D. 1984, *ApJ* , 280, 328

[44] Dermer, C.D. 1986, *ApJ* , 307, 47

[45] Deul, E.R., & Burton, W.B. 1988, Mapping the Sky: Past Heritage and Future Directions, ed. S. Debarat *et al.* , (Dordrecht: Kluwer)

[46] Diamond, C.J., Jewell, S.J.. & Ponman, T.J. 1995, *MNRAS*, 274, 589

[47] Dickey, J.M., & Lockman, F.J. 1990, *ARA&A*, 28, 215

[48] Ding, K.Y., Cheng, K.S., & Chau, H.F. 1993, *ApJ* , 408, 167

[49] Dullemond, C.P. 1997a, to be submitted on *A&A*

[50] Dullemond, C.P. 1997b, to be submitted on *A&A*

[51] Ebisawa, K., Titarchuk, L.. & Chakrabarti, S.K. 1996, *PASJ*, in the press

[52] Edelstein, J., Foster, R.S., & Bowyer, S. 1995, *ApJ* , 454, 442

[53] Flammang, R.A. 1982, *MNRAS*, 199, 833

[54] Flammang, R.A. 1984, *MNRAS*, 206, 589

[55] Frei, Z., Huang, X., & Paczyński, B. 1992, *ApJ* , 384, 105

[56] Freihoffer, D. 1981, *A&A*, 100, 178

[57] Frisch, P.C., & York, D.G. 1983, *ApJ*, 271, L59

[58] Genzel, R., Hollenbach, D., & Townes, C.H. 1994, Rep. Prog. Phys., 57, 417

[59] Gillman, A.W., & Stellingwerf, R.F. 1980, *ApJ* , 240, 235

[60] Goldreich, P., & Reisenegger, A. 1992, *ApJ* , 395, 250

[61] Gould, R.J. 1980, *ApJ* , 238, 1026

[62] Haberl, F., Pietsch, W., Motch, C., & Buckley, D.A.H. 1996, IAUC No. 6445

[63] Haberl, F., Motch, C., Buckley, D.A.H., Zickgraf, F.-J., & Pietsch, W. 1997, *A&A*, in press

[64] Haller, J.W., et al. 1996, *ApJ* , 456, 194

[65] Hansen, B.M.S., & Phinney, E.S. 1996, *BAAS*, 189

[66] Hartman, J.W. 1997, *A&A*, 322, 127

[67] Hartman, J.W., Bhattacharya, D., Wijers, R., & Verbunt, F. 1997, *A&A*, 322, 477

[68] Hartmann, D., Epstein, R.I., & Woosley, S.E. 1990, *ApJ* , 348, 625

[69] Hasinger, G., *et al.* 1993, *A&A*, 275, 1

[70] Haug, E. 1975, *Zs. Naturforschung*, 30a, 109

[71] Haug, E. 1985, *Phys. Rev. D*, 31, 2120; *Phys. Rev. D*32, 1594

[72] Hauschildt, P.H., & Wehrse, R. 1991, *J. Quant. Spec. Radiat. Transf.*, 46, 81

[73] Heitler, W. 1936, The Quantum Theory of Radiation, (Oxford: Oxford University Press)

[74] Helfand, D.J., Chanan, G.A., & Novick, R. 1980, *Nature*, 283, 337

[75] Hertz, P., Grindlay, J.E., & Bailyn, C.D. 1993, *ApJ* , 410, L87

[76] Illarionov, A., & Sunyaev, R. 1975, *A&A*, 39, 185

[77] Jauch, J.M., & Rohrlich, F. 1976, The Theory of Photons and Electrons, (New York: Springer–Verlag)

[78] Kafka, P., & Mèszàros, P. 1976, *Gen. Rel. & Grav.*, 7, 841

[79] Karzas, & Latter, 1961, *ApJS*, 6, 167

[80] Kawai, N., *et al.* 1988, *ApJ* , 330, 130

[81] Kellogg, E., *et al.* 1971, *ApJ*, 169, L99

[82] Kershaw, D.S., Prasad, M.K., & Beason, J.D. 1986, *J. Quant. Spec. Radiat. Transf.*, 36, 273

[83] Kershaw, D.S. 1987, *J. Quant. Spec. Radiat. Transf.*, 38, 347

[84] Knude, J.K. 1979, *A&AS*, 38, 407

[85] Kompaneets, A.S. 1956, *Soviet Phys. JETP*, 4, 730

[86] Koyama, K., *et al.* 1989, *Nature*, 339, 603

[87] Koyama, K., *et al.* 1996, in Proc. of "Röntgenstrahlung from the Universe", eds. Zimmermann, H.U., Trümper, J.E., & Yorke, H., MPE Report 263

[88] Lamb, D.Q. 1992, Frontieres of X–Ray Astronomy, eds. Tanaka, Y., & Koyama, K., (Tokyo: Universal Academy Press)

[89] Levermore, C.D., & Pomraning, G.C. 1981, *ApJ* , 248, 321

[90] Lindquist, R.W. 1966, *Ann. Phys.*(NY), 37, 487

[91] Lyne, A.G., & Lorimer, D.R. 1994, *Nature*, 369, 127

[92] Lorimer, D.R., Lyne, A.G., & Anderson, B. 1995, *MNRAS*, 275, 16L

[93] London, R.A., Taam, R.E., & Howard, W.E. 1986, *ApJ* , 306, 170

[94] Loose, H.H., Krügel, E., & Tutukov, A. 1982, *A&A*, 105, 342

[95] Madau, P., & Blaes, O. 1994, *ApJ* , 423, 748

[96] Malina, R.F., *et al.* 1994, *AJ*, 107, 751

[97] Maoz, E., & Grindlay, J.E. 1995, *ApJ* , 444, 183

[98] Maoz, E., Ofek, E.O., & Shemi, A. 1997, *MNRAS*, 287, 293

[99] Maraschi, L., Reina, C., & Treves, A. 1974, *A&A*, 35, 389

[100] Maraschi L., Treves A., & Tarenghi M. 1973, *A&A*, 25, 153

[101] Markevitch, M., Sunyaev, R.A., & Pavlinsky, M. 1993, *Nature*, 364, 40

[102] Mastichiadis, A., & Kylafis, N.D. 1992, *ApJ* , 384, 136

[103] McDonald, K., *et al.* 1994, *AJ*, 108, 1843

[104] McKee, C., & Ostriker, J.P. 1977, *ApJ* , 218, 148

[105] Melrose, D.B. 1986, Instabilities in Space and Laboratory Plasmas, (Cambridge: Cambridge University Press)

[106] Mèszàros, P. 1975, *A&A*, 44, 59

[107] Mihalas, D., Kunasz, P.B., & Hummer, D.G. 1975, *ApJ* , 202, 465

[108] Mihalas, D., Kunasz, P.B., & Hummer, D.G. 1976a, *ApJ* , 203, 647

[109] Mihalas, D., Kunasz, P.B., & Hummer, D.G. 1976b, *ApJ* , 206, 515

[110] Mihalas, D. 1980, *ApJ* , 237, 574

[111] Mihalas, D., & Mihalas, B. 1984, Foundations of Radiation Hydrodynamics, (Oxford: Oxford University Press)

[112] Miller, M.C. 1992, *MNRAS*, 255, 129

[113] Miller, J.C., & Rezzolla, L. 1995, *Phys. Rev. D*, 51, 4017

[114] Misner, C.W., Thorne, K.S., & Wheeler, J.A. 1973, Gravitation, Box 25.7, (San Francisco: Freeman & Co.) (MTW)

[115] Morris, M. 1993, *ApJ* , 408, 496

[116] Morris, M., & Serabyn, E. 1996, *ARA&A*, 34, 645

[117] Morrison, R., & McCammon, D. 1983, *ApJ* , 270, 119

[118] Motch, C., *et al.* 1997, *A&A*. 318, 111

[119] Narayan, R., & Ostriker, J.P. 1990, *ApJ* , 352, 222

[120] Nelson, R.W., Wang, J.C.L., Salpeter, E.E., & Wasserman, I. 1995, *ApJ*, 438, L99

[121] Nobili, L., & Turolla, R. 1988, *ApJ* , 333, 248

[122] Nobili, L., Turolla, R., & Zampieri, L. 1991, *ApJ* , 383, 250 (NTZ91)

[123] Nobili, L., Turolla, R., & Zampieri, L. 1993, *ApJ* , 404, 686 (NTZ93)

[124] Nobili, L. 1997, to appear in Proc. of "Open problems about astrophysical jets: origin. energy transport and radiation," Torino, Italy

[125] Nottingham, M.R., *et al.* 1993, *A&AS*, 97, 165

[126] Novikov, I.D., & Thorne, K.S. 1973, Black Holes, eds. DeWitt, C., & DeWitt B.S.. (New York: Gordon & Breach)

[127] Ostriker, J.P., & Gunn , J.E. 1969, *ApJ* , 157, 1395

[128] Ostriker, J.P., Rees, M.J., & Silk, J. 1970, *Astrophys. Lett.*, 6, 179

[129] Paczyński, B. 1990, *ApJ* , 348, 485

[130] Park, M.–G., & Ostriker, J.P. 1989, *ApJ* , 347, 679

[131] Park, M–G. 1990a, *ApJ* , 354, 64

[132] Park, M.–G. 1990b, *ApJ* , 354, 83

[133] Payne, D.G., & Blandford, R.D. 1981, *MNRAS*, 196, 781 (PB)

[134] Paresce, F. 1984, *AJ*, 89, 1022

[135] Phinney, E.S., & Kulkarni, S.R. 1994, *ARA&A*, 32, 591

[136] Pomraning, G.C. 1973, The Equations of Radiation Hydrodynamics, (New York: Pergamon Press)

[137] Pomraning, G.C. 1983, *ApJ* , 266, 841

[138] Pounds, K.A., *et al.* 1993, *MNRAS*, 260, 77

[139] Prasad, M.K., Shestakov, A.I., Kershaw, D.S., & Zimmerman, G.B. 1988, *J. Quant. Spec. Radiat. Transf.*, 40, 29

[140] Predehl, P., & Trümper, J. 1994, *A&A*, 290, L29

[141] Psaltis, D., & Lamb, F.K. 1997, *ApJ* , submitted

[142] Quigg, C. 1968, *ApJ* , 151, 1187

[143] Rajagopal, M., & Romani, R.W. 1996, *ApJ* , 461, 327

[144] Rees, M.J. 1978, *Phys. Scripta*, 17, 193

[145] Rezzolla, L., & Miller, J.C. 1994, *Class. Quantum Gravit.*, 11, 1815

[146] Rezzolla, L. 1996, *Phys. Rev. D*, 54, 6072

[147] Rezzolla, L., & Miller, J.C. 1996, *Phys. Rev. D*, 53, 5411

[148] Risken, H. 1989, The Fokker–Planck Equation (Berlin: Springer–Verlag)

[149] Rybicki, G.B., & Lightman, A.P. 1979, Radiative Processes in Astrophysics, (New York: Wiley)

[150] Rossano, G.S., 1978, *AJ*, 83, 1214

[151] Romani, R.W. 1987, *ApJ* , 313, 718

[152] Romani, R.W. 1990, *Nature*, 347, 741

[153] Sanders, R.H. 1989, in IAU Symp. 136, The Center of the Galaxy, ed. M. Morris, (Dordrecht: Kluwer)

[154] Sang, Y., & Chanmugam, G. 1987, *ApJ*, 323, L61

[155] Sang, Y., & Chanmugam, G. 1990, *ApJ* , 363, 597

[156] Schinder, P.J. 1988, *Phys. Rev. D*, 38, 1673

[157] Schinder, P.J., & Bludman, S.A. 1989, *ApJ* , 346, 350

[158] Schmid–Burgk, J. 1978, *Ap.&Space Sci.*, 56, 191

[159] Schneider, P., & Bogdan, T.J. 1989, *ApJ* , 347, 496

[160] Sellgren, K., et al. 1990, *ApJ* , 359, 112

[161] Shapiro, S.L., & Salpeter, E.E. 1973, *ApJ* , 198, 761

[162] Shapiro, S.L. 1973a, *ApJ* , 180, 531

[163] Shapiro, S.L. 1973b, *ApJ* , 185, 69

[164] Shemi, A. 1994, *MNRAS*, 269, 1112

[165] Shestakov, A.I., Kershaw, D.S., & Prasad, M.K. 1988, *J. Quant. Spec. Radiat. Transf.*, 40, 577

[166] Shibanov, Yu.A., *et al.* 1992, *A&A*, 266, 313

[167] Shvartsman, V.F. 1971, *Soviet Ast. -AJ*, 15, 377

[168] Skinner, G.K., *et al.* 1987, *Nature*, 330, 544

[169] Skinner, G.K. 1989, in IAU Symp. 136, The Center of the Galaxy, ed. M. Morris (Dordrecht: Kluwer)

[170] Simon, R. 1963, *J. Quant. Spec. Radiat. Transf.*, 3, 1

[171] Sneddon, I.N. 1956, Special Functions of Mathematical Physics and Chemistry. (Edinburgh: Oliver & Boyd)

[172] Soffel, M.H. 1982, *A&A*, 116, 111

[173] Sofue, Y. 1995a, *PASJ*, 47, 527

[174] Sofue, Y. 1995b, *PASJ*, 47, 551

[175] Srinivasan, G., Bhattacharya, D., Muslimov, A.G., & Tsygan, A.I. 1990, *Curr. Sci.*, 59, 31

[176] Srinivasan, G. 1997, in Saas–Fee Advanced Course 25, Lecture Notes 1995, eds. Meynet, G., & Schaerer, D., (Berlin Heidelberg: Springer–Verlag)

[177] Stepney, S., & Guilbert, P.W. 1983, *MNRAS*, 204, 1269

[178] Stocke, J.T., *et al.* 1995, *AJ*, 109, 1199

[179] Sunyaev, R.A., Markevitch, M., & Pavlinsky, M. 1993, *ApJ* , 407, 606

[180] Svensson, R., 1982, *ApJ* . 258, 335

[181] Svensson, R., 1983, *ApJ* , 270, 300

[182] Tamazawa, S., Toyama, K., Kaneko, N., & Ôno, Y. 1974, *Ap.&Space Sci.*, 32, 403

[183] Taylor, J., Manchester, R., & Lyne, A. 1993, *ApJS*, 88,529

[184] Tavani, M., & Liang, E. 1996, *A&A*. in press

[185] Titarchuk, L. 1997, in Proc. of the 2nd Integral Workshop, ESA SP-382

[186] Titarchuk, L, Lapidus, I., & Muslimov, A. 1997, *ApJ* , submitted

[187] Thomas, L.H. 1930, *Q. Jl. Math.*. 1. 239

[188] Thomas, B., *et al.* 1996, in Proc. of "Röntgenstrahlung from the Universe", eds. H.U. Zimmermann, J.E. Trümper, & H. Yorke, MPE Report 263

[189] Thorne, K.S. 1981, *MNRAS*, 194. 439 (Th81)

[190] Thorne, K.S., Flammang, R.A., & Żytkow, A.N. 1981, *MNRAS*, 194, 475

[191] Treves, A., & Colpi, M. 1991, *A&A*. 241, 107 (TC)

[192] Treves, A., Colpi, M., & Lipunov, V.M. 1993, *A&A*, 269, 319

[193] Treves, A., Colpi, M., & Turolla, R. 1997, poster presented at the conference "X–Ray Surveys", Potsdam, 17–20 June 1997

[194] Treves *et al.* 1995, "Problems in the Theory of Old Neutron Stars Accreting the Interstellar Medium", Grossman Meeting Proceedings

[195] Treves *et al.* 1997, in preparation

[196] Turolla, R., & Nobili, L. 1988, *MNRAS*, 235, 1273

[197] Turolla, R., Zampieri, L., Colpi, M., & Treves, A. 1994, *ApJ* , 426, L35 (paper I)

[198] Turolla, R., Zampieri, L., & Nobili, L. 1995, *MNRAS*, 272, 625

[199] Turolla, R., Zane, S., Zampieri, L., & Nobili, L. 1996, *MNRAS*, 283, 881

[200] Urpin, V.A., Chanmugam, G., & Sang, Y. 1994, *ApJ* , 433, 780

[201] Vargas, M., *et al.* 1996, *A&A*, 313, 828

[202] Verbunt, F., Belloni, T., Johnston, H.M., Van der Klis, M., & Lewin, W.H.G. 1994, *A&A*, 285, 903

[203] Vitello, P.A.J. 1978, *ApJ* , 225, 694

[204] Walter, F.M., Wolk, S.J., & Neuhäuser, R. 1996, *Nature*, 379, 233

[205] Wandel, A., Yahil, A., & Milgrom, M. 1984, *ApJ* , 282, 53

[206] Wang, Y.M., & Robertson, J.A. 1985, *A&A*, 151, 361

[207] Wang, J.C.L. 1996, *Nature*, 379, 206

[208] Wang, J.C.L. 1997, *ApJ*, in press

[209] Watson, M.G., *et al.* 1981, *ApJ* , 250, 142

[210] Welsh, B.Y., Craig, N., Vedder, P.W., & Vallerga, J.V. 1994, *ApJ* , 437, 638

[211] White, N.E., Nagase, F., & Parmar, A.N. 1993, X–Ray Binaries, eds. Lewin, W.H.G., van Paradijs, J., & van den Heuvel, E.P.J., Cambridge University Press

[212] White, N.E., Giommi, & P., Angelini, L. 1994, IAU Circ. 6100

[213] Wielen, R. 1977, *A&A*, 60, 263

[214] Yamauchi, S., *et al.* 1990, *ApJ* , 365, 532

[215] Zampieri, L., Miller, J.C., & Turolla, R. 1996, *MNRAS*, 281, 1183

[216] Zampieri, L., Turolla, R., & Treves, A. 1993, *ApJ* , 419, 311

[217] Zampieri, L. 1995, PhD Thesis

[218] Zampieri, L., Turolla, R., Zane, S., & Treves, A. 1995, *ApJ* , 439, 849

[219] Zane, S., *et al.* 1995, *ApJ* , 451, 739

[220] Zane S., Turolla, R., Nobili, L., & Erna, M. 1996a, *ApJ* , 466, 871

[221] Zane, S., Zampieri, L., Turolla, R., & Treves, A. 1996b, *A&A*, 309, 469

[222] Zane, S., Turolla, R., & Treves, A. 1996, *ApJ* , 471, 248

[223] Zane, S., Turolla, R., & Treves, A. 1997a, *ApJ* , in the press

[224] Zane, S., Turolla, R., & Treves, A. 1997b, to appear in Proc. of "The many faces of Neutron Stars", NATO–ASI Series, Lipari, Italy

[225] Zavlin, V.E., Pavlov, G.G., & Shibanov, Y.A. 1996, *A&A*, 315, 141

[226] Zel'dovich, Ya, & Raizer, Yu. 1967, Physics of Shock Waves and High–Temperature Hydrodynamic Phenomena, (New York: Academic Press)

[227] Zel'dovich, Ya., & Shakura, N. 1969, *Soviet Ast. -AJ*, 13, 175 (ZS)

Appendix A

The coefficients A_i's

Here we present the expressions of the A_i, $i = 1, \ldots, 8$, terms appearing into equation (3.24). Their derivation starts from Fraser's result, equation (3.22), and makes use of relation

$$\xi = \mu\mu' + \sqrt{1-\mu'^2}\sqrt{1-\mu^2}\cos\left(\Phi - \Phi'\right) . \tag{A.1}$$

At first order in γ and τ, only the first four moments m_ν^n of the distribution function

$$m_\nu^n = \frac{1}{2}\int_{-1}^{1} f\mu^n d\mu \tag{A.2}$$

appear in the Compton source term; they will be termed j_ν, h_ν, k_ν and l_ν, using the standard notation. The relation between m_ν^n and the more familiar correspondent moments of the specific intensity I_ν is simply:

$$M_\nu^n = E^3 m_\nu^n . \tag{A.3}$$

To make the larger number of terms dimensionless, we introduce double logarithmic frequency derivatives for all even moments; terms containing odd moments are written as semi–logarithmic derivatives since odd moments may become vanishingly small in regions

where the effective optical depth is very large. The final result is:

$$A_1 = j_\nu \left\{ 1 - \gamma \left(1 - \frac{\partial \ln J_\nu}{\partial \ln \nu} \right) + \tau \left[\frac{\partial^2 \ln J_\nu}{\partial \ln \nu^2} + \left(\frac{\partial \ln J_\nu}{\partial \ln \nu} \right)^2 - 3 \frac{\partial \ln J_\nu}{\partial \ln \nu} \right] \right\} \tag{A.4}$$

$$A_2 = \frac{6}{5} \left[(\gamma - \tau) h_\nu - \frac{1}{E^3} (\gamma - 3\tau) \frac{\partial H_\nu}{\partial \ln \nu} - \frac{\tau}{E^3} \frac{\partial^2 H_\nu}{\partial \ln \nu^2} \right] \tag{A.5}$$

$$\begin{aligned} A_3 = {} & \frac{1}{8} \left\{ (1 - \gamma - 6\tau)(j_\nu - 3k_\nu) + (\gamma - 3\tau) \left(j_\nu \frac{\partial \ln J_\nu}{\partial \ln \nu} - 3k_\nu \frac{\partial \ln K_\nu}{\partial \ln \nu} \right) \right. \\ & \left. + \tau \left[j_\nu \left(\left(\frac{\partial \ln J_\nu}{\partial \ln \nu} \right)^2 + \frac{\partial^2 \ln J_\nu}{\partial \ln \nu^2} \right) - 3k_\nu \left(\left(\frac{\partial \ln K_\nu}{\partial \ln \nu} \right)^2 + \frac{\partial^2 \ln K_\nu}{\partial \ln \nu^2} \right) \right] \right\} \end{aligned} \tag{A.6}$$

$$\begin{aligned} A_4 = {} & \frac{3}{40} \left[(\gamma + 4\tau)(3h_\nu - 5l_\nu) - \frac{1}{E^3} (\gamma - 3\tau) \left(3 \frac{\partial H_\nu}{\partial \ln \nu} - 5 \frac{\partial L_\nu}{\partial \ln \nu} \right) \right. \\ & \left. - \frac{\tau}{E^3} \left(3 \frac{\partial^2 H_\nu}{\partial \ln \nu^2} - 5 \frac{\partial^2 L_\nu}{\partial \ln \nu^2} \right) \right] \end{aligned} \tag{A.7}$$

$$A_5 = \frac{3}{8} \left(3j_\nu - k_\nu - 3j_\nu \frac{\partial \ln J_\nu}{\partial \ln \nu} + k_\nu \frac{\partial \ln K_\nu}{\partial \ln \nu} \right) \tag{A.8}$$

$$A_6 = \frac{3}{8} \left(j_\nu - 3k_\nu - j_\nu \frac{\partial \ln J_\nu}{\partial \ln \nu} + 3k_\nu \frac{\partial \ln K_\nu}{\partial \ln \nu} \right) \tag{A.9}$$

$$A_7 = \frac{3}{8} \left(h_\nu - \frac{1}{E^3} \frac{\partial H_\nu}{\partial \ln \nu} \right) \tag{A.10}$$

$$A_8 = \frac{3}{8} \left(l_\nu - \frac{1}{E^3} \frac{\partial L_\nu}{\partial \ln \nu} \right) \tag{A.11}$$

Appendix B

The coefficients $A_n^{\pm}$

Since the polynomials $G_n(b-n.c.z)$ appearing in equation (6.30) are not an orthogonal system, is not possible to derive an explicit expression for the coefficients $A_n^{\pm}$. Here we show that these constants can be, in principle, obtained as the solution of an infinite system of linear algebraic equations. We note that the two sets $A_n^{\pm}$ are not independent, because the two expressions in (6.30) must match at $\nu = \nu_0$, where

$$w_\nu^1(t,\nu_0) = A\delta(t/t_* - 1) \tag{B.1}$$

(A is a constant related to the monochromatic flux injected at the inner boundary). Since $z \propto t/t_h$ and $x = t/t_*$, the polynomials $G_n(b-n,c,z)$ can be expressed in terms of $G_n(3,3,x)$, which form an orthogonal system, as

$$G_n(b-n,c,z) = \sum_{m=0}^{n} C_{nm} G_m(3,3,x)\,. \tag{B.2}$$

The coefficients C_{nm} are solution of the upper triangular system of linear algebraic equations

$$\sum_{m=k}^{n}(-1)^{m-n}\binom{m}{k}\frac{(m+2)!(m+2+k)!}{(2m+2)!(k+2)!}C_{nm} = \binom{n}{k}\frac{\Gamma(c+n)\Gamma(b+k)}{\Gamma(b+n)\Gamma(c+k)}\left(-\frac{\beta}{\gamma}t_*\right)^k\,, \tag{B.3}$$

for $k = 0, \ldots, n$. Recalling the standard expansion of the δ–function over an orthogonal set of eigenfunctions and using again $G_n(3,3,x)$ as a basis, it is

$$\delta(x-1) = x^2 \sum_{m=0}^{\infty} \frac{(2m+3)!}{m!(m+2)!} G_m(3,3,x)\,. \tag{B.4}$$

Inserting (B2) and (B4) into (B1) and equating the coefficients of the polynomials of the same degree, we obtain

$$\sum_{n=m}^{\infty} (-1)^n \frac{(b)_n}{(c)_n} C_{nm} A_n^{\pm} = \frac{A}{t_*^2} \frac{(2m+3)!}{m!(m+2)!} \qquad m \geq 0\,. \tag{B.5}$$

The numerical evaluation of $A_n^{\pm}$ has been carried out truncating the series appearing in (B5) to a maximum order $N \sim 60$ and solving the system by backsubstitution.

List of Figures

Acknowledgments

During the four years of my Phd, I splitted my time in different cities. Working in all of them, I have benefited enormously through the knowledge and the interaction with a number of very special persons. It is virtually impossible to name all these people here, but I certainly would like to thanks some of them who, in different parts of the worlds, helped me in many ways and in various occasions.

Trieste: My deepest thanks to Aldo Treves, to whom I am enormously indebted for his encouragement in my work, his supervision, enlighting example and friendship. I wish to thanks also Dennis Sciama, head of the astrophysics Sector at Sissa, for his constant help and support in my research. Particular thanks to George Ellis, for his enlighting teachings in General Relativity during my first year, and to John Miller, Antonio Lanza, Marco Bruni, Marek Abramowicz, Francesca Matteucci, Alberto Parola who generously offered me their scientific experience and friendship.

Padova: I am specially, deeply grateful to my Teachers and friends, Luciano Nobili and Roberto Turolla, for explaining me most of the things that I know in astrophysics; for their example in and out of the work; for their patience and constant help; for their strong, continuous encouragement. I'd like to thank also Ornella Pantano and Sabino Matarrese,

who shared with me my staying in Padova and lots of discussions during a million of lunch breaks!

Milano: A great thanks to Monica Colpi, for her friendship and for the deep scientific and human interaction. Sergio Campana, Francesco Haardt, Sandro Mereghetti also often offered me their experience and help.

Urbana–Champaign: I will be always in debt to Stu Shapiro, for putting me on the way of General Relativity, for his strong encouragement and for his example in and away of science. Actually, a lot of really special people contribute to make unforgettable my staying in Illinois. I am delighted to thank Fred and Susan Lamb for their hospitality, for all nice and fruitful discussions, and for their suggestions; Dimitri Mihalas for deep insights in radiative transfer and for his friendship. Thomas Baumgarte and one of my closest collaborators, Luca Zampieri, who offered me their scientific experience and their constant help!

I would like to thank also the scientific and administrative staff of SISSA, University of Padova and Loomis Laboratory for Physics at UIUC, always ready to provide me technical support and, in general, whatever I needed it. A friendly thank to Gianfranco Carpani, for his help in using the scanner for some of the figures of this thesis.

Finally, in different part of the world, lots of friends shared with me science, good time, fun and love. Just to mention some of them, in strictly random order, I want to deserve a particular great thanks to: Cristina Chiappini, for being a guide that made easier my approach to life; Gianluca Israel, who successfully survived to my turns of mood with his own characteristic patience and sense of paradox, when sharing with me office

and life during the unforgettable three years in SISSA; Elisabetta Dotto, for the solar friendship; Enzo Branchini for being an exceptional psychologist and a critical help in lots and lots of situations; Giovanni Fossati, who also shared the mythic room 480 with all related consequences; Tomaso Belloni, who contributed to this thesis with lots of technical informations about English, X–ray data, and with a prompt intervent whenever I needed it.

Dimitrios Psaltis, Vicky Kalogera, Gail Conway, Sean Points, Paschal Paschos, Mark Sincell to have been the stone–miles that made possible to survive during the cold winter in Illinois ! Thanks in particular to Dimitrios, who is a real good colleague and friend, for helpful and fun discussions about radiative transfer and life.

For a lot of fun days (and evenings!) in Sissa, thanks to Elena (two), Francesco (two), Cecilia, Cristiano, Silvia, Laura, Enrico, Alejandra, Alice, Marco, Claudio, Daniele, Stefano, Massimo.

Last, I send my love to Marco, to whom I am deeply grateful for his presence in my life and for believing in me.